MICROMACHINED MEMBRANE-BASED ACTIVE PROBES FOR BIOMOLECULAR FORCE SPECTROSCOPY

A Dissertation
Presented to
The Academic Faculty

by

Hamdi Torun

In Partial Fulfillment
of the Requirements for the Degree
Doctor of Philosophy in the
School of Electrical and Computer Engineering

Georgia Institute of Technology
May 2010

MICROMACHINED MEMBRANE-BASED ACTIVE PROBES FOR BIOMOLECULAR FORCE SPECTROSCOPY

Approved by:

Dr. F. Levent Degertekin, Advisor
School of Electrical and Computer Engineering
Georgia Institute of Technology

Dr. Cheng Zhu
School of Biomedical Engineering
Georgia Institute of Technology

Dr. Oliver Brand
School of Electrical and Computer Engineering
Georgia Institute of Technology

Dr. Pamela T. Bhatti
School of Electrical and Computer Engineering
Georgia Institute of Technology

Dr. Thomas G. Habetler
School of Electrical and Computer Engineering
Georgia Institute of Technology

Date Approved: December 11,2009

ACKNOWLEDGEMENTS

I would like to thank Prof. Levent Degertekin for his support and guidance in every aspect of the research described in this thesis. His creativeness and optimism always encouraged me and definitely proved substantial towards the completion of this work. I would also like to thank Prof. Cheng Zhu, Prof. Oliver Brand, Prof. Pamela Bhatti, and Prof. Thomas Habetler for serving on my thesis committee.

I owe thanks to all members of our research laboratory, especially: Dr. Jemmy Sutanto for helping me with device fabrication and building the experimental setup; Dr. Krishna Sarangapani for his help with biological experiments; and Ofer Finkler for helping me with instrumentation. Here, I also acknowledge Dr. Fang Kong from Prof. Zhu's group for helping us with our setup and kindly providing us with biological molecules. I always benefited from the fruitful collaboration between Prof. Zhu and Prof. Degertekin.

This thesis would be impossible without the unconditional support of my family. Finally, and most importantly, I would like to thank Ayse, Hande and my parents for their support and understanding.

The National Institutes of Health (Grant No. R1 AI060799) provided the financial support for this research.

TABLE OF CONTENTS

LIST OF TABLES

LIST OF FIGURES

SUMMARY

Atomic force microscope (AFM) is an invaluable tool for measurement of pico-Newton to nano-Newton levels of interaction forces in liquid. As such, it is widely used to measure single-molecular interaction forces through dynamic force spectroscopy. In this technique, the interaction force spectra between a specimen on the sharp tip of the cantilever and another specimen on the substrate is measured by repeatedly moving the cantilever in and out of contact with the substrate. By varying the loading rate and measuring the bond rupture force or bond lifetime give researchers information about the strength and dissociation rates of non-covalent bonds, which in turn determines the energy barriers to overcome. Commercially available cantilevers can resolve interaction forces as low as 5 pN with 1 kHz bandwidth in fluid. This resolution can be improved to 1 pN by using smaller cantilevers at the expense of microfabrication constraints and sophisticated detection systems. The pulling speed of the cantilever, which determines the loading rate of the bonds, is limited to the point where the hydrodynamic drag force becomes comparable to the level of the molecular interaction force. This level is around 10 μm/s for most cantilevers while higher pulling speeds are required for complete understanding of force spectra. Thus, novel actuators that allow higher loading rates with minimal hydrodynamic drag forces on the cantilevers, and fast, sensitive force sensors with simple detection systems are highly desirable.

This dissertation presents the research efforts for the development of membrane-based active probe structures with electrostatic actuation and integrated diffraction-based optical interferometric force detection for single-molecular force measurements. Design, microfabrication and characterization of the probes are explained in detail. A setup including

optics and electronics for experimental characterization and biological experiments with the probes membranes is also presented. Finally, biological experiments are included in this dissertation.

The "active" nature of the probe is because of the integrated, parallel-plate type electrostatic actuator. The actuation range of the membrane is controlled with the gap height between the membrane and the substrate. Within this range it is possible to actuate the membrane fast, with a speed limited by the membrane dynamics with negligible hydrodynamic drag. Actuating these membrane probes and using a cantilever coupled to the membrane, fast pulling experiments with an order of magnitude faster than achieved by regular AFM systems are demonstrated.

The displacement noise spectral density for the probe was measured to be below 10 fm/√Hz for frequencies as low as 3 Hz with differential readout scheme. This noise floor provides a force sensitivity of 0.3 – 3 pN with 1 kHz bandwidth using membranes with spring constants of 1 – 10 N/m. This low inherent noise has a potential to probe wide range of biomolecules. The probes have been demonstrated for fast-pulling and high-resolution force sensing. Feasibility for high throughput parallel operation has been explored. Unique capabilities of the probes such as electrostatic spring constant tuning and thermal drift cancellation in AFM are also presented in this dissertation.

CHAPTER 1

INTRODUCTION

This thesis describes the development of micromachined membrane-based active displacement and force sensing probes for biomolecular mechanics measurement. These active probes may replace passive micro-cantilevers of atomic force microscopes (AFM) used for applications of life sciences. The "active" nature of these probes is because of the integrated parallel-plate electrostatic actuator whereas the membrane displacement can be measured with high resolution using integrated diffraction-based interferometer.

Chapter 1 of the thesis describes the applications of conventional AFM methods in life sciences. Chapter 1 also introduces the methods central to the membrane probe which are further described in detail by providing the design, fabrication and experimental results in following chapters.

Atomic Force Microscope and Biomolecular Force Measurements

Since its invention in 1986, atomic force microscope has become an essential tool for applications such as high-resolution imaging at sub-nano scale, measurement of single-biomolecular interactions, and viscoelasticity measurements for material characterization [1-4]. In a conventional AFM system, a passive, microscale cantilever is used as the force sensing element to measure the interaction force between the sharp cantilever tip and the sample surface. The cantilever is brought in and out of contact of a

surface using a piezo actuator and the forces are detected by using the optical lever detection mechanism based on the spring constant of the cantilever. An AFM system is schematically shown in figure 1(a), where the cantilever scans a sample surface in a closed-loop operation and the deflection of the cantilever is detected by optical means. Figure 1(b) shows an SEM image of typical micro-scale AFM cantilevers.

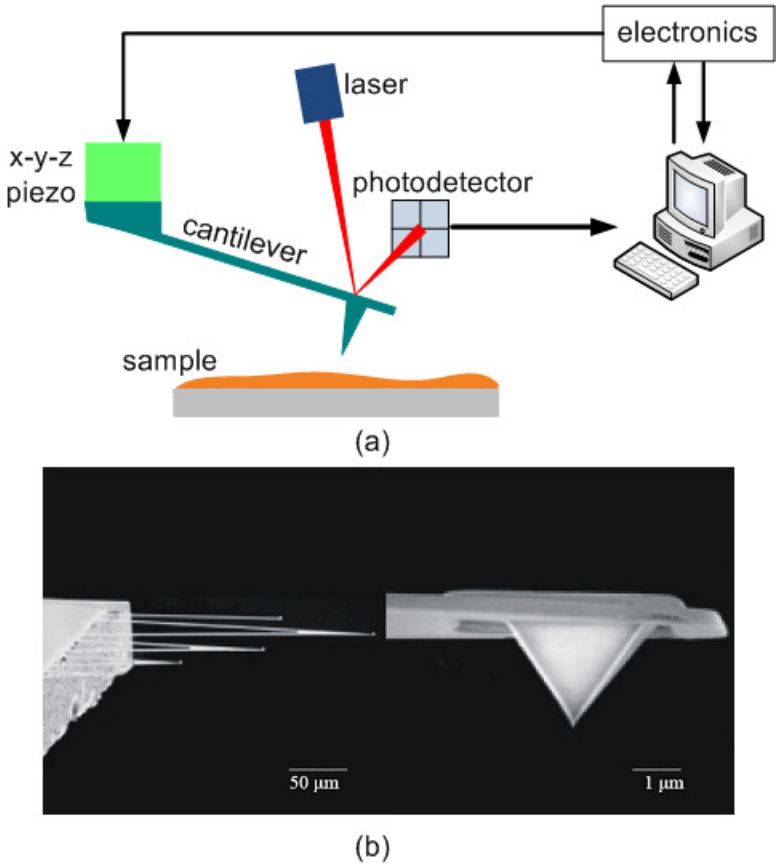

Figure 1. (a) Schematic of AFM employing optical lever method for detection. (b) SEM image of AFM cantilevers and closed view of a sharp tip (from http://www.veecoprobes.com).

The first operation of AFM in liquid was demonstrated in 1987 [5], followed by the investigation of its potential for biology [6]. Applications of AFM in life sciences

have been increasing in both variety and significance during the past decade [7-9]. In addition to high resolution imaging of cells, DNA and other biological structures, AFM enables single molecule mechanics studies characterizing both intramolecular and intermolecular forces [4, 10].

In a conventional AFM system for biomolecular force spectroscopy; the force sensing passive micro-cantilever is functionalized by biological specimens such as proteins, antibodies, antigens and ligands whose properties are being investigated. The interaction force between a specimen on the sharp tip of the cantilever and another specimen on the apposing substrate is measured repeatedly by moving the cantilever in and out of contact with the substrate using the piezo tube actuator of the AFM system.

A representative photodetector (PD) trace for a single touch is shown in figure 2. Here y-axis shows PD output proportional to the bending of cantilever, hence the force exerted on the cantilever. X-axis is time and for a fixed piezo speed this denotes the distance from the base of the cantilever to the sample stage. The experiment starts at segment-1 where the functionalized cantilever stays within the vicinity of the functionalized sample. Then, the cantilever is moved towards the sample using the piezo actuator and it gets into contact with the sample at segment-2. The cantilever is further moved into the sample to allow the formation of a bond between the apposing biomolecules at segment-3. Then, the piezo reverses its direction at segment-4 and continues to move the cantilever out-of-contact with the sample. If a biological bond is formed, the cantilever is exposed to a rupture (unbinding) force at segment-5 before it goes out-of-contact. The bond finally breaks and the cantilever becomes free again, thus it snaps back to its resting position at segment-6.

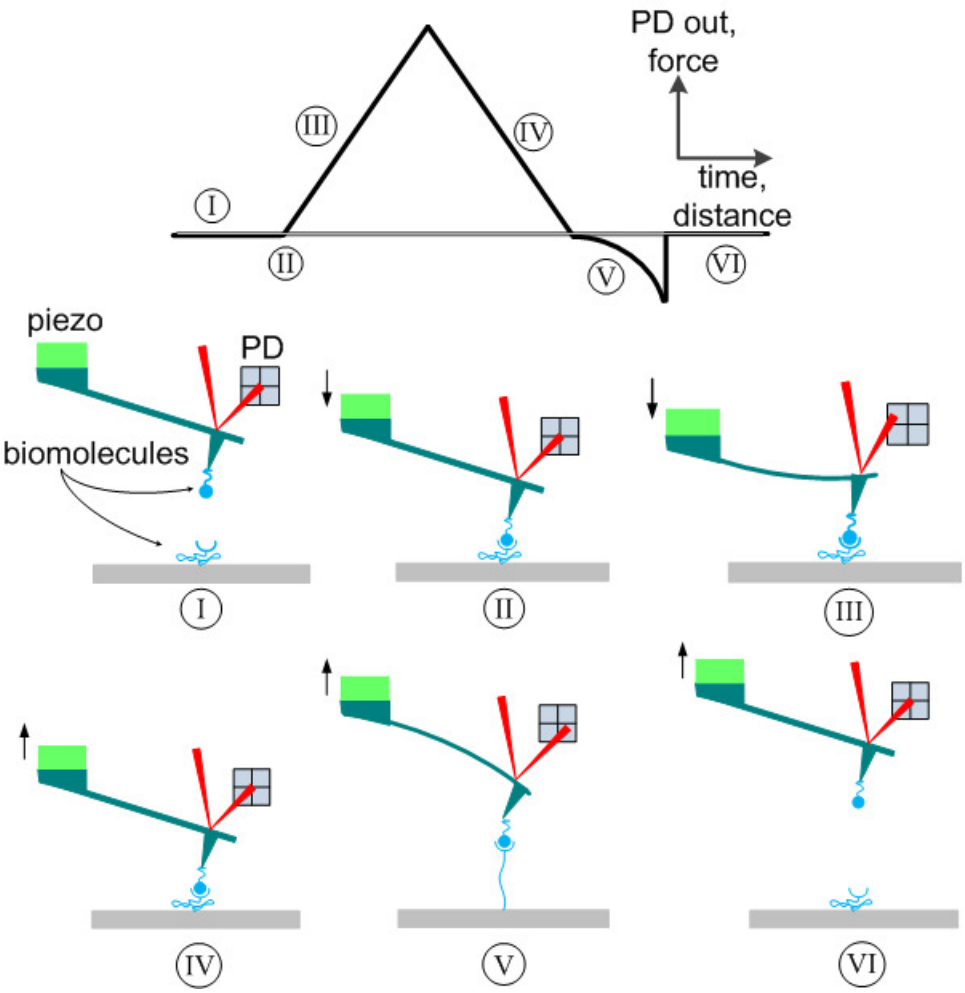

Figure 2. Representation of photodetector signal in a biomolecular force spectroscopy experiment. The segments of the signal are labeled. Relative position of the cantilever and the sample is shown for each labeled segment.

Non-linear portion of the signal, segment-5, is characteristic for the biological system under investigation. Small biomolecules, such as antibodies, are usually attached to the surface using polymer tethers. Therefore segment-5 is characterized by the polymer elasticity [11]. Larger molecules, such as protein titin, also display polymer elasticity when anchored to the tip directly. Following the polymer extension, unbinding force

corresponds to the instantaneous force measured when the bond between the biomolecules is broken. Florin et al. reported the first measurement of unbinding forces between biotin and avidin pairs [12]. It was later shown that bond rupture is, indeed, a random process and unbinding force scales logarithmically with the loading rate, i.e., the rate of force exerted on the molecules [13]. Accordingly, dynamic force spectroscopy has been employed to vary loading rate and to reveal the characteristics of interactions between biomolecules.

One application of dynamic force spectroscopy is to understand the energy landscape of biomolecular pairs by probing the intermolecular interactions at different loading rates. The concentration of bound molecules at a specific time, $S(t)$, depends on the kinetic rate of dissociation. Under the effect of external force, f, the kinetic rate of dissociation, $k_{off}(f)$, would be considerably different than the rate at the absence of force, k_{off}. The governing equations are given in equation 1 and 2.

$$\frac{dS}{dt} = -k_{off}(f) \cdot S(t) \tag{1}$$

$$k_{off}(f) = k_{off} \exp\left(\frac{f}{k_B T / r_o} \right) \tag{2}$$

Theory of dynamic force spectroscopy combines these equations and relates the unbinding force, f^*, to the loading rate, r_f, explicitly as follows:

$$f^* = \frac{k_B T}{r_o} In\left(\frac{r_f}{k_B T / r_o \cdot k_{off}} \right) \tag{3}$$

where r_o is the distance between the bound state and the activation state along the reaction coordinate. k_{off} and r_o are characteristic parameters for the molecular pair under investigation and are called Bell parameters. These parameters can be extracted from dynamic force spectroscopy experiments by determining the slope and the x-intercept of the curve when unbinding force is plotted against loading rate as shown in figure 3.

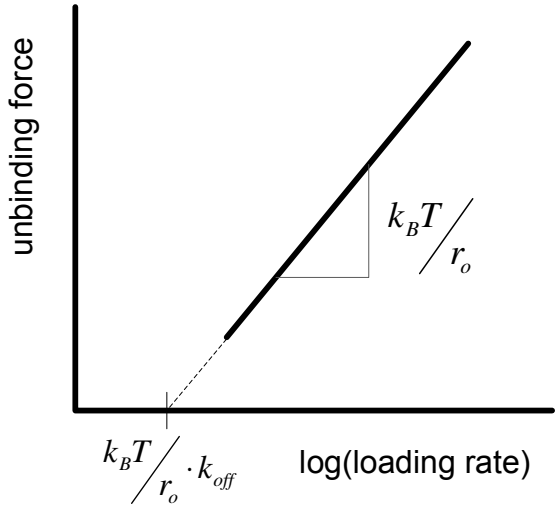

Figure 3. Unbinding force as a function of loading rate. Bell parameters can be determined from the slope and the x-intercept of the curve. Figure is adapted from Evans et al. [14].

The above analysis applies to so-called "slip bonds" for which applied force tilts the energy landscape and lowers the energy barrier. Therefore, applied force lowers the lifetime of the biological bond, i.e. inverse of the kinetic rate of dissociation. There is

also another type of biological bond, called “catch bond”. Catch bonds behave counter-intuitively, such that applied force prolongs lifetime [15, 16].

Improving AFM Based Biomolecular Force Spectroscopy Instrumentation

The methods and experimental details for biomolecular force spectroscopy are well summarized in several review articles [7, 17-19]. Before going into details of AFM instrumentation, other techniques commonly used for single-molecular experiments are summarized here for the sake of completeness.

Biomembrane force probes (BFP), optical tweezers (OT) and magnetic tweezers are the most commonly used instruments for force spectroscopy. A micrograph of a BFP setup is shown in figure 4(a) where a functionalized glass micro-bead (labeled as “probe”) is attached to red blood cell (RBC) that is trapped at the tip of a pipette. In a typical experiment, the probe is driven into and out of contact with the other functionalized bead (labeled as “target”) and the interaction forces are detected by measuring the deformations of RBC using a CCD camera. Optical tweezers, schematically shown in figure 4(b), employ laser light to hold and drive a functionalized probe bead against an immobilized target bead. Similarly, magnetic tweezers use magnetic force to steer a paramagnetic functionalized bead against a functionalized target surface as schematically shown in figure 4(c).

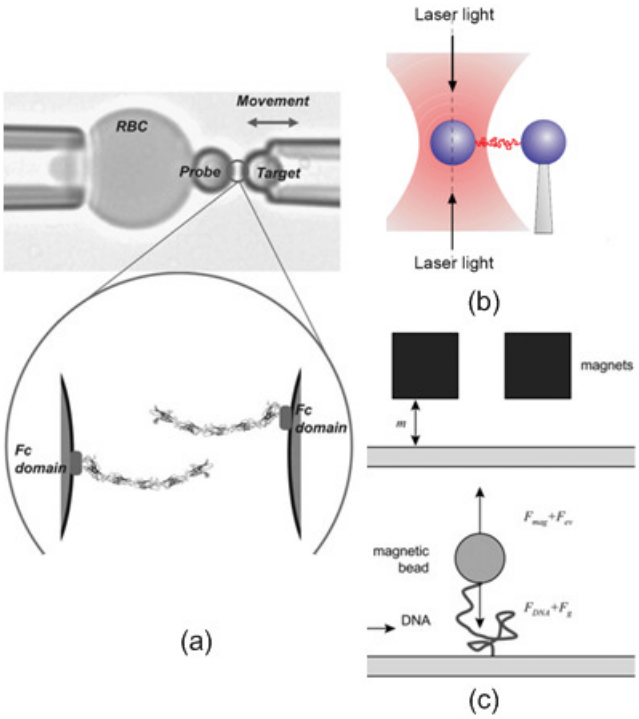

Figure 4. Different techniques for single-molecule measurements. (a) Micrograph of a biomembrane force probe, from Bayas et al. [20]. Schematics of (b) optical tweezers, from Kellermayer et al. [21] and (c) magnetic tweezers from Kruithof et al. [22].

Clausen-Schaumann et al. compared the use of AFM for biomolecular force measurements along with the other techniques: magnetic beads, optical tweezers, microneedles, and biomembrane force probes in terms of force resolution and dynamic range as summarized in table 1 [17]. Although the other methods can provide higher force resolution, AFM offers higher dynamic range and versatility.

Table 1. Comparison of force and dynamical range provided by different tools for single-molecular experiments. Table is adapted from Clausen-Schaumann et al. [17].

	AFM	**BFP**	**LT**	**MT**
Force range (pN)	>1	0.5 – 1000	0.1 – 150	0.01 – 100
Dynamical range	>10 µs	>1 ms	>10 ms	>1 s

Commercially available AFM cantilevers provide force resolution of few pN with 1 kHz bandwidth. The force resolution can be improved by reducing the cantilever's coefficient of viscous damping. Consequently, smaller cantilevers can measure smaller forces since they have smaller viscous damping [23, 24]. On the other hand, if one reduces the lateral dimensions of the cantilever to achieve low thermal noise in fluids, the thickness needs to be decreased to simultaneously keep the spring constant at its original value. These cantilevers come with their own limitations. In addition to microfabrication constraints, smaller cantilevers need sophisticated optics and special optical lever sensors that may not perform very well with larger cantilevers [25]. Thus, novel force sensors with low inherent noise will greatly expand the capability of AFM to probe wide range of biomolecules and to investigate interesting phenomena such as catch bonds [15].

Higher dynamic range for actuation and detection is required along with higher force resolution for improved dynamic biomolecular force spectroscopy. Dynamic force spectroscopy measurements by varying the loading rate on the bio-molecules allow researchers to investigate the shape of the energy landscape of the probed molecular

system [26]. The pulling speed of the cantilever by using a piezo actuator determines the loading rate in a conventional AFM system. Hydrodynamic drag force on the moving cantilever increases with the pulling speed which sets the maximum pulling speed before the hydrodynamic drag force becomes larger than the interaction force to be measured. This level is usually between 10 and 30 μm/s for most of the cantilevers in use, but higher pulling speed capability is required for complete understanding of energy landscapes [27]. Thus, novel actuators that allow higher loading rates with minimal hydrodynamic drag forces on the force sensors are highly desirable.

The AFM technology is well established for single cantilever operation, however the parallel operation of array of cantilevers is still challenging, especially in fluid. Parallel optical detection of cantilevers in air with a single actuator has been demonstrated for imaging applications [28]. A parallel sequential readout method for passive cantilevers in fluid has also been developed for monitoring relatively slow chemical processes [29, 30]. On the other hand, both parallel actuation and force sensing capabilities are required for measuring interaction forces precisely to obtain statistically significant data in biomolecular force spectroscopy. Piezoelectric technology integrates both actuators and detectors to array of cantilevers for data storage and imaging applications [31-34]. These devices can be difficult to isolate in fluid and require complex fabrication processes. Researchers have also developed a 2D array of cantilevers that can be individually actuated by slicing a bulk piezo actuator, but this is not suitable for batch fabrication and the readout of such an array may need a complex system [35].

Micromachined Membrane Probes for AFM Applications

Cantilevers are not the only structures suitable for AFM as a force sensor. Figure 5 shows novel membrane and clamped-clamped beam structures introduced for AFM applications. These probes have electrostatic actuation and integrated diffraction-based optical interferometric displacement detection capabilities. The use of these probes, called force-sensing integrated readout and active tip (FIRAT), has been demonstrated for various applications. Membrane and clamped-clamped beam structures can be designed with high bandwidth as compared with slower commercially available cantilevers. Moreover, broadband actuation of these probes is possible with the integrated electrostatic actuators as compared with the piezo tube actuators. Onaran et al. presented the system setup developed for FIRAT probes and used these probes for fast imaging and for capturing transient interaction forces between the probe tip and the sample [36]. In addition to high bandwidth of the probes, interferometric readout provides higher displacement sensitivity which is important for nondestructive material characterization. Balantekin et al. demonstrated the use of these probes for quantitative material characterization [37].

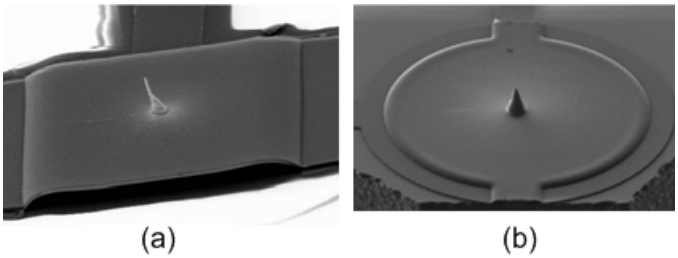

Figure 5. SEM images of FIRAT probes made of aluminum and comprising (a) a clamped-clamped beam, and (b) a membrane on quartz substrate.

The focus of this thesis is on a version of FIRAT probes for biomolecular mechanics measurements. Figure 6 shows a schematic of a membrane-based active probe built on top of a transparent substrate. The main structure is a surface micromachined dielectric membrane with a buried metal layer serving as the top electrode. Under the membrane, there is a patterned metal layer (bottom electrode) on top of the substrate. Electrostatic forces actuate the membrane by using the top and the bottom electrodes. The actuation range of the membrane can be controlled with the gap height between the membrane and the substrate as it is typically one-third of the gap. Within this range it is possible to actuate the membrane fast since the speed is only limited by the membrane dynamics.

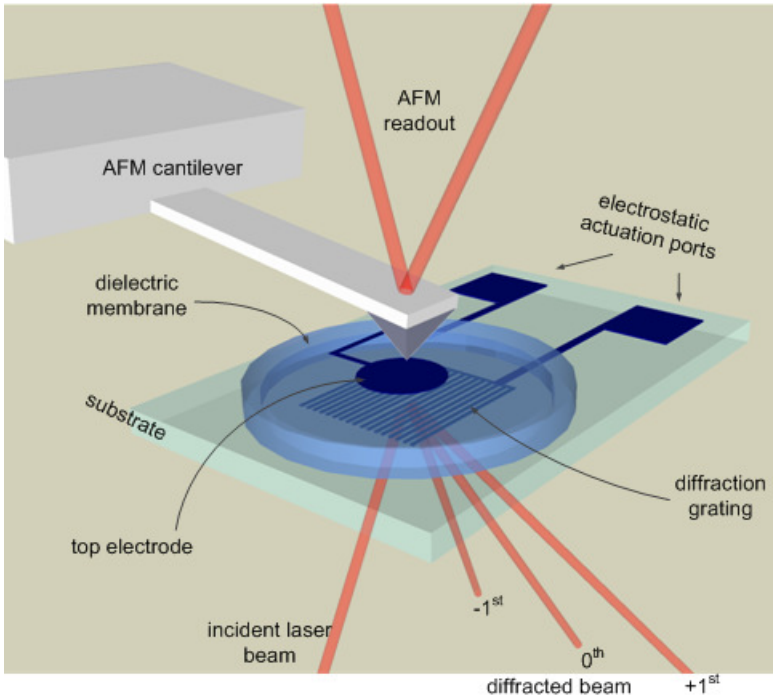

Figure 6. Schematic of membrane probe with an AFM cantilever coupled to it in a typical experimental setup.

Optical interferometric displacement detection capability is integrated to the probe by patterning the bottom electrode on the substrate as a diffraction grating. This phase sensitive diffraction grating structure enables displacement measurement with the sensitivity of a Michelson interferometer. When the membrane is illuminated from backside with a coherent light source, the reflected light is separated into diffraction orders as shown in figure 6. The light reflected directly from the diffraction grating interferes with the light reflected from the membrane. Thus the intensity of light at the diffraction orders varies sinusoidally as a function of the gap between the membrane and the grating. A simple scalar analysis of the reflected light shows that the optical signal in the 0^{th} order is complementary to the higher diffraction orders [38]:

$$I_0 = I_{in} \cos^2\left(\frac{2\pi d}{\lambda}\right), \quad I_{\pm 1} = \frac{4I_{in}}{\pi^2} \sin^2\left(\frac{2\pi d}{\lambda}\right) \tag{4}$$

where I_{in} and λ are the intensity and wavelength of incident light, respectively, and d is the gap height. Separate photodetectors measure the intensities of the zeroth (I_0) and first ($I_{\pm 1}$) diffraction orders; thus it is possible to implement a differential detection architecture using these photodetector outputs to increase the displacement sensitivity and eliminate the common mode noise components such as laser intensity noise.

Figure 7 shows the variation of light intensities in the diffraction orders as a function of gap height. The small dots on the optical curves are where the sensitivity is maximum. Here the sensitivity is defined as the amount of change in light intensities due to a unit change in gap height. Maximum sensitive points correspond to odd multiples of

$0.125 \times d/\lambda$. Probes can be used as sensitive linear sensors around these operating points. This can pose a limitation on the detection range. To overcome this shortcoming an improved probe structure with quadrature phase-shifted dual gratings that provides good detection sensitivity for small displacement for the whole range of membrane displacement has also been developed [39]. It is also possible to employ two-wavelength laser readout to extend the detection range [40].

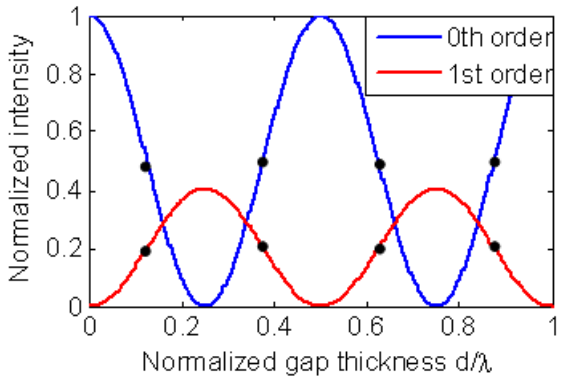

Figure 7. Variation of normalized light intensities in 0^{th} and 1^{st} diffraction orders as a function of normalized gap thickness.

Figure 6 also shows the typical experimental setup for a force spectroscopy measurement where a force measuring soft AFM cantilever is coupled to the probe membrane in immersion. Both the cantilever and the membrane are functionalized with appropriate molecular layers. With a relatively stiff membrane, the probe is used as a microscale actuator to bring the tip and the membrane in and out of contact, and the displacement readout can be used to accurately control the extension of the molecules through a feedback loop. With a soft membrane, the probe, itself, is used as the force sensor where the membrane displacement due to biomolecular interaction forces is

directly detected, eliminating the need for another force sensor such as the AFM cantilever.

In this thesis, active probes made of silicon nitride/oxide and parylene is discussed in detail. Design, fabrication, modeling and characterization efforts are described. The fabricated devices have been used in different biological experiments and the results are presented in this thesis.

CHAPTER 2

DESIGN OF MEMBRANE PROBES

Design of probe actuator

The design effort for the probe actuator is focused on providing sufficient displacement range and the speed needed for the experiments. As an actuator, the probe needs to have enough displacement range for single molecule experiments such as molecular pulling and force-clamp force-spectroscopy. A displacement range of 1 μm is sufficient to probe a variety of protein-protein interactions, ligand-receptor interactions, and antibody-antigen interactions [41]. This figure is also suitable for certain protein folding experiments.

It is also desirable to provide the displacement range of the probe within a certain frequency bandwidth for dynamic experiments. Pulling speed of commercially available cantilevers is limited to 10 μm/s while higher pulling speeds with dynamic force spectroscopy experiments are required for complete understanding of force spectra [27]. The speed limitation comes from increased drag force on the cantilever that becomes comparable to biological interaction forces. As will be shown later, pulling speeds in the order of 10^4 μm/s, and molecular pulling rate of 10^{10} pN/s (with 1 N/m stiffness) are possible with an actuation bandwidth of 10 kHz in liquid with membrane probes. Using membrane actuators for surface-actuation of cantilevers also has certain benefits in minimizing drag force and this will be presented in detail later.

Parallel-plate type electrostatic actuators can be designed to meet these required specifications. Moreover, it is possible to integrate an electrostatic actuator to the membrane probe without a need for external component and such an actuator is relatively simple to operate. A simple schematic of the actuator integrated to a membrane probe is shown in figure 8.

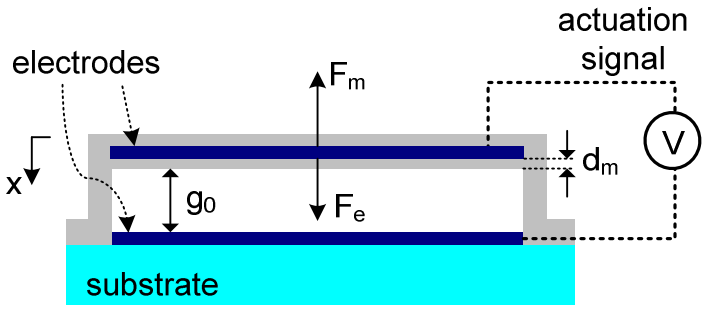

Figure 8. Schematic of a parallel-plate electrostatic actuator integrated to the membrane probe.

The simplest model for the parallel-plate electrostatic actuator shown in figure 8 is the lumped model where the electrostatic force, F_e, is balanced with the mechanical restoring force, F_m. Here, the bottom electrode is fixed and the top electrode, embedded into the membrane, is movable. Thus the total capacitance when the membrane is displaced by an amount of x is:

$$C(x) = \varepsilon_0 \frac{A}{g_0 + \frac{d_m}{\varepsilon_r} - x} \tag{5}$$

where ε_0 is the permittivity of the free space, A is the area of the electrode, and g_0 is the initial gap height. d_m/ε_r term in the denominator captures the effect of the dielectric layer

between two electrodes, where d_m is the thickness of the layer and ε_r is the relative permittivity of the dielectric material. It is possible to store electrical energy, *E(x)*, in such a capacitor when electrical potential difference is applied between its electrodes. Consecutively, the electrostatic force, F_e, can be defined as *dE(x)/dx* as follows:

$$E(x) = \frac{1}{2} C(x) V^2 \tag{6}$$

$$F_e(x) = \frac{dE(x)}{dx} = -\frac{\varepsilon_0 A V^2}{2\left(g_0 + \frac{d_m}{\varepsilon_r} - x \right)^2} \tag{7}$$

A first order lumped model for the membrane assumes a spring (*k*), a mass (*m*), and a damping (*b*) parameter and each of these parameters contributes to the mechanical force, F_m, that balances F_e, as shown in equation 8.

$$F_e(x) = F_m(x) \Rightarrow m\frac{d^2x(t)}{dt^2} + b\frac{dx(t)}{dt} + kx(t) - \frac{\varepsilon_0 A (V(t))^2}{2\left(g_0 + \frac{d_m}{\varepsilon_r} - x(t) \right)^2} = 0 \tag{8}$$

Equation 8 is a nonlinear differential equation of second order. However the displacement range of the actuator can be determined by considering a time independent drive signal and solving the equation only for the static response. The stable displacement range for the actuator extends towards the point where the electrical force gradient becomes larger than the mechanical force gradient. This point is called pull-in point where the top electrode suddenly collapses on top of the bottom electrode. The associated voltage and the displacement values with pull-in point are given as follows [42]:

$$V_{pull-in} = \sqrt{\frac{8k\left(g_0 + \frac{d_m}{\varepsilon_r}\right)^3}{27\varepsilon_0 A}} \tag{9}$$

$$x_{pull-in} = \frac{g_0 + \frac{d_m}{\varepsilon_r}}{3} \tag{10}$$

Despite the simplicity of the given lumped model, it is powerful to determine the displacement range and the required voltage. The range depends on the initial gap height and is approximately one-third of it. For example a membrane with 4.5 μm thick initial gap height would have a range of 1.5 μm, and meeting the previously mentioned requirements. Such a circular membrane with 300 μm diameter and a spring constant of 150 N/m would require about 150 V for full range operation. Obviously the voltage requirement for the full range reduces as the gap height reduces: e.g. a 2.5 μm gap height membrane would only require 62 V for a full range of 830 nm. So, increasing the range comes at the expense of high voltage requirement. In addition to that, increasing gap height requires a thicker sacrificial layer and the processing steps following the sacrificial layer become more difficult due to side coverage issues. This becomes more important when thinner layers are needed.

It is also possible to extend the stable displacement range of electrostatic actuators by simply segmenting the electrodes without a need for increased gap heights. This method was introduced by Hung et al. to increase the range of a tunable reflective diffraction grating [43]. Segmented-electrode actuation method relies on applying electrostatic force to only a part of the structure and displacing the rest of the structure as a lever. The method is applicable to any parallel plate type electrostatic actuators.

Consecutively, displacement range of membrane probes can be extended using so called "leveraged bending" method when the bottom and the top electrodes of the actuator is segmented as schematically shown in figure 9.

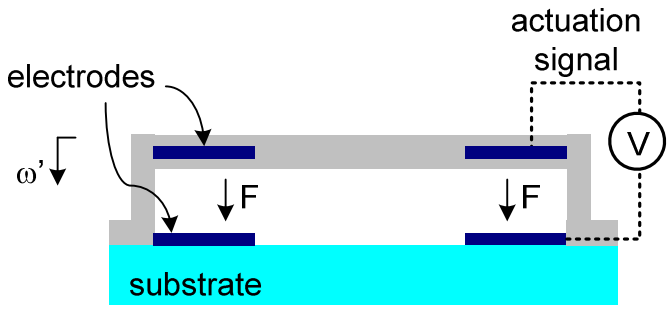

Figure 9. Schematic of a segmented-electrode electrostatic actuator to increase the stable displacement range.

Modeling of a segmented electrode actuator is more complex than a simple parallel plate actuator and requires solving equation 11, governing the electrostatic-elastic system schematically shown in figure 9 [44].

$$\rho h \frac{\partial^2 \omega'}{\partial t'^2} + a \frac{\partial \omega'}{\partial t'} - \mu \nabla^2 \omega' + D \nabla^4 \omega' = -\frac{\varepsilon_0}{2} |\nabla \phi|^2 \tag{11}$$

where ρ is the density, h is the membrane thickness, a is the damping constant, D is the flexural rigidity and ω' is the displacement of the membrane. Φ is the electrostatic potential and it is required to compute the potential everywhere on the membrane region including the fringing fields. The term on the left-hand side of the original equation including the term μ captures the effect of tension on the membrane.

Alternatively, finite element simulations with coupled field (electrostatic-elastic) capability can be used to determine the stable actuation range of a segmented electrode actuator. Results of the simulations for membranes with different geometries obtained with ANSYS are shown in figure 10. All the membranes shown here are 300 µm diameter ones made of parylene and donut shaped aluminum electrodes. The inner diameter for the donut shape is 120 µm. Membranes with different thicknesses and gap heights were simulated for comparison purposes.

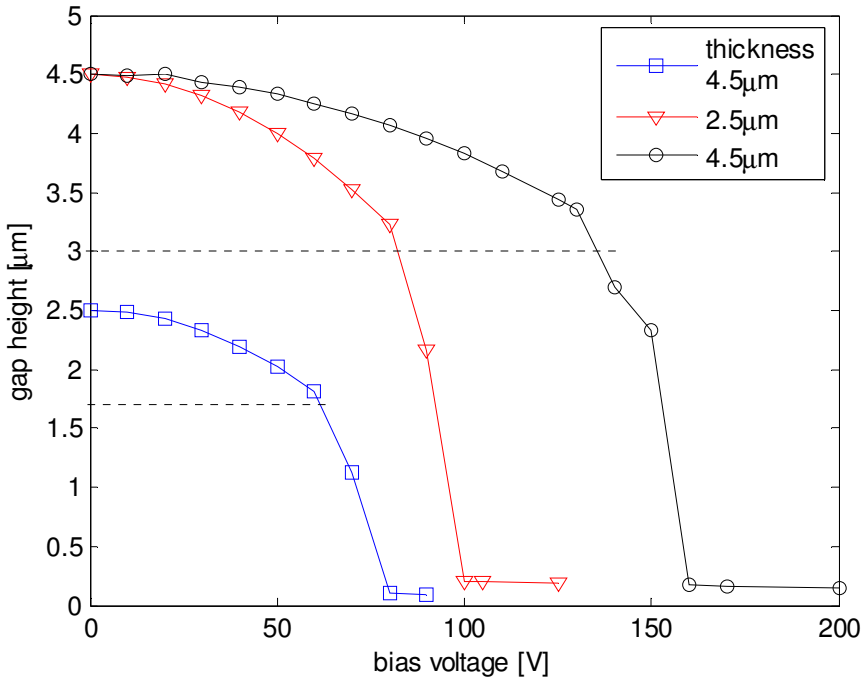

Figure 10. FEM simulation results obtained with ANSYS to determine stable displacement range of membranes. Dashed lines specify the pull-in point for simple parallel-plate actuators with the same gap heights for comparison.

The FEM results show that a stable actuation of 1.5 µm is possible even with a 2.5 µm gap height membrane. This is an improvement of two-times when compared to a

simple parallel-plate type actuator with the same gap height. The displacement range of the 2.5 μm gap height membrane can be doubled with a gap height of 4.5 μm. Such a device can be used for a variety of protein unfolding experiments. For the gap height of 4.5 μm, two different membrane designs with different thicknesses were simulated. Obviously, the thicker membrane (4.5 μm thick) is stiffer and requires more voltage for the full displacement range. The spring constant of this membrane was calculated ~250 N/m. If the thickness of the membrane is reduced to 2.5 μm, then the spring constant reduces to ~50 N/m, hence the maximum required voltage can be limited to 100 V.

Thicker membranes have benefits in fluid operation. Dielectric layer on top of the membrane protects the top electrode from electrolysis, a significant problem for electrostatic actuators in fluid. If water gets into contact with the electrodes due to defects such as cracks or pin-holes, electrolysis occurs and damages the electrodes by etching the metal layer. At 25˚C and 1 atm electrolysis starts if the potential difference between the electrodes is larger than 1.23 V [45]. Considering the required voltage levels for the membrane actuator, this poses a potential problem. Obviously improving fabrication process to minimize defects helps with this problem. Alternatively, new drive schemes for in fluid operation based on modulating the drive signal with a square wave have been introduced [46, 47]. This method is called RMS operation and performed by modulating the drive signal with a zero-mean, high frequency square wave. If the frequency of the square wave is above the resonant frequency of the actuator, the actuator responds only to the envelop of the input signal. Zero-mean signal guarantees electrolysis-free operation and it has been experimentally demonstrated that the RMS operation is almost identical to DC operation under certain conditions [46].

Use of the RMS operation with the membrane probes allows reliable in-liquid operation even with thinner membranes so that the voltage requirement can be kept moderate. Modeling of RMS operation requires the solution of equation 4 with dynamic elements *m* and *b* as well as static element *k*. Senturia presents an implementation of the equation in Simulink/Matlab environment as shown in figure 11 [42]. This simple model captures the first-order dynamic behavior of the actuator when used with RMS operation method.

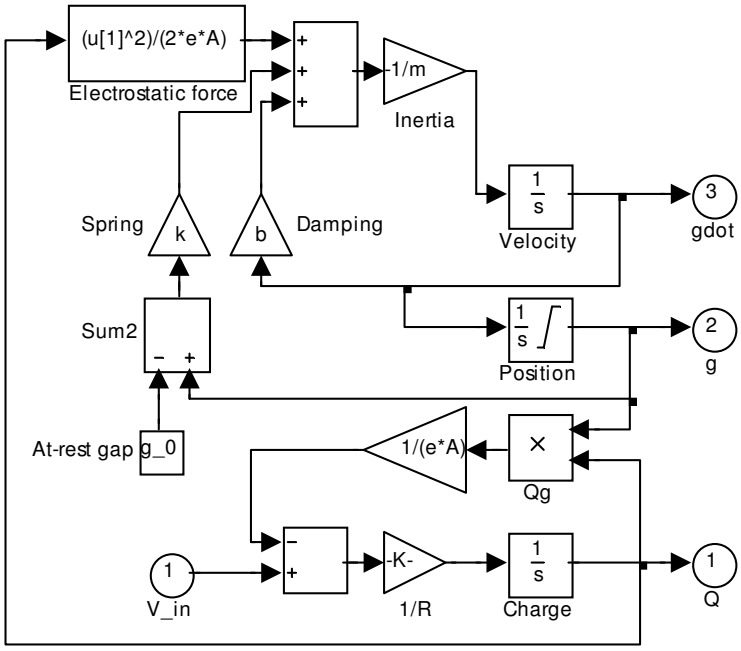

Figure 11. First-order lumped model of the electrostatic actuator implemented with Simulink/Matlab.

The model was run for two cases. The first run was with "normal" operation where the drive signal was directly applied to the actuator and the second one was with RMS operation when the drive signal was modulated with a square wave. The parameters for a 300 µm diameter membrane was fixed as $k=150$ *N/m*, $m=5x10^{-15}$ *kg*, $b=5x10^{-5}$ *N/m-*

s. The simulated response of the membrane to an arbitrary drive signal is shown in figure 12(a). The resonant frequency of the membrane is ~550 kHz; hence the drive frequency is well below the resonant frequency guaranteeing linearity. Note that the peak displacement of the membrane is ~300 nm and it moves at twice of the drive frequency.

The drive signal was then modulated with 1 MHz square wave and applied to the membrane. The transient response is shown in figure 12(b). Since the frequency of the square wave is above the resonant frequency, the membrane cannot follow the square wave but responds to the envelope of the signal. The displacement curve is almost identical to the one with that of the normal operation.

The behavior of the membrane in fluid with this drive scheme depends on the modulation frequency due to the frequency dependence of the dielectric constant of water. This becomes more important with segmented-electrode devices where fringing fields affect the behavior of the actuator more. Thus real devices should be characterized well in fluid before biological experiments.

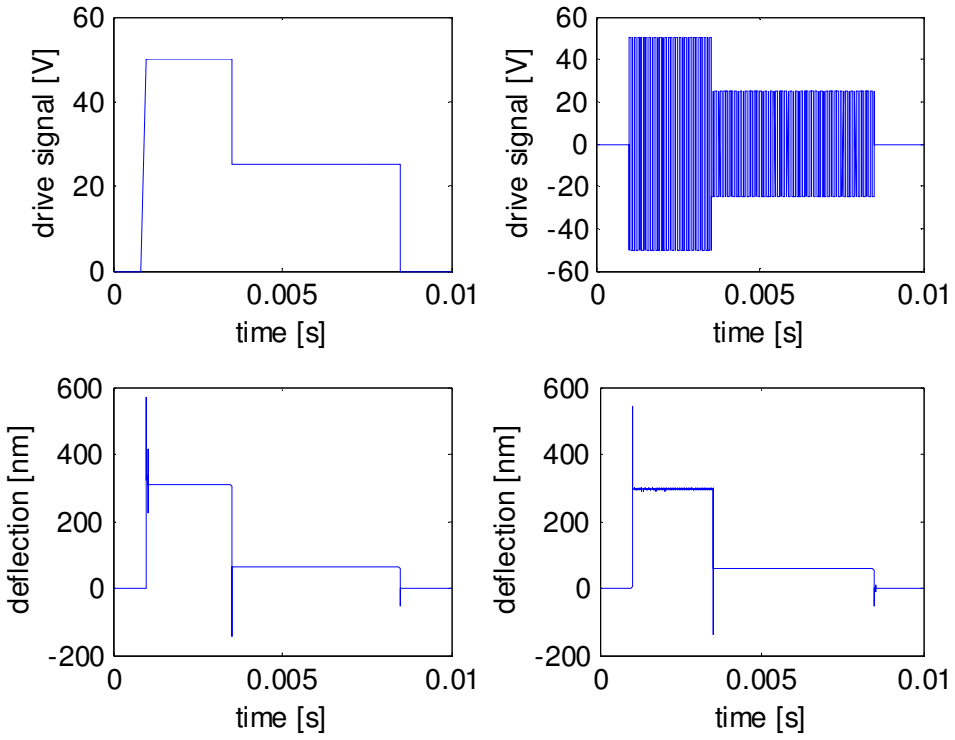

(a) (b)

Figure 12. Simulated transient response of membrane actuator (a) with normal operation (b) with RMS operation.

Squeeze Film Damping

The first-order lumped model used so far is simple yet powerful to capture dynamics of the membrane probe. One major limitation of the model is that the lumped elements are frequency independent. However the damping force, so called "squeeze film damping, due to the surrounding air in MEMS cannot be explained with these elements. Squeeze film damping force is observed when a plate oscillates in the vicinity of another surface where the surfaces are separated by a gas film. The contribution of gas damping becomes dominant if the thickness of the gas film is smaller than one-third of the width

of the plate [48]. This condition holds for most of the MEMS devices operating at atmospheric pressures and this phenomenon has been studied extensively [48-52].

The behavior of gas film is governed by well-known Reynolds equation and for MEMS devices, inertial effects and temperature variations are usually negligible. Thus the Reynolds equation is reduced to [48]:

$$\frac{\partial}{\partial x}\left(\rho\frac{h^3}{\mu}\frac{\partial P}{\partial x}\right)+\frac{\partial}{\partial y}\left(\rho\frac{h^3}{\mu}\frac{\partial P}{\partial y}\right)=12\frac{\partial(h\rho)}{\partial t} \tag{12}$$

where P is the pressure on the film, μ is the coefficient of viscosity, ρ is the density, and h is the thickness of the film.

Squeeze film damping force, due to the pressure on the gas film, can be divided into two components for analysis purposes; one component associated with the squeezed flow of gas in and out of the movable structure, and the other component associated with the compressibility of the gas film when the structure moves against it. Forces due to the flow of gas can be modeled with a damping element while the elastic forces due to the compressibility of the gas film can be modeled with a spring element. These elements are frequency dependent. At lower speeds of movement, the gas film is not compressed significantly, thus viscous damping force dominates. However at higher speeds, the gas film is basically compressed as it can find no time to flow, thus the film behaves more like an elastic spring. Consequently, the membrane can be modeled using the equivalent circuit shown in figure 13. Note that the spring (k_{air}) and the damping (b_{air}) parameters assigned for the gas film are now frequency dependent.

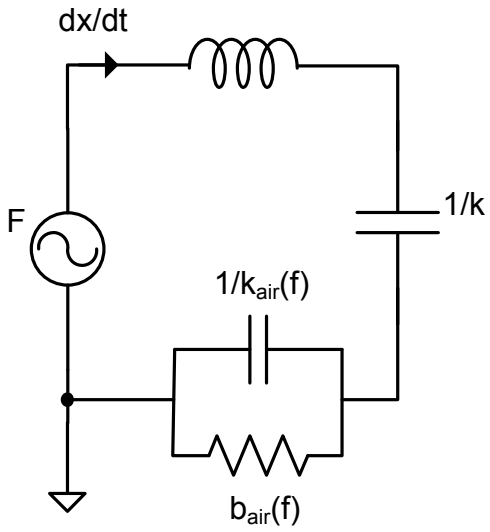

Figure 13. Equivalent circuit with frequency-dependent elements to model membrane behavior including squeeze film damping.

Modeling of membrane dynamics requires the extraction of damping parameters k_{air} and b_{air}, which can be difficult for real membranes due to geometrical complexities. For illustration purposes, the effect of geometry on the behavior of gas film is shown in figure 14. In ANSYS; first, a gas film under a membrane with an etch-hole is defined. Then, a constant velocity vector at an arbitrary speed is applied on top of the gas film to simulate the membrane movement against the gas film. The velocity profile within the gas film is shown in figure 14. Note that the end of the etch hole is left open, thus is set to ambient pressure. Higher amplitude velocity vectors towards the end of the etch hole clearly shows the flow of the gas in this part of the structure. That is an indication of viscous damping associated with the gas film. On the other hand, the velocity vectors under the membrane area are smaller in magnitude; even vanish towards the other end of the geometry. That clearly points out the fact that the gas film is compressed at these regions. Hence the film behaves as an elastic spring.

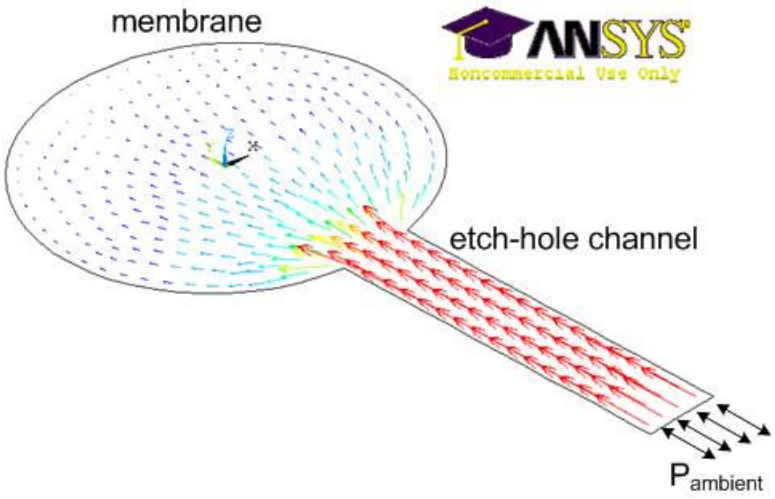

Figure 14. Vectors showing the velocity profile within a gas film trapped under a membrane with an etch hole obtained by FEM simulations with ANSYS. The end of the etch-hole is open, thus set to ambient pressure.

Reviewing the distribution of velocity vectors shown in figure 14 indicates that an accurate model should take into account the geometry of the structure and such a model can become quite complex even with simple geometries. In ANSYS, this problem is treated based on the analogy between the equation 8 and a similar 2-D heat transfer equation [53]. For any given geometry, matrices of k_{air} and b_{air} can be extracted for a fixed frequency of motion and these parameters can be used with the model shown in figure 13.

This method is used to predict dynamic response of membrane actuators with different geometries. Frequency response of a 50 μm diameter membrane, made of 1 μm thick parylene and 100 nm thick Au, with a gap of 2.5μm gap is shown in figure 15(a). The spring constant of a stress-free membrane with these dimensions is calculated to be 112 N/m, and the spring constant associated with the gas film under the membrane

becomes comparable with this value at the actuation frequency of 10^5 Hz. The spring constant and the coefficient of viscous damping due to the gas film calculated with FEM simulations are shown in figure 15(b-c). The effect of squeeze film damping is apparent for actuation frequencies $>10^4$ Hz, deteriorating the membrane response at higher frequencies.

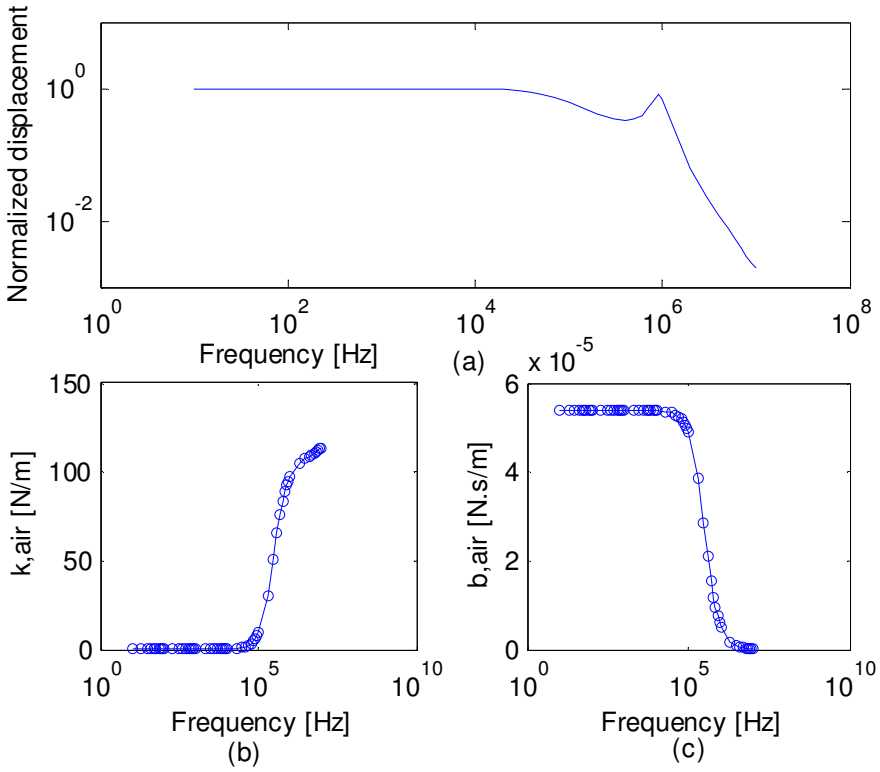

Figure 15. (a) Frequency response of a 50 μm diameter membrane with a gap of 2.5 μm (membrane made of 1 μm thick parylene and 100 nm thick Au). (b) Spring constant and (c) viscous damping parameters associated with the gas film under the membrane with respect to the frequency of motion.

This membrane, initially designed to have a resonant frequency in air at ~1 MHz, cannot be used effectively beyond 10 kHz due to squeeze film damping effect. Obvious

solution to overcome this problem is to increase the gap height. Figure 16 shows the dynamics of the same membrane for a gap height of 5 μm. Increasing the gap height allows the membrane actuation until its resonant frequency. Moreover, squeeze film damping parameters help controlling the quality-factor of the membrane for linear operation near its resonant frequency.

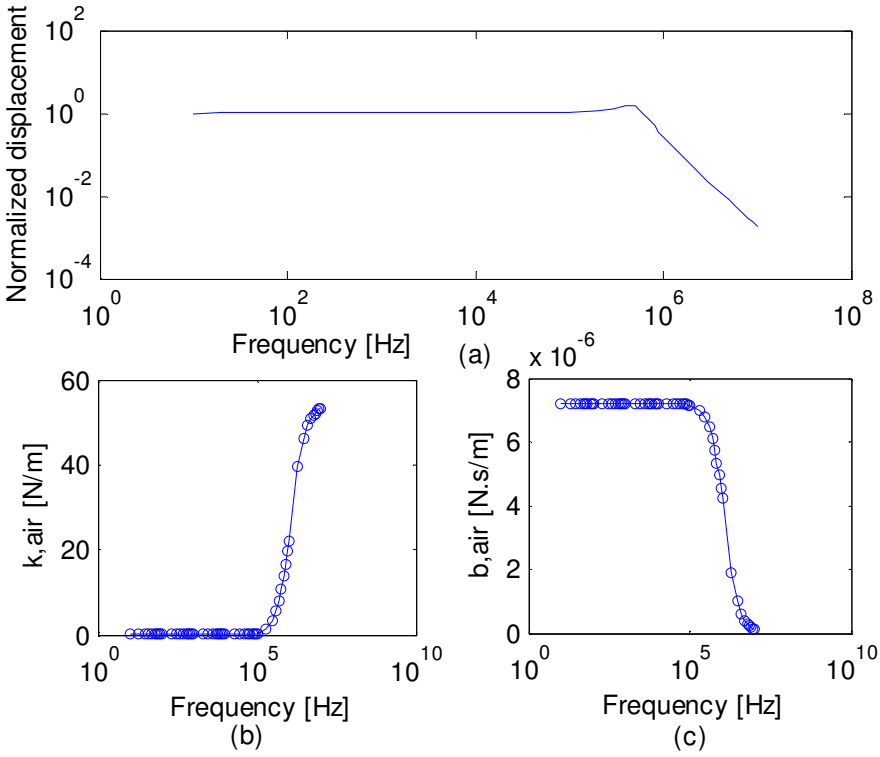

Figure 16. (a) Frequency response of a 50 μm diameter membrane with a gap of 5 μm (membrane made of 1 μm thick parylene and 100 nm thick Au). (b) Spring constant and (c) viscous damping parameters associated with the gas film under the membrane with respect to the frequency of motion.

Design of probe sensor

The models presented so far to design probe actuators can also be used for the design of probe sensors. The design focus for the probe sensor is to deliver the required force sensitivity to probe molecular interactions. The design specification for the probe sensors can be briefly noted as a minimum detectable force of 1 pN with 1 kHz bandwidth in fluid. This figure allows the use of membrane probes to measure the interaction forces between pairs of a variety of biomolecules. Diffraction grating based interferometer architecture provides sub-pm displacement sensitivity with stiff membrane structures with this bandwidth [54]. Thus this method of detection is suitable to meet the design specifications with well designed membranes. Design of membranes should maximize SNR by considering major noise sources, i.e. shot noise in the photodetectors, thermo-mechanical noise of the mechanical structure, electronics noise and laser noise.

It is desirable to have stiff membranes as actuators since the effect of squeeze film damping diminishes with increasing mechanical stiffness. However for force sensing applications, the stiffness of the membrane should be to increase signal levels. On the other hand, given the microfabrication constraints, reducing the stiffness usually means larger membranes; hence increased thermo-mechanical noise. So, the stiffness of the membrane should optimize SNR effectively without letting the sensitivity be dominantly limited with thermo-mechanical noise.

When the mechanical stiffness is reduced to 1-10 N/m level, the elastic spring introduced by the gas film under the membrane matches this level at lower frequencies. Considering the membrane analyzed in figure 16, now with a diameter of 150 μm instead

of 50 μm, illustrates this fact. The spring constant of such a membrane is calculated to be 12 N/m and is suitable for detection applications. Figure 17(a) shows the calculated frequency response of this membrane. Although the nominal resonant frequency of the membrane, calculated to be 170 kHz, it shifts to higher frequencies due to the increased stiffness introduced by the gas film. Moreover, the sensitivity of the probe is not constant from 1 kHz up to the resonant frequency. The stiffness of the air under the membrane becomes comparable to that of the mechanical structure for frequencies larger than 1 kHz, thus altering the frequency response of the membrane. When used for detection, data inversion is needed to accommodate the change in sensitivity.

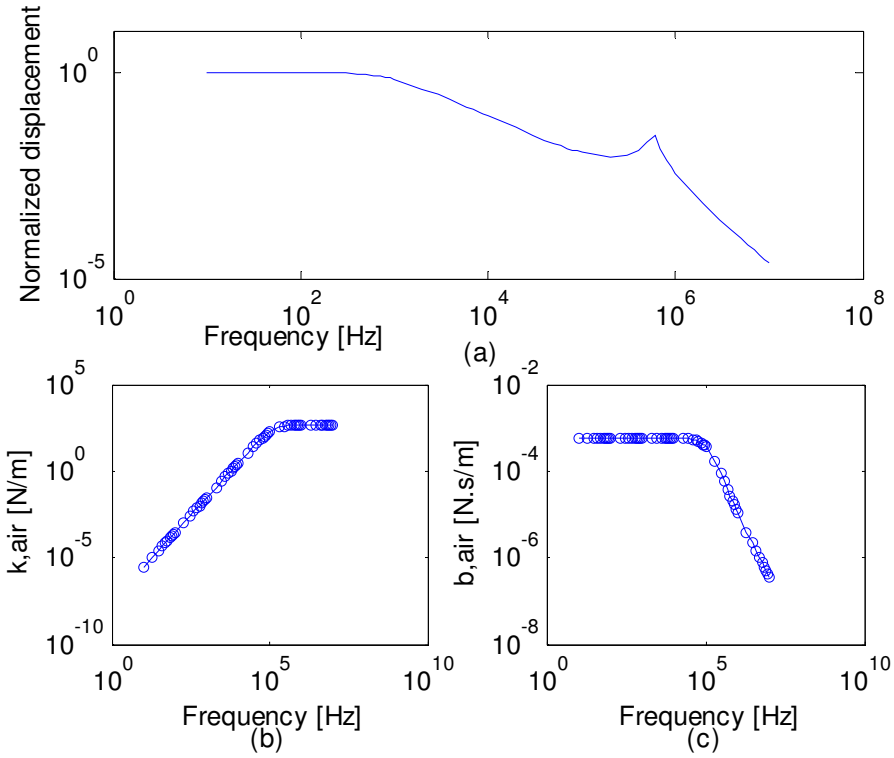

Figure 17. (a) Frequency response of a 150 μm diameter membrane with a gap of 5 μm (membrane made of 1 μm thick parylene and 100 nm thick Au). (b) Spring constant and (c) viscous damping parameters associated with the gas film under the membrane with respect to the frequency of motion.

The membranes with smaller spring constant will need larger gap heights to control the effect of squeeze film damping, but increasing the gap height beyond 5 μm is not practically reasonable. Hence it is strongly desirable to eliminate the effect of gas damping underneath the membrane.

In summary, design of probe actuators and sensors are described in previous sections. Design consideration for better probe actuators and better probe sensors does not always overlap when the uniform-membrane structure presented so far is used. In addition, the effect of gas damping is shown through FEM simulations. Squeeze film damping is detrimental especially for the probes sensors for which the air stiffness

becomes comparable with mechanical stiffness. Providing a path for the gas film under the membrane to escape will effectively eliminate the effect of gas damping.

Design of optimized non-uniform membrane probe

A non-uniform membrane structure is introduced to overcome the shortcomings of the membranes described so far. This structure can be used to optimize the performance of the actuator and the sensor simultaneously. Schematic of a Si-based non-uniform membrane is shown in figure 18 on which associated parts of the membrane are labeled.

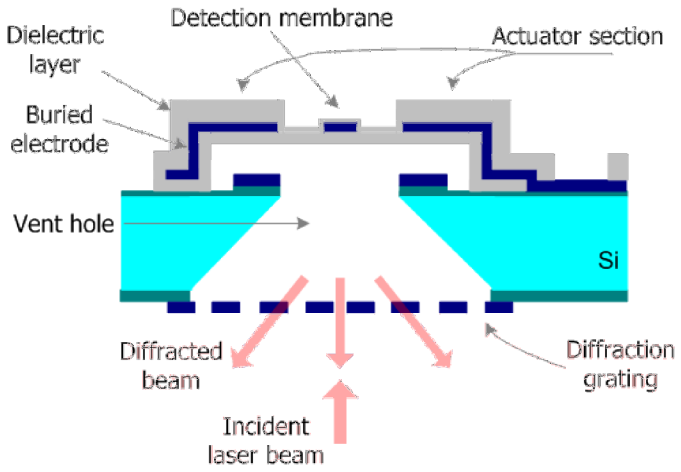

Figure 18. Schematic cross-section of probe structure highlighting the sections forming the membrane.

The side of the membrane is the actuator section as it forms parallel-plate type electrostatic actuator integrated to the probe. The thicker top dielectric layer on the actuator section provides better insulation in fluid operation by it preventing electrolysis

when the buried electrode is electrically excited. The thicker actuator section also makes a stiff actuator with less displacement noise and with high resonant frequency enabling fast pulling experiments. These come at the expense of higher, but reasonable, voltage levels needed to move the membrane. The gap height between the buried electrode and the bottom electrode determines the actuation range of the membrane. Moving the electrodes to the sides extend the actuation range of a uniform parallel-plate type electrostatic actuator for which the range is typically one-third of the gap, as described earlier.

The center part of the probe, which forms the detection membrane for force sensing, is thinner. It is mainly made of dielectric layer with a circular metal layer as the second reflector forming the diffraction grating interferometer that measures the displacement of the membrane.

The vent hole underneath the membrane not only provides optical access for the interferometer but it also allows fabricating free-standing membrane structure since the membrane is released from backside as will be described in the fabrication section. This approach eliminates the need for an etch channel on the front-side of the probe exposed to fluid. Sealing of such etch channels without affecting the operation of the probes may be difficult. The vent hole also equalizes the pressure between both sides of the probe, which in turn makes the probe more immune to ambient pressure gradients that may displace the membrane during the operation. The detection membrane has no rigid structure underneath it due to the vent hole. Thus, the sensing membrane is not affected by the squeezed film damping which would adversely alter the dynamics and thermo-mechanical noise level of the membrane. The non-uniform membrane structure

effectively decouples the design of actuator and the force sensor effectively. When used as a force sensor in fluid it is important to minimize the moving area of the probe as smaller structures encounter lower viscous damping, thus lower thermal mechanical noise.

Detection membrane is used to detect point forces acting at the center of the membrane. Smaller detection membrane makes a good force sensor provided the actuator section does not respond to a point force at the center. Figure 19(a) shows the steady-state response of a 300 μm diameter parylene probe with 120 μm diameter detection membrane to a point force of 100 pN. The displacement profile was obtained with FEM simulations using ANSYS^{TM}. The detection membrane and the actuation section are designed with thicknesses of 0.5 μm and 3 μm, respectively. Center of detection membrane displaces 91 pm, while the deflection of the actuation section is negligible.

The thinner detection membrane is made compliant to increase the force sensitivity. FEM simulations give stiffness of the unbiased membrane to be 1.100 N/m. The detection membrane can be fabricated soft enough for better sensitivity with this approach. It is also important to maintain the same stiffness value when the probe is actuated by applying voltage to the actuator electrodes. The result of the FEM simulation in figure 19(b) shows the membrane profile when the center of the sensor membrane is displaced by 1 μm using the electrostatic actuator. The stiffness of the detection membrane changes – it is actually reduced – only by %2.2. Hence, use of the rigid side electrodes for actuation does not significantly affect the behavior of the sensor membrane, indicating a decoupled sensor/actuator combination.

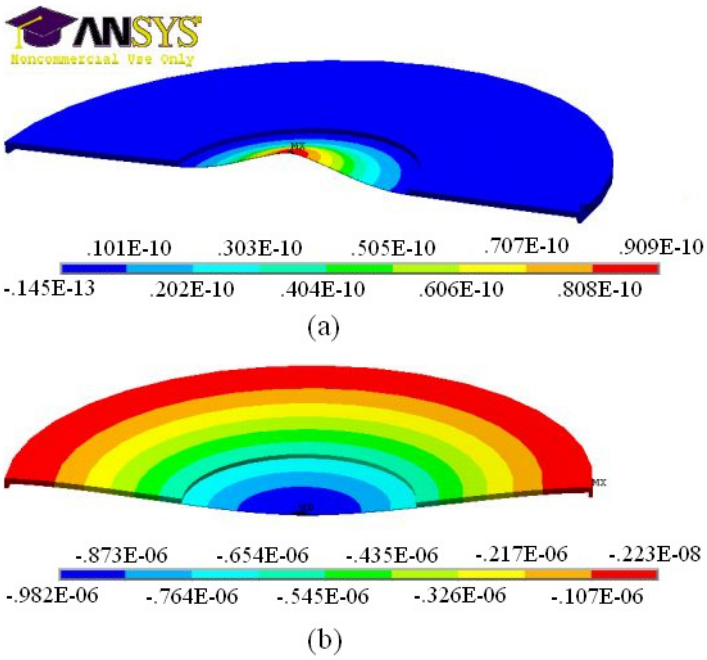

Figure 19. Displacement profile of (a) the unbiased membrane when 100 pN point force is applied at the center, (b) the membrane with applied voltage to the side electrodes to displace the center by 1 μm; obtained with ANSYS. One-half of the membrane is shown.

With this design, dynamics of neither the detection membrane nor the actuator is significantly affected by squeezed film damping. The vent hole under the detection membrane allows free flow of gas and the increased stiffness of the actuator reduces the effect of air stiffening. On the other hand, an accurate model for the membrane dynamics operating in fluid should consider the effect of fluid loading.

Effects of Fluid Loading

The fluid loading on the membrane can be handled by calculating the associated radiation impedance of the acoustic wave propagated into the fluid due to the mechanical vibrations generated by the membrane.

An acoustic port including the radiation impedance, Z_a, can be added to the model given in figure 13 to consider the effect of fluid loading as shown in figure 20. Here the mechanical velocity, *dx/dt*, is coupled to the volume velocity, *q*, and the coupling ratio is simply the area of the transducer, *S*. Note that the squeeze film damping elements are now removed from the model. Instead, a simple damping parameter, *b*, is added to capture loss mechanisms affecting the membrane, such as structural damping or hydrodynamic drag.

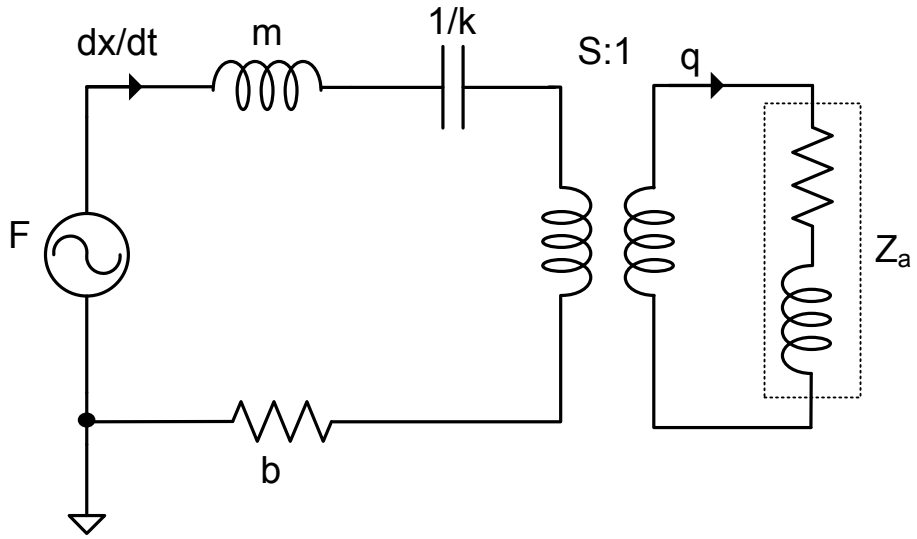

Figure 20. Equivalent circuit for the membrane in fluid. Acoustic domain, modeling fluid loading, is coupled to the mechanical domain with transformer ratio equals to the area of the membrane.

A basic assumption for the membrane in fluid is to consider it as a circular piston for which the associated radiation impedance can be expressed analytically in terms of piston resistance function R_1 and piston reactance function X_1 [55]:

$$Z_a = \frac{\rho_0 c}{S}\left[R_1(2ka) + jX_1(2ka)\right] \tag{13}$$

where ρ_0, c, k, and a are the density, speed of sound, wave number, and the radius of the piston. R_1 and X_1 are expressed with Bessel function of the 1st kind, order 1, J_1, and first order Struve function, H_1, as follows:

$$R_1(x) = 1 - \frac{2J_1(x)}{x} \tag{14}$$

$$X_1(x) = \frac{2H_1(x)}{x} \tag{15}$$

Consecutively, the effect of fluid loading on the dynamics of the membrane will be added mass and damping. Note that additional mass and damping parameters are frequency-dependent as they depend on the wave number.

The mechanical impedance values are calculated for the detection membrane investigated earlier in figure 19. These values with respect to frequency are given in figure 21 for comparison purposes. Any mechanism that causes membrane fluctuation basically introduces dissipation. Hence, hydrodynamic drag affecting the membrane in fluid is assumed as a damping source in the mechanical domain. In a typical experiment,

a membrane is coupled to an AFM cantilever. Thus, the calculation of hydrodynamic drag coefficient should also take into account the presence of the AFM cantilever within the vicinity of the membrane probe. Dagan et al. analytically calculated the drag force on a circular disk when a sphere is brought near the disk [56]. Using this model, the drag coefficient on the disk can be calculated as follows:

$$b = 16 \cdot \lambda \cdot \mu \cdot a \qquad [N \cdot s \cdot m^{-1}] \tag{16}$$

where λ, the hydrodynamic interaction coefficient, is a correction factor depending on the distance between the disk and the sphere normalized to the sphere radius. μ is the viscosity of fluid and a is the radius of the disk. Assuming the membrane and the cantilever as a disk and a sphere, respectively; a first-order approximation for the impedance value associated with the drag force can be calculated as shown in figure 21.

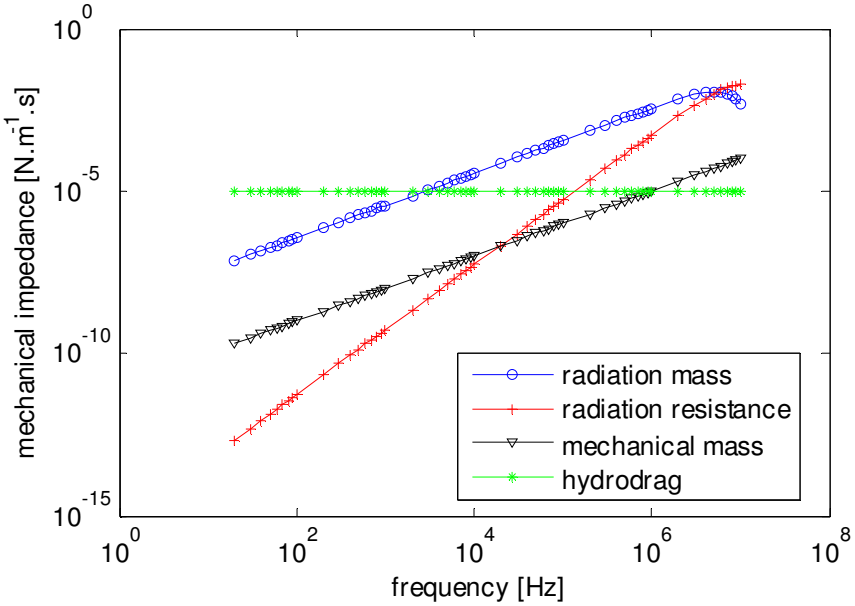

Figure 21. Calculated frequency spectrum of mechanical impedance of the membrane shown in Figure 19 in fluid operation.

Figure 21 suggests that fluid adds significant radiation mass on the vibrating membrane as expected. The effect of radiation resistance, however, becomes important at higher frequencies. At lower frequencies, the dominant damping source is the hydrodynamic drag on the membrane. Hence, increased radiation resistance would adversely affect the higher order modes of the membrane.

Based on the spectra of mechanical impedances, frequency response of the detection membrane can be calculated. Figure 22 shows the normalized frequency response by considering first four radially-symmetric vibration modes of the membrane. For a circular plate, vibration modes are represented as *(m,n)*, where *m* denotes the number of nodal circles and *n* denotes the number of nodal diameters and the mode shapes are well documented [57]. The resonant frequency of the fundamental node is 6.3 kHz and the quality factor is approximately 2.5. So, it is possible to detect displacements

with constant sensitivity in liquid with 1 kHz bandwidth and a reasonable quality-factor; thus meeting the design specifications. Figure 22 also shows that the vibration in higher order modes is well damped due to the increased radiation resistance at higher frequencies.

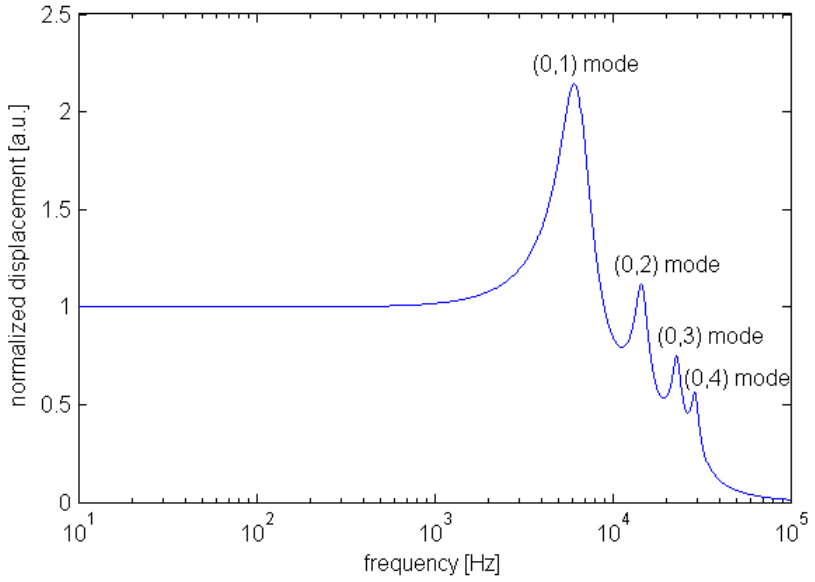

Figure 22. Calculated frequency response of the membrane displacement in fluid based on the mechanical impedance shown in figure 21.

Hydrodynamics of membrane probes in fluid

Radiation impedance analysis together with the fluid damping of equation 16 can be used as a first-order approximation for the effect of fluid on the membrane. For the fluid damping the membrane is considered as an immersed circular disk. Although this approximation is intuitive to understand the dynamics of the membrane in fluid, it has certain limitations. Viscous forces on a body oscillating in fluid strongly depend on the

geometry of the body and its boundary conditions. An accurate model for the hydrodynamic viscous forces on the membrane should take into account the fluid on top and the air on the backside of the membrane. For accurate dynamic modeling, the frequency dependency of fluid damping should also be considered. When compared to steady flow or low frequency vibration cases, fluid damping behaves drastically different at higher frequencies. The frequency dependent fluid damping for AFM cantilevers has been studied analytically, experimentally and using finite element analysis [58-60].

The fluid flow due to an oscillating body at small amplitude requires the solution of the unsteady simplified Navier-Stokes equations for incompressible fluids [61].

$$\rho \frac{\partial U}{\partial t} = -\nabla P + \mu \nabla^2 U , \qquad \nabla \bullet U = 0 \tag{17}$$

where ρ and μ are the fluid density and viscosity. U and P represent the fluid velocity and pressure, respectively. For the case of oscillating membrane probe, cylindrical coordinates can be used due to the symmetry conditions. When the membrane oscillates at frequency ω, U takes a sinusoidal form at frequency ω with spatial distribution in r- and z-coordinates. Commercial finite element analysis software packages with fluid-structure interaction capabilities can be used to solve these equations for the immersed probes with complex geometries and boundary conditions.

FEM software COMSOL handles this type of problems using Arbitrary Lagrangian-Eulerian (ALE) algorithm. Fluid-structure interaction problems require the solution for the deformation of structures in fluid flow, which in turn affects the flow pattern. COMSOL's ALE method handles the deforming geometries and the moving

boundaries with a moving mesh grid [62]. The result of the software was compared with analytical solution for drag force on an immersed circular disk as a test structure. The computation domain for the problem is given in figure 23. 2D axisymmetric model was created with a 2.5 μm thick solid disk at the center with a diameter of 150 μm.

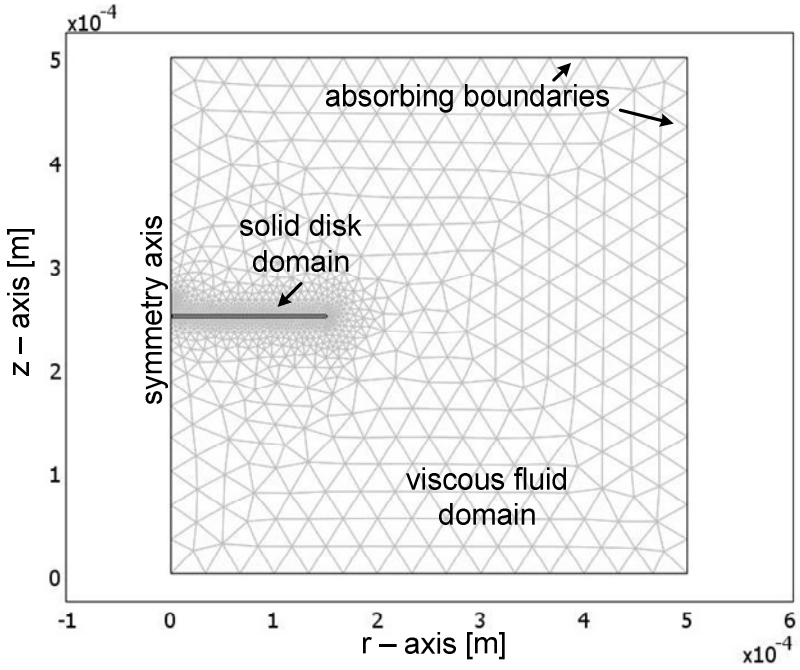

Figure 23. Axisymmetric computational domain for an immersed circular disk.

The drag force, F_z, on an infinitesimally thin disk transversely moving with a velocity of U is given as $F_z = -16\mu aU$. The error for the force prediction is less than %0.5 even when the thickness of the disk is one-tenth of its diameter [63]. A transient simulation was run on COMSOL for drag force computation. The disk was moved with a constant velocity of 1 nm/s in z-direction. The force on the disk as a function of time is shown in figure 24. The force on the disk settled down after t=0.015s and reached a value

of 2.31 fN. The analytical calculation for the same disk and velocity predicts a drag force of 2.4 fN at steady-state, validating the accuracy of the transient COMSOL model.

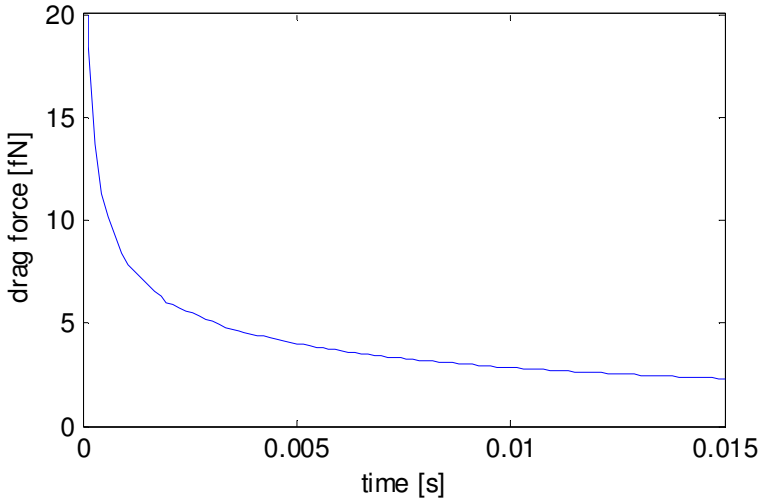

Figure 24. Drag force on the disk (in z-direction) as a function of time.

Transient simulation capability for fluid-structure interactions in COMSOL was used to model frequency dependent fluid damping on membrane probes. Only thin detection membrane was modeled in COMSOL for computational efficiency. The computational domain for a 300 μm diameter membrane is shown in figure 25. Again, axial symmetry was employed for the model.

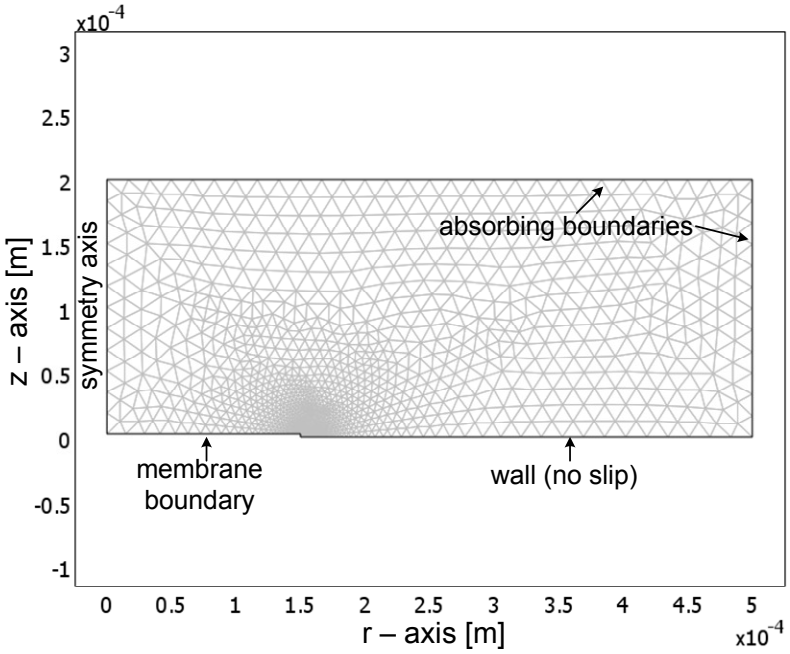

Figure 25. Axisymmetric computational domain for an immersed 300 µm diameter probe membrane.

Simulations were run by oscillating the membrane surface at a specified frequency. The fluid flow generated by the program was used to extract drag force on the membrane. The spatial distribution of membrane velocity over the surface of the membrane was also taken into account by Bessel function of the first kind, $J_0(z)$. Thus, the velocity assigned on the membrane boundary was defined as:

$$V_{membrane}(r,t) = V_{peak} \cdot J_0(2.4048r) \cdot \cos(2\pi f \cdot t) \tag{18}$$

where V_{peak} is the peak velocity of the membrane and was set as 10 µm/s for the simulations. The range for frequency of oscillation, f, was from mHz to kHz. Note that only first mode displacement profile was assumed for the membrane. This is a valid

assumption for a typical operation of the membrane in fluid since data are acquired with a bandwidth of 1 kHz in a typical biological experiment.

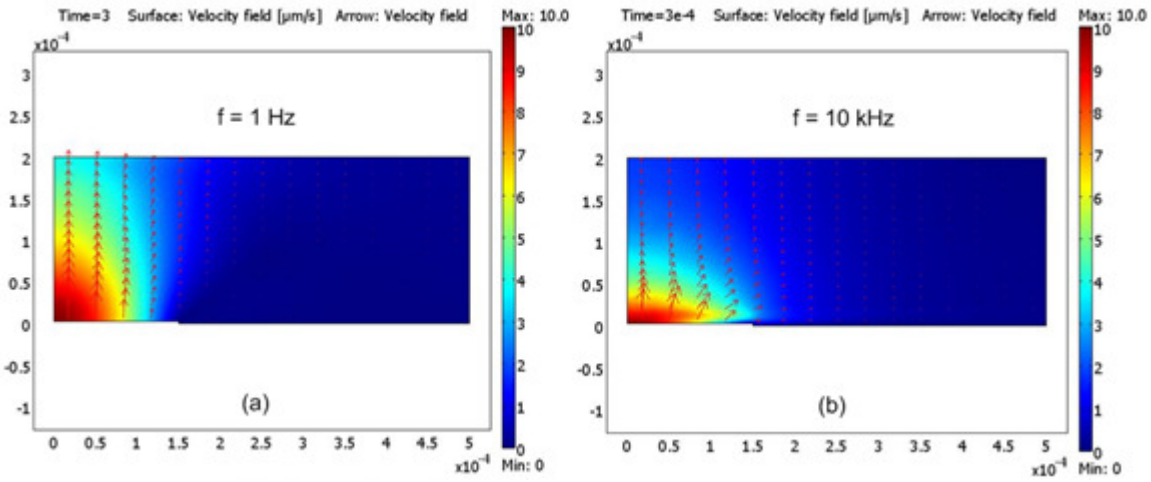

Figure 26. Velocity profile contours in fluid due to membrane oscillation at (a) 1Hz (b) 100 kHz.

Velocity profile contours in fluid generated based on the solution for fluid flow is instructive and shown in figure 26. It was seen that the velocity of the membrane can be effectively transferred to the fluid domain at low frequencies as the profile of the velocity contour in fluid takes the shape of a Bessel function. However, at higher frequencies, the velocity contours appears to be “squeezed” in z-direction. This is due to the increased pressure on the membrane domain.

After the generation of velocity profiles, drag force on the membrane domain was extracted. Figure 27 shows the equivalent drag force at the center of the membrane as a function of time together with the velocity of the center of the membrane. The first observation is that the drag force is in phase with the velocity of the membrane at low frequencies. That means that drag force is solely due to viscous damping. However at

higher frequencies, there is a phase difference between the velocity of the membrane and the drag force on the membrane. That is due to the increased pressure over the membrane surface as previously observed in figure 26.

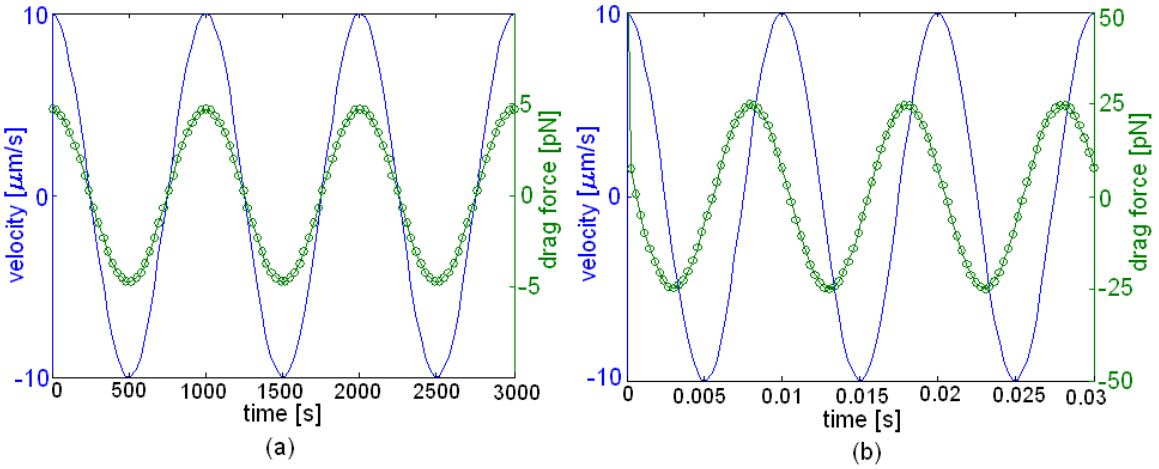

Figure 27. Drag force on the membrane as a function of time plotted together with membrane velocity at (a) 1 mHz, and (b) 100 Hz.

Considering the lumped model, the component of the drag force that is in-phase with the velocity results from the viscous damping coefficient, b. On the other hand, fluid mass affecting the membrane results in the out-of-phase component of the drag force. In the light of these arguments, viscous damping coefficient can be extracted as a function of frequency. The extracted data scales with the multiplication of the radius (r) and square-root of angular frequency (ω). The dependency of damping coefficient on fluid properties is also known. Thus, equation 16 is assumed for the damping coefficient with two constants K_1 and K_2.

$$b = \mu\left(K_1 R_e' + K_2 R_e' r\sqrt{\omega}\right)$$

$$R_e' = \sqrt{\frac{\rho \cdot r^2}{\mu}} \tag{19}$$

where ρ and μ are the fluid density and viscosity, respectively. The constants K_1 and K_2 were determined to be 2.9733×10^{-3} and 2.9733×10^{-1}, respectively using nonlinear least square fitting techniques with the data for 150 µm radius membrane. Figure 28 shows the variation of damping coefficient extracted from COMSOL with respect to frequency together with the model of equation 16. FEM simulations were run for three different values of membrane radius and both the data and model are shown in figure 28. Note that the model was constructed for 150 µm radius membrane for which the coefficient of determination, R^2 is 0.9941. For radii of 50 µm and 25 µm, R^2 values are 0.8216 and 0.8448.

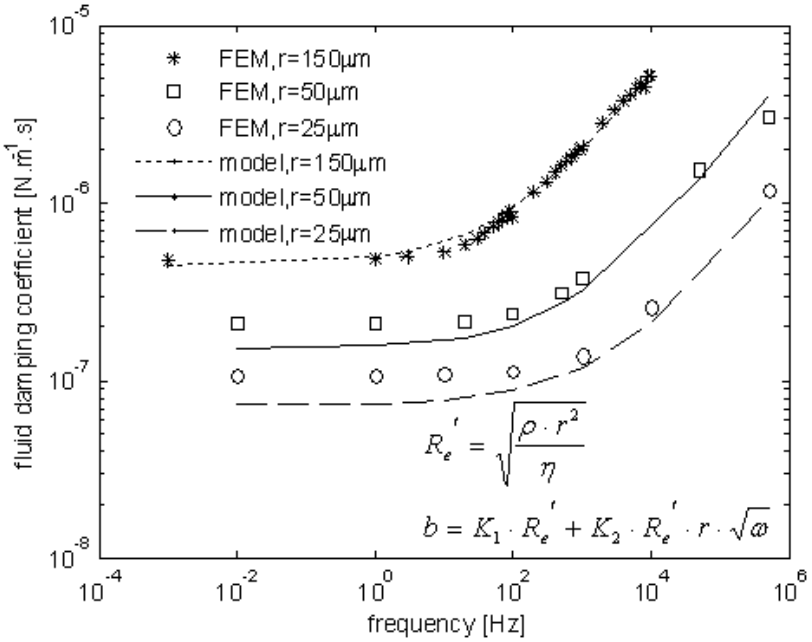

Figure 28. Viscous damping coefficients for different membranes extracted from FEM simulations as a function of frequency.

Thermo-mechanical Noise Calculations

An immediate application of the complete mechanical impedance analysis presented in this section is the calculation of thermo-mechanical noise spectrum for the probe sensors. Figure 29 shows the equivalent circuit of a membrane in fluid including different domains. It is helpful for the calculation of mechanical impedance, $Z(\omega)$, seen by the voltage source. According to fluctuation-dissipation theorem, real part of the mechanical admittance, $Y(\omega)$, (reciprocal of mechanical impedance, $Z(\omega)$) determines the thermo-mechanical noise [64, 65]:

$$X^2(\omega) = \frac{4k_B T}{\omega^2}\mathrm{Re}\big(Y(\omega)\big) \tag{20}$$

where $X(\omega)$ denotes the displacement power spectrum.

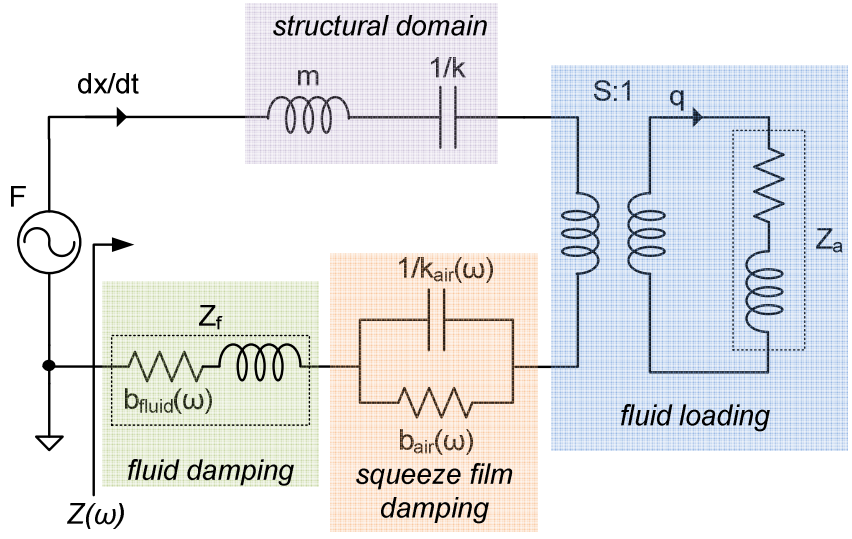

Figure 29. Equivalent circuit of the membrane in fluid used for thermo-mechanical noise calculations.

Accordingly, thermo-mechanical force noise density of the immersed membrane of figure 19 is shown in figure 30(a). Figure 30(b) shows the integrated noise of this membrane. It is possible to detect 1 pN using this membrane with a bandwidth of 1 kHz.

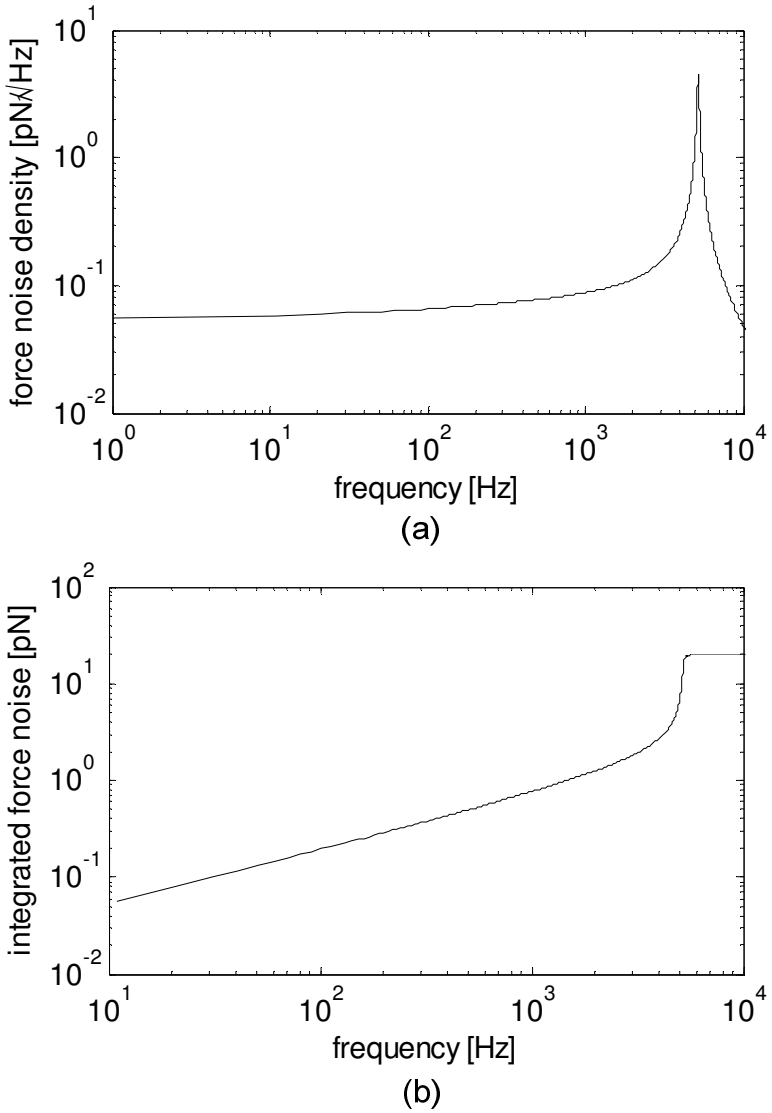

Figure 30. (a) Thermo-mechanical force noise density and (b) integrated noise of the membrane shown in figure 19.

For comparison purposes, performance metrics for detection membranes with different diameters are provided in table 2.

Table 2. Performance metrics

	60 µm radius	100 µm radius	150 µm radius
Spring constant (N/m)	1.1	0.36	0.16
Fundamental resonant frequency (kHz)	5.20	1.73	0.65
Quality factor	40	24	17
Integrated thermo-mechanical noise in 1 kHz bandwidth (pN)	0.77	1.32	8.06

Mechanical impedance analysis together with hydrodynamic modeling presented in this chapter is an important tool for the design of membrane probes. It is possible to predict noise performance and dynamic response of the probes by using this model before fabrication and any experimental characterization. The simulation results obtained using hydrodynamic model compares well with the experimental results and validate the model. The experimental results are presented in chapter 5. This is a significant improvement when compared to basic simple harmonic oscillator (SHO) model commonly used among MEMS community. Basic SHO model requires the knowledge of quality factor which depends on hydrodynamic damping and cannot be calculated without a proper hydrodynamic model.

The design effort for probe sensor is presented in this chapter with an emphasis on high force resolution. Note that the models presented here can also be used to design probes for different applications such as fast imaging. The key components for a fast imaging AFM system are a fast z-scanner and a force sensor with high bandwidth to

resolve transient interaction forces [66]. Stiffer membranes have higher resonant frequency and together with integrated electrostatic actuator, they make ideal z-scanners. Moreover, the quality factor can be adjusted properly by exploiting squeeze-film damping effect as presented in this chapter. These membranes can also be used as high bandwidth force sensors. The higher stiffness poses a drawback as it reduces force sensitivity. However, it is possible to overcome this problem by electronically softening the membrane stiffness using spring softening effect. Thus, a compromise between force sensitivity and bandwidth of already fabricated probes can be made on demand electronically. Details are presented in chapter 7.

CHAPTER 3

FABRICATION OF MEMBRANE PROBES

The microfabrication details and the process flows developed for different types of probes are presented in this chapter. First, silicon nitride/oxide membranes on quartz substrate were fabricated. Silicon nitride and oxide are biocompatible, standard IC materials. Electrically, they also provide dielectric insulation layer in fluid. Fabricating membranes on a transparent substrate makes it possible to optically read the displacement of the membranes from the backside. Relatively thicker (3-5 μm thick) membranes using this process were fabricated as stiff probe actuators.

Silicon nitride/oxide membranes are not good enough for force sensing. As explained in this chapter, large Young's modulus and built-up stress on the layers prevent fabricating softer membranes. Instead, a biocompatible polymer, parylene was used to fabricate probe sensors. Parylene membranes were fabricated on both quartz and silicon substrate. Parylene membranes on silicon exhibit non-uniform structure allowing the optimization of actuator and sensor simultaneously.

Silicon Nitride/Oxide Membrane Probes

The microfabrication of silicon nitride/oxide probes involves a 4-mask process as schematically illustrated in figure 31. Standard IC materials (silicon nitride, silicon oxide, titanium and gold) are used for the mechanical structures whereas a special polymer film (Unity-400) is used as a sacrificial layer.

The fabrication process starts with a 500-550 µm thick quartz wafer on top of which 80 nm thick gold diffraction gratings with a 20 nm thick titanium adhesion layer are formed using e-beam evaporation and a standard lift-off process as shown in figure 31(a). Diffraction gratings are fabricated with periods of 3.3 µm, 4 µm and 6 µm. This step defines the minimum line-width for the fabrication process.

After the definition of diffraction gratings, the Unity-400 sacrificial polymer is spun to obtain a flat 3.2 µm thick layer as shown in figure 31(b). The photo definable Unity-400 layer is patterned by photo-lithography and it can be then thinned down by O_2 plasma in an RIE chamber.

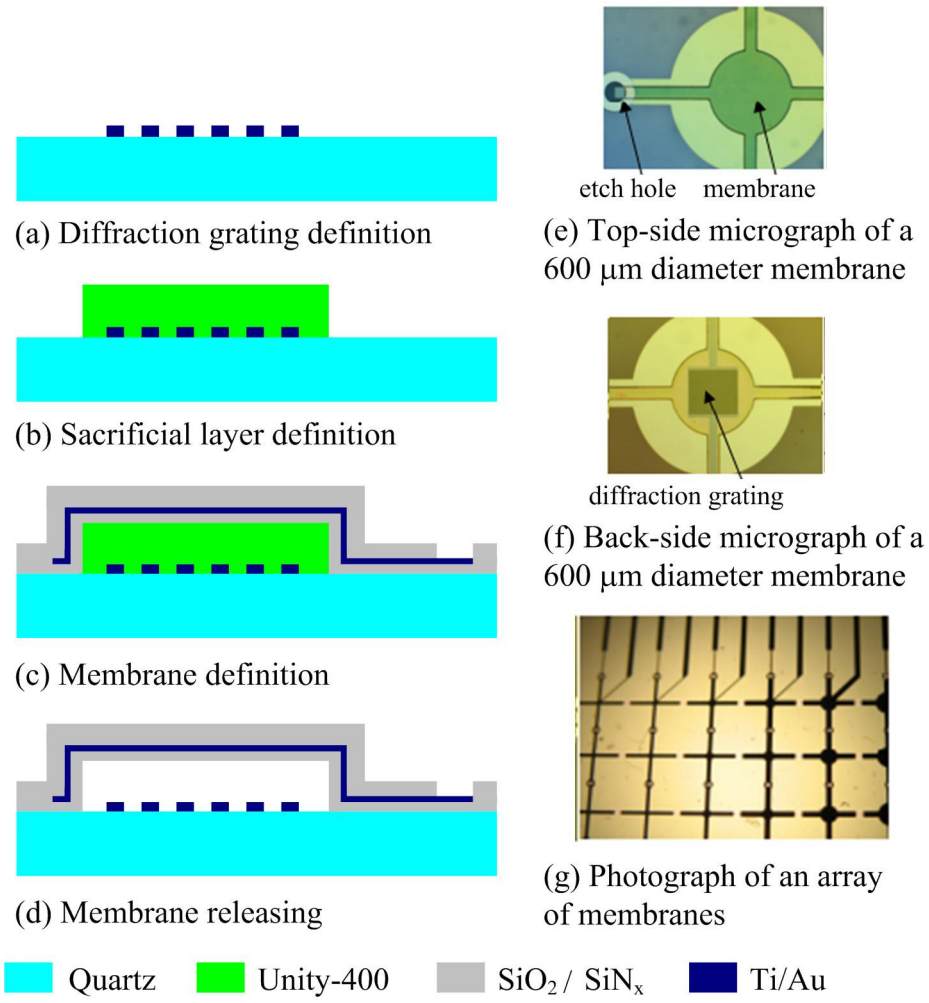

Figure 31. (a-d) Process flow for the fabrication of silicon nitride/oxide membrane probes. (e-g) Photographs of fabricated devices.

To define the probe membrane, first a 0.1 µm thick PECVD dielectric layer to prevent electrical shorting in case the membrane collapses is deposited on top of the sacrificial layer at 300 °C. The dielectric film consists of SiN_x/SiO_2 with a ratio of 0.84:1 to minimize the intrinsic stress built-up in the layer. Then an 80 nm thick gold layer with a 5 nm thick titanium adhesion layer is sputtered and patterned to define the top electrode. Gold layer is etched in KI solution and titanium is etched in 5% HF solution. After metallization another dielectric layer consisting of four sequencing layers of SiN_x

and SiO_2 with a total thickness of 1.5 µm is deposited. The membrane definition step is shown in figure 31(c). The membrane is patterned using RIE etching to open electrical contact pads for electrodes and to form etch holes necessary for the etching of the sacrificial layer.

The Unity-400 film is decomposed by heating up the wafer to a temperature of 440 ºC with a furnace that can supply a continuous flow of N_2 gas at 5-10 sccm. The release step shown in figure 31(d) is carried out slowly in several steps to prevent buckling in the membrane. The decomposition process using furnace is shown in figure 32.

Once the sacrificial layer is fully decomposed, the wafer is then diced into chips and the etch holes are sealed by using epoxy for operation in liquid to finish device fabrication.

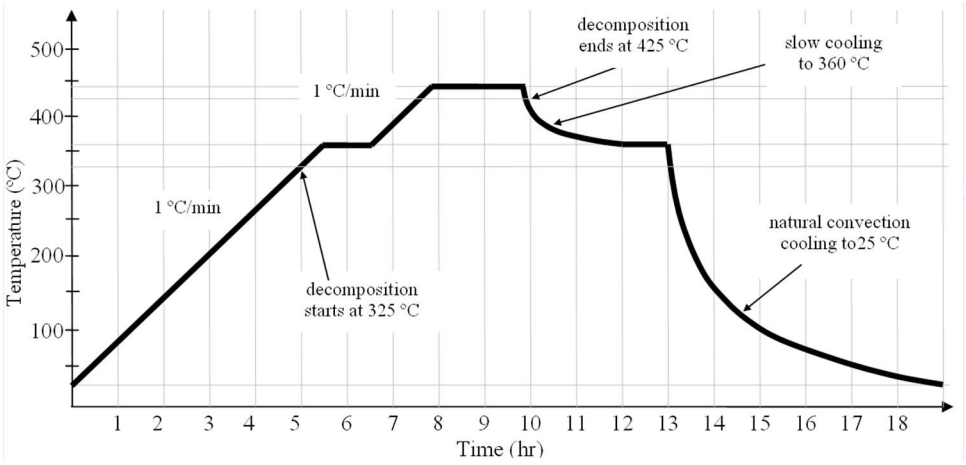

Figure 32. Furnace process for the decomposition of Unity-400 polymer.

Circular probe membranes with various diameters (50-600 µm) were fabricated as shown in figure 31(e-g). Spring constant of each membrane was measured experimentally

by using TriboIndenter (Hysitron Inc.). The experimental characterization results are presented together with lumped model predictions as shown in figure 33. The characteristic equation for a flat circular diaphragm for small displacements is given as follows [67]:

$$\frac{Pa^4}{Eh^4} = \frac{16y}{3(1-v^2)h} + \frac{(7-v)y^3}{3(1-v^2)h^3} + \frac{4a^2\sigma y}{(1-v)Eh^3} \tag{21}$$

where E is the Young's modulus, h is the thickness of the diaphragm, a is the radius of the diaphragm, v is the Poisson's ratio, and σ is the biaxial residual stress. Spring constant of membranes predicted with this model is presented with two different stress values in figure 33.

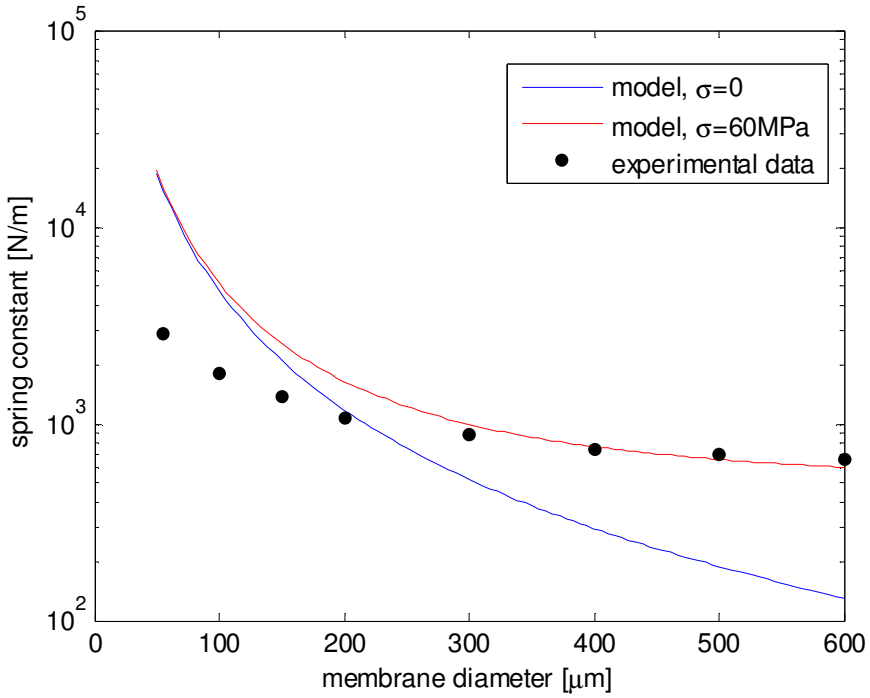

Figure 33. Measurement of spring constant of fabricated silicon nitride/oxide membranes.

The first observation on the spring constant of membranes is that the measured values are considerably smaller than that of the predicted values with the given model for membrane diameter <200 μm. This is due to the fact that the membrane side wall is thinner than the membrane thickness due to the directionality of the deposition process in the PECVD chamber. Thus, a fully clamped support boundary condition assumed by the model does not hold for the fabricated membranes. The second observation is that the model with a residual stress of 60 MPa predicts well the stiffness of membranes with diameters > 300 μm. This indicates that the spring constants of larger membranes are dominated by residual stress. Thus, increasing the diameter of the membranes beyond a certain point is not an effective method to make softer membranes required for force sensing.

Parylene Membrane Probes on Quartz Substrate

Force sensing membranes are designed using parylene as the structural layer. The material selection is based on the material properties and fabrication compatibility of parylene. Young's Modulus of parylene is relatively low: 0.4-2.5 GPa, which makes it a good candidate to make softer membranes [68]. Moreover, a thin layer of parylene usually has relatively low intrinsic stress [69]. In addition to these advantages, parylene films are deposited at room temperature using a chemical vapor deposition (CVD) process and can be patterned at room temperature using O_2 plasma.

Previously outlined process flow is adapted for parylene membrane fabrication as shown in figure 34. The structural membrane material is replaced by parylene and the new process uses the same mask set. The fabrication process is now carried out in room temperature. Thus, photoresist can be used as a sacrificial layer instead of Unity-400 to make the process simpler (figure 34(b)). The membrane layer is now composed of 0.5 µm thick parylene at the bottom, 0.2 µm thick gold in between, and 1.5 µm thick parylene on top. A thin layer of chromium (~5 nm) is used to improve adhesion between parylene and quartz and parylene and gold. Parylene layer is patterned in RIE chamber with O_2 plasma using a metal hard mask.

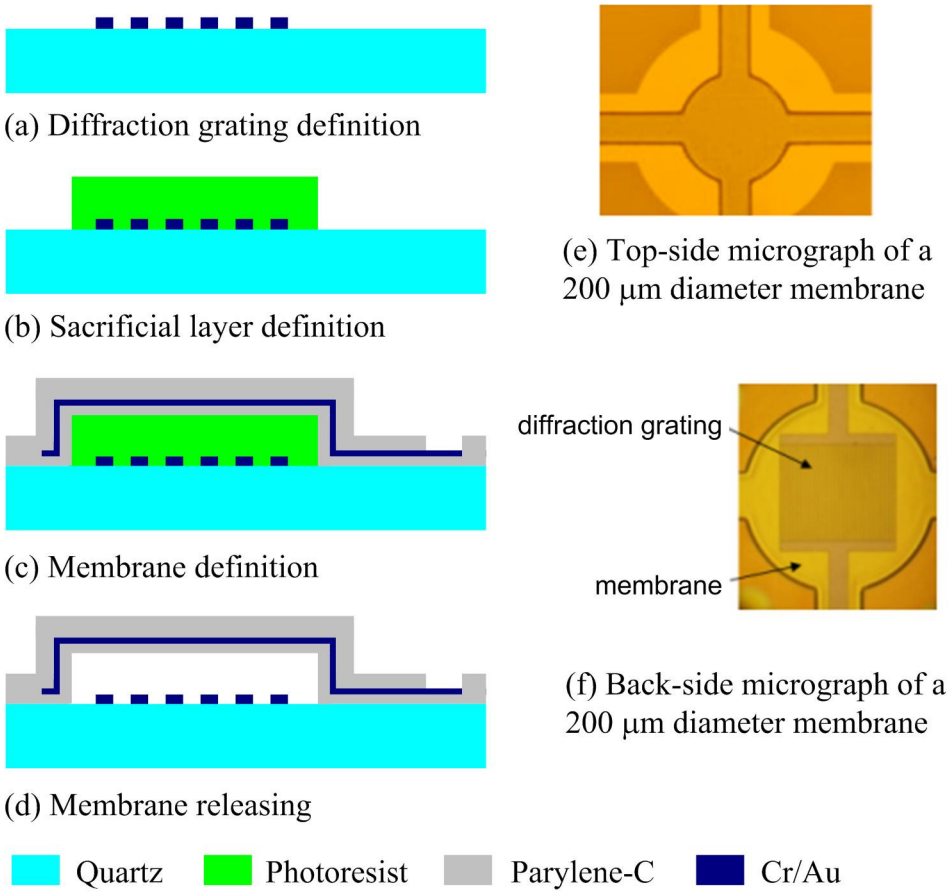

Figure 34. (a-d) Process flow for the fabrication of parylene membrane probes on quartz substrate. (e,f) Photographs of fabricated devices.

Finally the membranes are released in acetone and by using super critical dryer to prevent stiction. Fabricated devices are shown in figure 34(e,f). Using parylene makes the fabrication of membranes easier without sacrificing the quality. It is possible to fabricate relatively flat membranes as shown in figure 35. The profile of a 600 μm diameter membrane is obtained using an optical profilometer (Wyko Profilometer, Veeco Instruments). The membrane surface is sufficiently smooth for biomolecular force spectroscopy experiments.

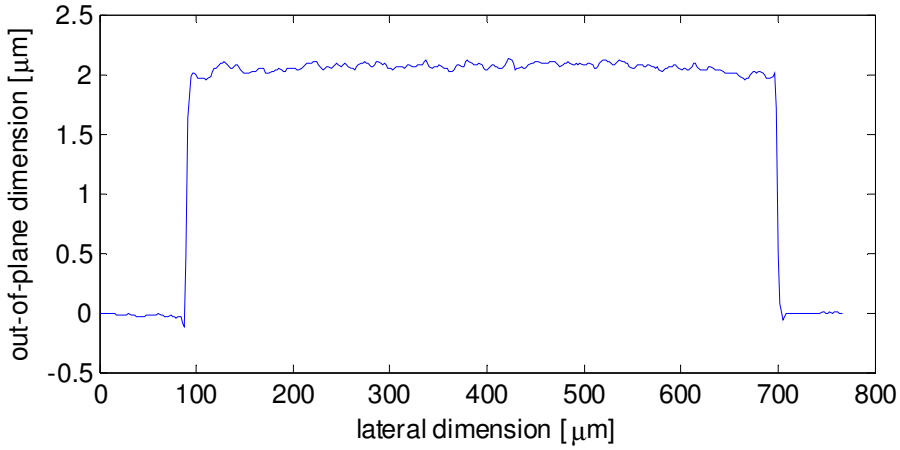

Figure 35. Profile of a 600 μm diameter parylene membrane obtained using a white light interferometer.

The spring constant of the fabricated membranes are measured using AFM with a calibrated AFM cantilever. Several force curves are obtained at the center of each membrane and the spring constant of each membrane is calculated using the slope of force curves and the spring constant of the cantilever. The measured values are compared with the ones predicted by the model of equation 21 as shown in figure 36. The first observation is that parylene membranes are softer than the silicon nitride/oxide ones. It is possible to fabricate one or two orders of magnitude softer membranes with parylene depending on the membrane diameter. Again, the smaller diameter membranes are softer than what the model predicts due to the fully clamped boundary condition assumed by the model. Also, the spring constants of larger membranes are dominated by residual stress, which is calculated to be 0.5-1.5MPa.

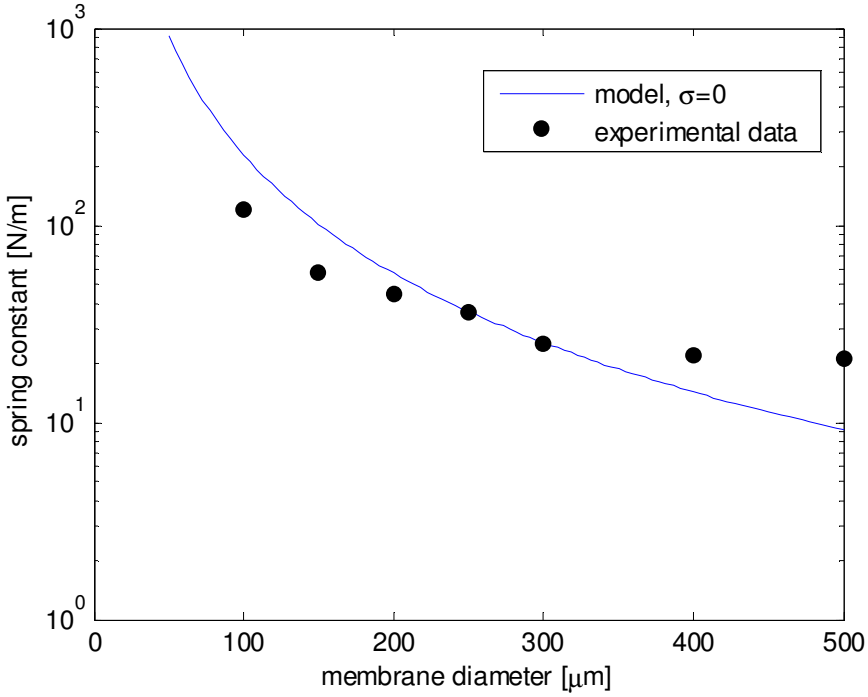

Figure 36. Measurement of spring constant of fabricated parylene membranes.

Parylene membranes with spring constants of ~20 N/m are fabricated with this process. These membranes can be used as force sensors for biomolecular force spectroscopy experiments to measure pN-level forces. However it is still desirable to reduce the spring constant of membranes to values with single digits to measure single digit pN-level forces and even sub-pN-level force. Obviously thinner membranes would reduce the spring constants but the membranes can not be thinned down beyond a certain point. Because, parylene layer seals the top electrode and thinner membranes are vulnerable to electrolysis during operation in fluid. One way to reduce the spring constant of the membranes is to use spring softening phenomenon as described in Chapter 7. Yet, another approach is to decouple the detection membrane from the actuator membrane with a non-uniform membrane design as described in Chapter 2.

Non-uniform Parylene Membrane Probes on Silicon

The fabrication of non-uniform membranes is a Si-based, 7-mask process as schematically illustrated in figure 37. The fabrication process starts with a ~300 μm thick Si wafer on both sides of which 3 μm thick PECVD nitride films are deposited. The back-side nitride film is used as masking layer for etching silicon substrate using potassium hydroxide (KOH) in a subsequent step. The front-side nitride film electrically isolates the electrodes from each other and the substrate. On top of this nitride layer, 100 nm thickness gold bottom electrodes of the electrostatic actuators integrated to the membrane probes (with 10 nm thickness chromium as an adhesion layer) are patterned using filament evaporator and a standard lift-off process with the first mask as shown in figure 37(a). After the definition of the bottom electrodes, the back-side nitride layer is patterned in a reactive ion etch (RIE) chamber to open KOH etching windows with the second mask. Back-side alignment is required for this lithography step to align the windows to the electrodes on the front-side of the wafer. The front-side nitride layer is then thinned down to a thickness of 1 μm after which a 2.5 μm thick positive photoresist (SC1827, Shipley) is spun and patterned as the sacrificial layer as shown in figure 37(b). The membrane structure is made of parylene with buried electrodes in it, and the membrane formation starts with a 0.5 μm thick CVD parylene layer deposition as an insulation layer between the electrodes to avoid electrical shorting for the actuator section. This parylene layer also formes the structural layer for the detection membrane. The parylene layer is patterned using RIE etching. The structures are protected with a

titanium hard mask for RIE etching since the etch rate of parylene and photoresist are on the same order. Then a 150 nm thick aluminum layer is sputtered as the top electrodes. In order to promote adhesion between the aluminum and parylene layers, 10 nm thick chromium layers are sputtered on the top and bottom side of the aluminum layer. The metal layers are wet-etched for patterning as shown in figure 37(c). Finally another 1 μm thick parylene layer is deposited over top electrodes for protection in fluid. This parylene layer also serves as the anchor surface for biomolecules. Top parylene layer is patterned similarly using a titanium hard mask as shown in figure 37(d). The fabrication of front-side of the wafer ends after this step and KOH etching is used to open backside venting holes that also serve as etch holes for the membranes as shown in figure 37(e). KOH bath is held below 70°C to prevent cracking on parylene layers due to thermal stress. All hard-baking and soft-baking steps after the deposition of first parylene layer are also carried out below 90°C, otherwise cracking on membrane layers is observed. Anisotropic etching of silicon substrate with KOH stops at front-side nitride layer, which is then RIE etched from back-side of the wafer. Finally the wafers are diced into chips for releasing the membranes and the chips are treated with acetone to etch out the photoresist sacrificial layer. The samples are dried using a super critical dryer to prevent stiction after the photoresist layer is removed.

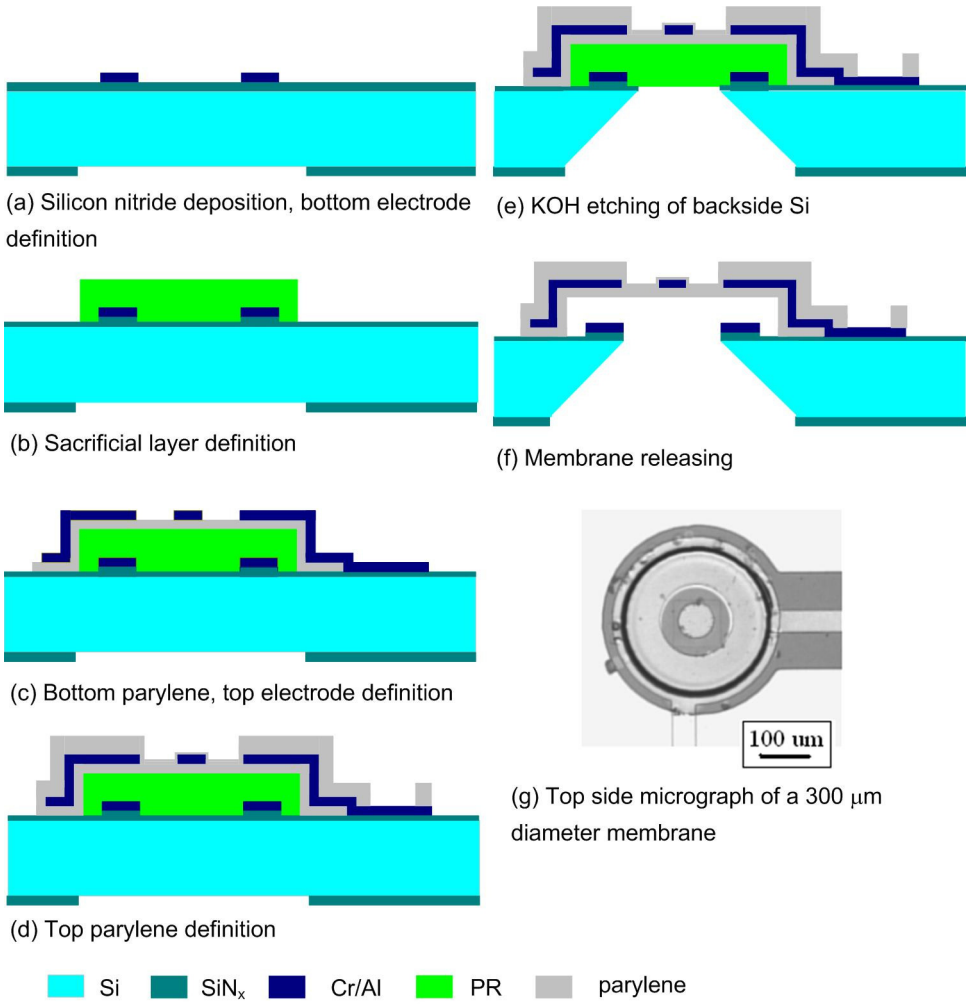

Figure 37. (a-f) Process flow for the fabrication of silicon based parylene membrane probes. (g) Photograph of a fabricated device.

Non-uniform membranes with different geometries were fabricated. Table 3 summarizes the variation of these membranes. The table is sorted from larger membranes to smaller ones. Larger membranes tend to be softer and the area reserved for their electrodes are larger. Therefore, these membranes require lower voltages for actuation. The smaller membranes are designed mainly as force sensors as they have lower viscous damping in fluid. They also have broader dynamic response for fast-pulling experiments at the expense of increased voltage requirement.

Table 3. Design variation for the fabricated non-uniform membranes

a: outer diameter b: outer diameter for the thinned down section c: diameter of the reflection pad d: length of the backside hole	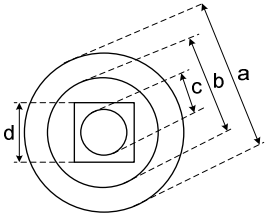 Top view of the membrane		
a [µm]	b [µm]	c [µm]	d [µm]
600	240	100	300
500	300	100	300
400	300	100	300
400	200	80	200
350	240	100	240
350	200	80	150
350	120	60	120
300	150	80	150
300	120	60	120
200	120	60	150
200	120	40	100

After the fabrication of the probes, it is absolutely mandatory that the membrane surface would anchor the biomolecules without compromising on the molecular functionality during membrane functionalization in biomolecular experiments. The

surface of the membrane is parylene, which is hydrophobic in nature. Hydrophobic surfaces would be good for protein adsorption while a hydrophilic surface would be good for experiments involving molecules reconstituted in supported lipid bilayers. It has been shown that the hydrophobicity of parylene surfaces can be altered by treating them with oxygen plasma in an RIE chamber [70]. Hence, the surface chemistry of a hydrophobic parylene surface can be accordingly altered to suit experimental needs.

CHAPTER 4

OPTICAL DETECTION

This chapter focuses on the design and implementation of optical detection system to measure membrane displacement. The system includes optics, associated electronics and a mechanical setup. This setup allows the membrane operation coupled with a commercial AFM head (Bioscope, Veeco Metrology – Digital Instruments, Santa Barbara, CA) in air and fluid.

Experimental Setup

Figure 38(a) shows the photograph of the setup where the key components are labeled. Mechanically it was designed such that it houses the commercial AFM head and the stepper motor attach to the head on top. The parts where the AFM head is attached to the setup were made of the same alloy to minimize thermal deformation due to differences in coefficients of thermal expansion (CTE). The rest of the setup was made of an aluminum alloy that has a small CTE value. The mechanical parts consist of housing elements to mount membrane probes, optics and electronics. Special holders for different variations of membranes and membrane arrays were machined to fix the membranes in use. Angular positioning of optics is fixed by using guided mounts. Micromanipulators seen in figure 38(a) allow relative positioning of both the membranes with respect to the

readout optics and the membranes with respect to the AFM cantilevers. A camera is attached to the side of the setup to monitor the locations of the cantilever and the membrane. Imaging optics consists of a 0.28 NA, long working distance (33.5 mm) objective (378 Series, Mitutoyo, Kanagawa, Japan).

Optical design and associated electronics are detailed in the following sub-chapters.

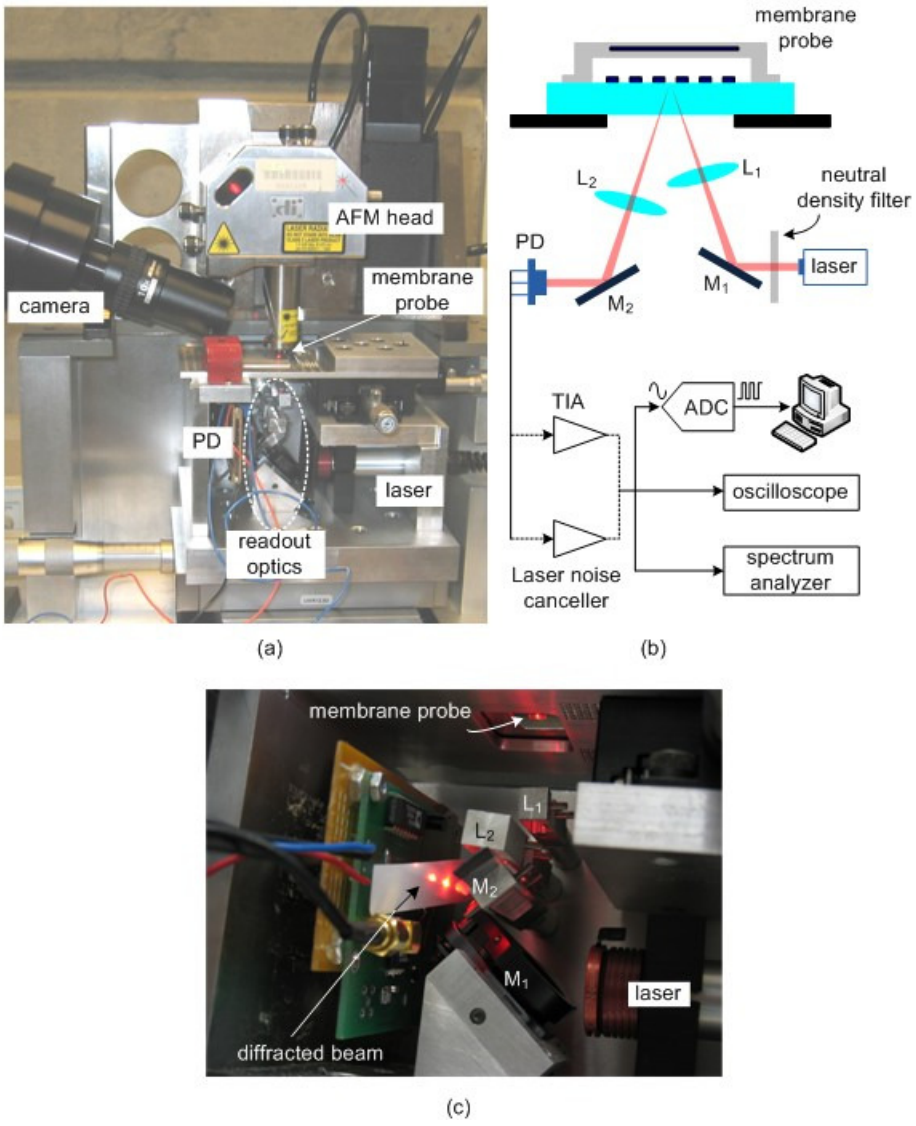

Figure 38 (a) Photograph of the setup showing key components. (b) Schematic of the optics and electronics for membrane readout. (c) Photograph of readout optics when the membrane is in use. The laser path is traced with red for clarification.

Optical Design

Displacement of the membranes is read out using diffraction grating based Michelson type interferometer originally developed for capacitive acoustic transducers [71]. This technique provides interferometric displacement detection sensitivity in a relatively small volume without the need for fine alignment. Figure 38(b) shows the schematic of the optical elements use for the readout setup. The low noise laser (RMS noise <0.06% in 10Hz-100MHz) module supplies 5 mW laser light at 635 nm (ULN series, Coherent Inc., Santa Clara, CA). The incident beam passes through a neutral density filter used to adjust laser power incident on the membranes. The beam is then deflected by an adjustable reflective mirror (M_1) and focused on the membrane grating with a focusing lens (L_1). The light intensities in the 0^{th}, $+1^{st}$ and -1^{st} diffraction orders are captured and collimated by a cylindrical lens (L_2) before they are directed onto photodiodes (PD) after reflection from a second mirror (M_2). The photocurrents from the PD's are converted into readout signals by either transimpedance amplifiers (TIA) or a laser noise canceller circuit with a gain of 5 kV/A. The details of the electronic circuits are given in the next sub-chapter. The readout signal after the electronic circuit is fed into an oscilloscope (Tektronix, TDS2004) from which DC and modulated DC signals are monitored. The readout signal is also fed to a data acquisition card (PCI-6115S, National Instruments, Austin, TX) that is used to acquire the signal into a computer and a dynamic signal analyzer (Stanford Research Systems, SR780, Sunnyvale, CA) that is used for noise characterization.

Ray tracing in the optical train to steer the laser beam from the laser to the membrane and from membrane to the photodetectors is shown in figure 39. Optical design software OSLO (Educational version, 6.4.5, Lambda Research, Littleton, MA) was used for ray tracing. In this design a diffraction grating with a period of 4 µm was placed on the membrane plane. The focal length of L_1 was selected such that the beam diameter on the diffraction grating plane is approximately 30 µm. OSLO was used to determine the positioning of this lens.

The purpose of the lens, L_2, is to collect light intensities only in the 0^{th}, $+1^{st}$ and -1^{st} diffraction orders and collimate them. Thus, a cylindrical lens with a focal length of 38.1 mm was selected to generate the desired waveform. Figure 39 shows a slight deviation from ideal case, i.e. diffraction orders in parallel, due to the finite lens thickness. Nonetheless, reasonable order separation was achieved with the selected lenses.

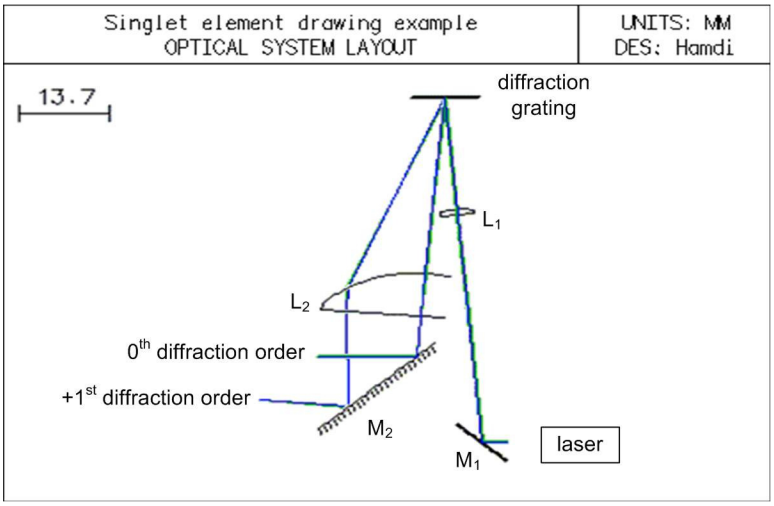

Figure 39. Ray tracing generated by OSLO software.

OSLO is a powerful design tool for ray tracing purposes for ray optics. In addition to this, it also has a useful Gaussian beam propagation algorithm that can handle various optical elements. Figure 40 shows the laser beam propagated in the optical train. Given that L_2 is cylindrical, both X and Y azimuths are provided. Both figures are plotted for 0^{th} diffraction order after the diffraction grating.

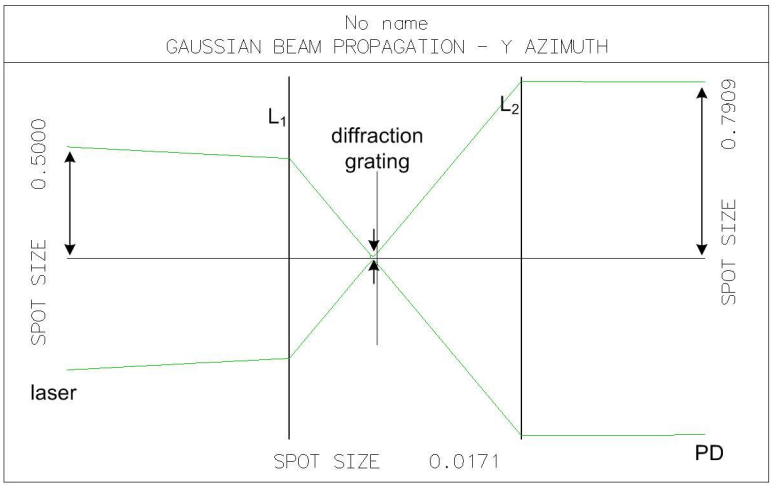

(a)

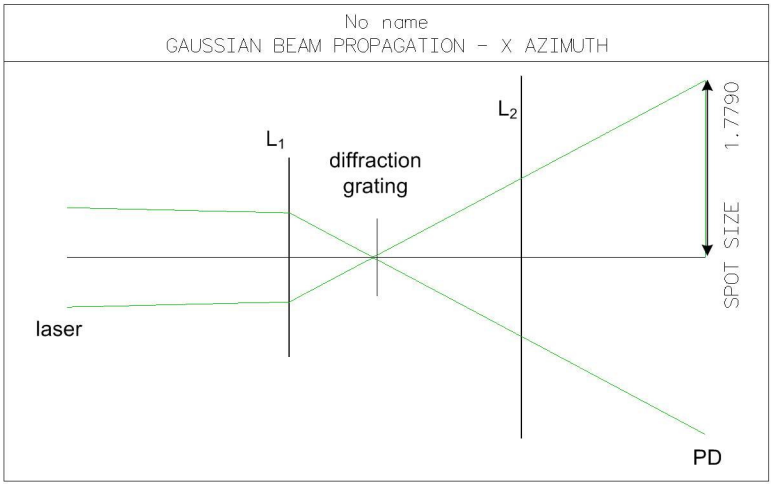

(b)

Figure 40. Determination of spot size along (a) Y-Azimuth (b) X azimuth generated by OSLO software using Gaussian optics.

The laser generates a circular beam with a beam diameter of 1 mm and beam divergence of <1 mrad as shown in the model given in figure 40. The focusing lens L_1 focuses the lens to a beam diameter of ~34 μm onto the membrane probe. This is consistent with the first order calculation of 30 μm beam diameter. After the beam is reflected off of the diffraction grating and passed through lens L_2, it is collimated along Y-azimuth with a beam diameter of ~1.6 mm as shown in figure 40(a). Along X-azimuth, L_2 essentially has no effect and the beam propagates towards the photodetectors. The beam diameter at the photodetector plane is ~3.6 mm.

Based on the optical design two sets of photodetectors have been used to capture the beam. One set consists of a 46-element photodiode array with an active area of 45.9 mm by 4.4 mm (S4114-46Q, Hamamatsu Photonics K.K., Japan) and associated transimpedance (TIA) amplifiers. The other set consists of three discreet Si photodiodes with active areas of 3.6 mm x 3.6 mm (FDS100, Thorlabs, Newton, NJ) and the laser noise canceller circuit built for low noise detection. The details of these circuits can be found in the following section.

Design of Photodiode Array Readout

The photodiode array readout circuit was built to convert individual photodiode currents generated by the diffraction order beams into voltage. The circuit also has an additional differential output that subtracts +1st order photocurrent from the 0^{th} order after their mean values are equalized. Thus the circuit has a total of four outputs, three for

the diffraction orders, and one for the differential. The circuit schematic in figure 41 only shows 1st and 0th order inputs, omitting the -1st order for simplicity.

The gain of the transimpedance amplifier is set by the feedback resistor, R_F. Here R_F is determined based on the optical power incident on the photodiodes. The laser power is 5 mW and assuming 10% loss through the optical train, 0th order photocurrent will be 1.94 mA when the gap height equals to an integer multiplier of half of the laser wavelength (λ). Given the optical loss, this is the largest possible input current to the TIA. For R_F=5 kΩ, the output of the 0th order TIA becomes 9.68 V. This figure is reasonably good as the maximum operating voltage for an OPAMP biased at +/-12 V.

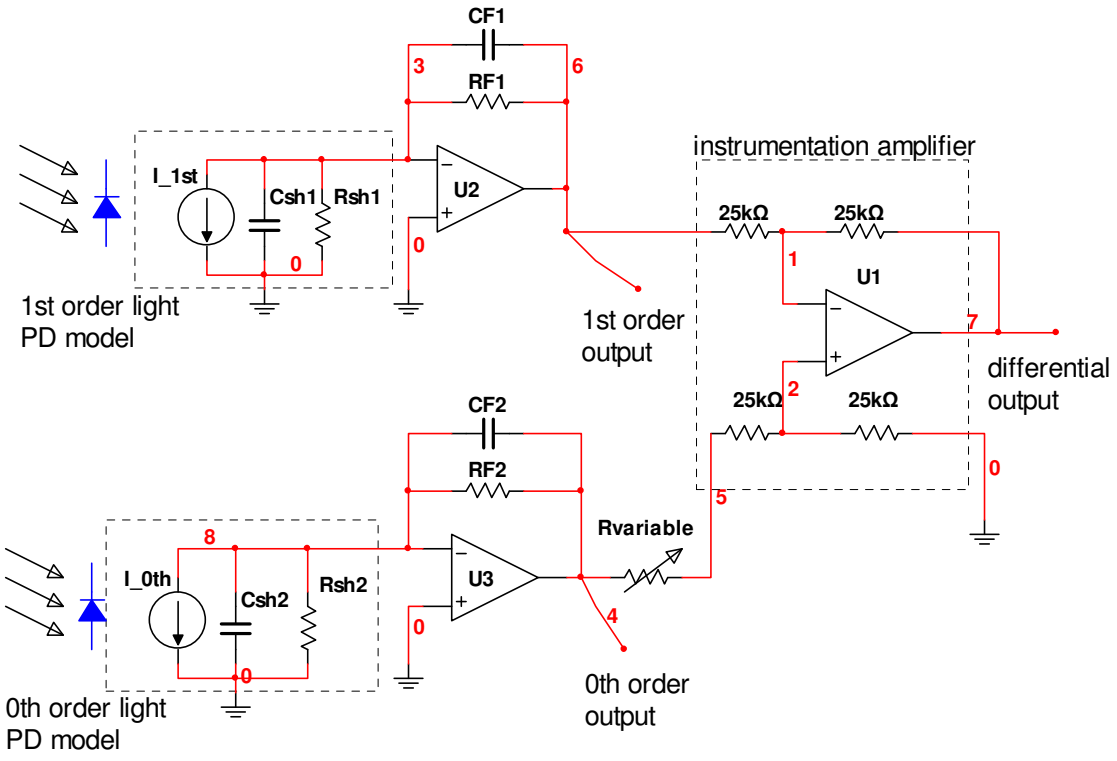

Figure 41. Schematic of circuit for PD array readout.

The photodiode model shown in figure 41 consists of a shunt resistor (R_{sh}) and a shunt capacitor (C_{sh}). The values of shunt elements for the selected Hamamatsu photodiode array are 15 MΩ and 350 pF. C_{sh} on the inverting terminal of the OPAMP can be detrimental for the stability of the amplifier as it creates a zero (f_z) on the noise gain (NG) of the TIA. Noise gain is defined as the gain of the amplifier to bias current induced voltage. Hence, NG and f_z are given as follows [72]:

$$NG = \frac{1 + sR_F(C_{sh} + C_F)}{1 + sC_F R_F} \tag{22}$$

$$f_z = \frac{1}{2\pi R_F C_{sh}} \tag{23}$$

The sole purpose of the feedback capacitor (C_F) is then to place a pole to cancel out the effect of the zero defined by C_{sh}. C_F, indeed, reduces the bandwidth of the TIA but it is required to prevent the circuit to oscillate. The value of C_F to obtain a phase margin of 45° and the resultant bandwidth of the TIA depend on the gain-bandwidth product of the OPAMP (GBW) and are given in equation 24 and 25.

$$C_F = \sqrt{\frac{C_{sh}}{2\pi R_F (GBW)}} \tag{24}$$

$$f_{-3dB} = \sqrt{\frac{GBW}{2\pi C_{sh} R_F}} \tag{25}$$

The design requirement for the TIA is to minimize noise and offset voltage at the output and to provide a flat response with a bandwidth of 1 MHz. Note that the fast membranes can be actuated with 1 MHz bandwidth and the readout electronics should be compatible with this figure. To meet these requirements the OPAMP OP627 from Texas Instruments was selected. The selection was based on the fact that OP627 has a good comprise of noise, precision and speed. It is very quiet (4.5 nV/√Hz at 10 kHz) and it has low voltage offset (<100 μV) at its output. The *GBW* is 16 MHz, which makes it suitable for the bandwidth requirement of the TIA. With this *GBW* the required C_F is calculated to be 27 pF that brings the TIA bandwidth to 1.1 MHz.

Voltage noise spectral density at the output of the TIA depends on the voltage gain of the circuit and given as [73]:

$$e_o = e_n \frac{A}{1 + A\beta} = e_n \frac{1}{\beta} \frac{1}{1 + \frac{1}{A\beta}} \tag{26}$$

where e_n represents the OPAMP's voltage noise spectral density, $A(\omega)$ represents the open-loop gain and $\beta(\omega)$ represents the feedback factor. For the circuit shown in figure 41, the feedback factor equals to [73]:

$$\frac{1}{\beta} = \left[\frac{R_1 R_2}{R_1 + R_2} \right] (C_1 + C_2) \tag{27}$$

Summarizing these results, the noise response for a generic TIA is shown in figure 42. The voltage noise of the amplifier shown here is referred to its input and the

output noise spectrum density can be calculated by multiplication of closed loop noise gain and the voltage noise of the amplifier.

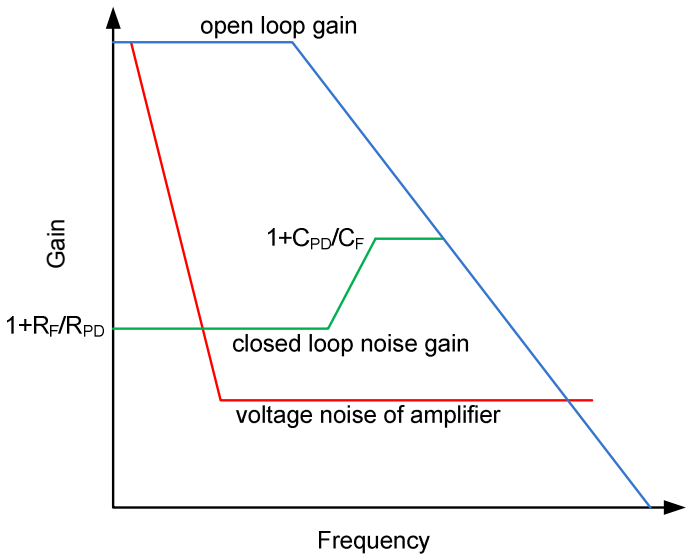

Figure 42. Bode plot of noise response showing different regions associated with a typical transimpedance amplifier. (Adapted from Burr-Brown, "Noise Analysis of FET Transimpedance Amplifiers," *Application Bulletin,* vol. SBOA060, 1994.)

Design of a low noise photodiode readout circuit requires control of individual noise sources. The basic noise sources can be denoted as the amplifier noise, the shot noise in the photodiodes, laser intensity noise, and the thermal noise associated with the feedback impedance of the TIA. Laser intensity noise is directly proportional to the DC value of the generated photocurrent and the relative intensity noise (RIN). Relative intensity noise originates in the laser cavity and is independent of the power incident on the photodiodes [74]. Since increasing laser power increases the DC value of the photocurrent, laser intensity noise can easily dominate the overall noise. On the other hand, it is better not to allow any of the individual noise sources to dominate the total

noise spectrum for better sensitivity. Fortunately, RIN in multiple beams originating from one laser source is correlated. Any correlated noise in two different signals can be eliminated if DC values of the signals are cancelled by subtracting or dividing the signals. Based on this fact, a differential output is added to the circuit shown in figure 41. A differential amplifier (INA134) was selected from Texas Instruments to subtract 90˚ out-of-phase orders to cancel the RIN. The selection was based on the features of the IC including high common-mode rejection (CMRR=90 dB), wide output voltage swing (+/-16V) and low distortion (0.0005% at 1 kHz). Leveling the DC values of the signals is done using the variable resistor, R_{var} and the output signal is given as:

$$V_{out}^{d} = \frac{50k\Omega}{50k\Omega + R_{\text{var}}} V_{out}^{0} - V_{out}^{1} \tag{28}$$

Given the parameters of the design circuit and estimation of photocurrents, noise performance of the photodiode array circuit can be determined. Assuming an optical loss of 10% through the optical train and a gap height of 0.125λ the 0^{th} order photocurrent will be 968 μA. This value is about half of the maximum photocurrent used to determine the feedback resistor. The 1^{st} order photocurrent with these assumptions is 784 μA. Then, the corresponding shot noise densities ($\langle i_{shot} \rangle = \sqrt{2qI_{DC}}$ $(A/\sqrt{Hz})$, q is the electron charge) in the photodiodes are 17.6 pA/√Hz for 0^{th} order and 11.2 pA/√Hz for the 1^{st} order.

The noise densities at the outputs of the detection circuit are summarized in figure 43. RIN noise is not shown in this figure since ideally it will be cancelled out at the

differential output. The noise densities show that the electronics noise is below the shot noise limit, but the shot noise limit does not significantly dominate the overall noise as desired.

Assuming 100% modulation in the diffraction orders, the sensitivity values will be 163 $\overset{o}{A}/V$ for the 0th order and 403 $\overset{o}{A}/V$ for the 1st order. Using the noise densities and the sensitivity values, one can determine the minimum detectable displacement (*MDD*) possible with the sensor, which is shown in figure 43(d). Note that it is possible to detect the displacement of the membrane with 3×10^{-4} $\overset{o}{A}/\sqrt{Hz}$ noise floor.

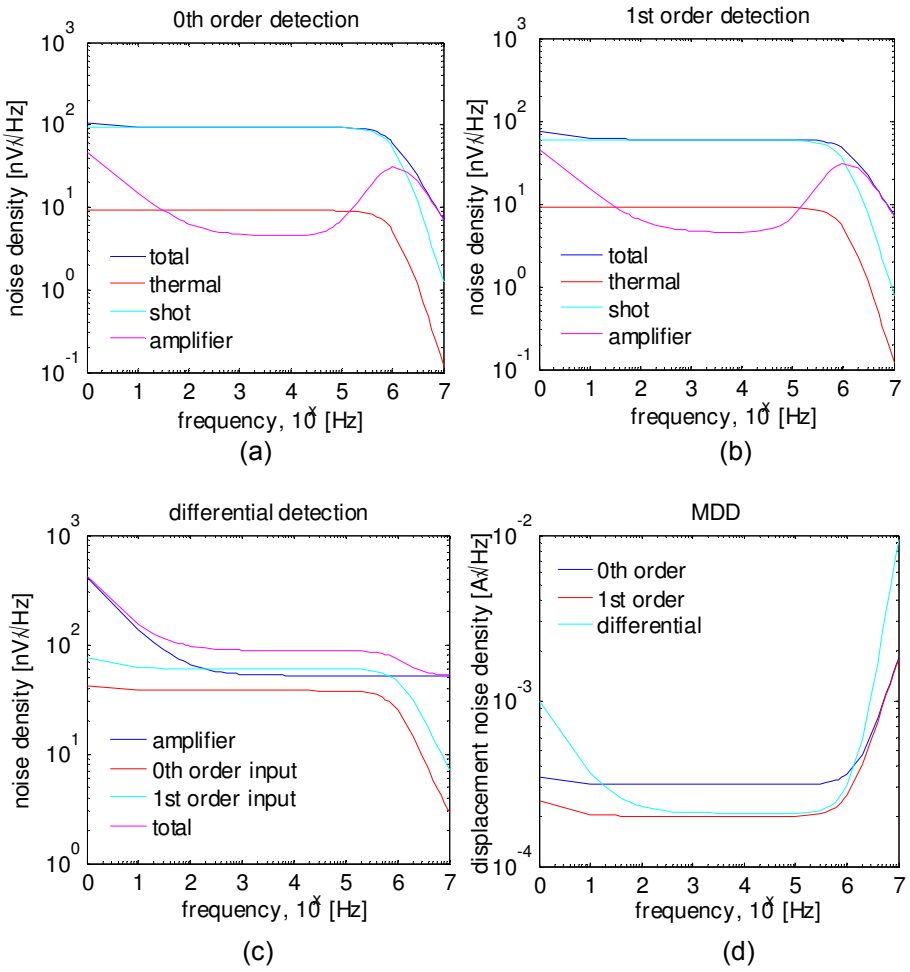

Figure 43. Calculated voltage noise density at the output of (a) 0th order TIA (b) 1st order TIA (c) Differential amplifier. (d) Calculated displacement noise density using different electrical outputs.

Experimental verification of the noise modeling for the photodiode array detection circuit was done using a stiff silicon nitride/oxide membrane. Stiff membrane (spring constant ~1000 N/m) guarantees that the thermal noise of the membrane is negligible comparing to the shot noise in the photodiodes and the electronics noise. The noise spectrum converted into displacement noise density is shown in figure 44. The photocurrents were adjusted such that they were almost identical to the values used for

modeling. The excess noise in 0^{th} order and 1^{st} order can be attributed to the RIN noise and it is clearly shown that the RIN is effectively suppressed at the differential output. The experimental noise floor, $4\times10^{-4}\ \mathring{A}/\sqrt{Hz}$, is in good agreement with modeling, thus verifying the noise model.

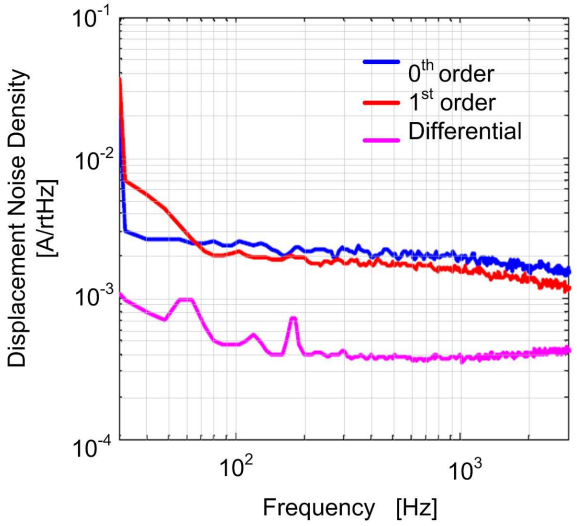

Figure 44. Measured displacement noise density with PD array electronics.

Laser Noise Canceller Circuit

Cancelling laser noise has been an interesting problem to increase the performance of electro-optical systems. Several different approaches, both optical and electrical, have been used to achieve the task [75-77]. Cancellation in electrical domain is appealing for its versatility and flexibility. The obvious way is to use a differential detection method to cancel out the DC value of two signals as shown in previous sub-chapter. Specifically for diffraction grating based sensor, the DC values of both orders

need to be kept the same at all times for perfect cancellation. This is not possible for practical reasons such as drift in membrane position or in electrical signals. It is also possible to cancel out the laser noise by simply dividing the signals. This method sounds simpler as it does not require leveling the DC values of the signals. However, implementation of voltage dividers required for this task is not easy. The commercially available dividers are slow and noisy. It is typical for a divider to have several $\mu V/\sqrt{Hz}$ voltage noise spectral density.

P. C. D. Hobbs attacked laser noise cancellation problem elegantly and designed a relatively simple balanced circuit [76]. This circuit automatically equalizes the DC value of two different photocurrents after they are converted into voltage. The output of the circuit is the difference of the signals, thus free from laser noise. Based on the original design, the circuit shown in figure 45 is designed to meet the requirements for membrane probe readout.

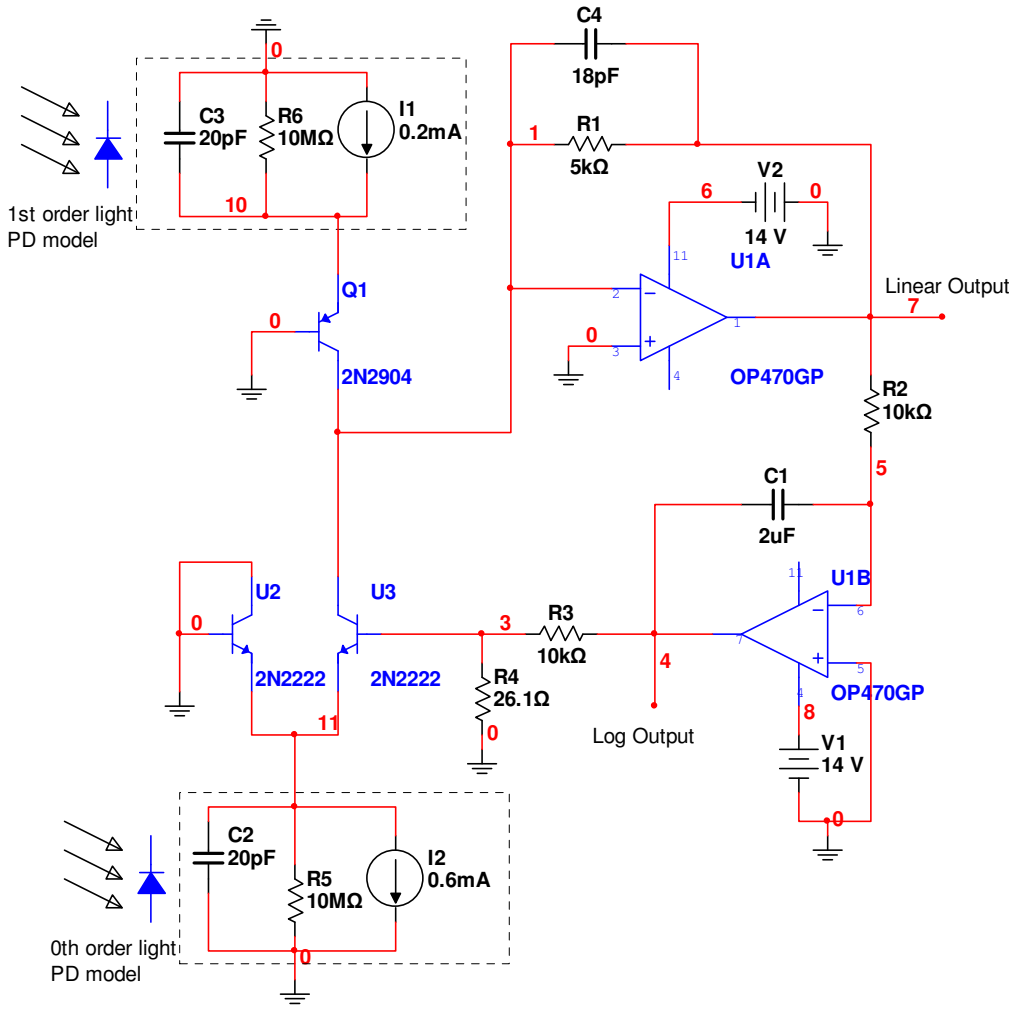

Figure 45. Schematics of laser noise canceller circuit for low noise displacement detection. (Reproduced from P. C. D. Hobbs, "Ultrasensitive laser measurements without tears," *Appl. Opt.,* vol. 36, pp. 903-920, 1997.)

The input current to the transimpedance amplifier, *U1A*, is the difference of collector currents of *Q1* and *U3*. This difference current is forced to be zero by the servo amplifier *U1B* in the feedback loop so that the DC output of *U1A* is zero. 0^{th} order photocurrent is used as the comparator for the 1^{st} order photocurrent used as the signal. The voltage difference in the base-emitter voltages of *U2* and *U3* controls the ratio of

collector currents of the transistors, thus determines the cut-off frequency of low pass filter inherent to the design [76].

$$f_c = \frac{q}{2\pi kT}\left[\frac{i_{signal}}{1+\exp\left(\frac{\Delta V_{BE}}{kT/q}\right)}\right]\frac{\gamma R_f}{R_2 C_1} \tag{29}$$

$$\Delta V_{BE} = -\frac{kT}{q}\ell n\left(\frac{i_{comp}}{i_{signal}} - 1\right) \tag{30}$$

$$\gamma = \frac{R_4}{R_4 + R_3} \tag{31}$$

Equations 8-10 can be used to determine the parameters to get the desired frequency response from the circuit. Low pass cut-off frequency of the circuit is determined by the feedback elements on *U1A* as explained in the previous sub-chapter. Thus, the feedback resistor and capacitor are selected based on the reasoning given there. The rest of the elements are selected to adjust the high pass cut-off frequency below 1 Hz. With these values, the cut-off frequency variation as a function of optical powers in the diffraction orders is shown in figure 46.

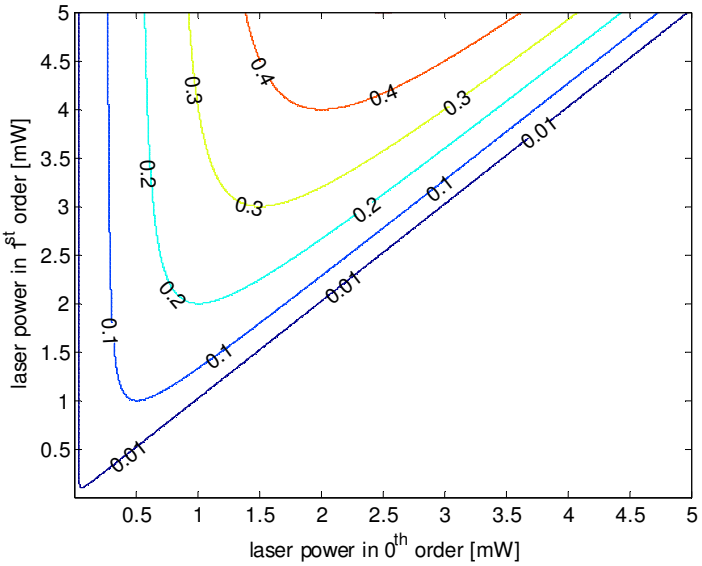

Figure 46. The variation of high pass cut-off frequency as a function of optical power in the diffraction orders.

With the values of the circuit elements shown on the schematic and the photocurrents for normal operation, the cut-off frequency is calculated to be less than 0.6 Hz. The frequency response of the designed circuit is simulated in PSPICE environment using Multisim Analog Devices Version 10.0 as shown in figure 47. There is a good agreement between the simulated response and the calculations.

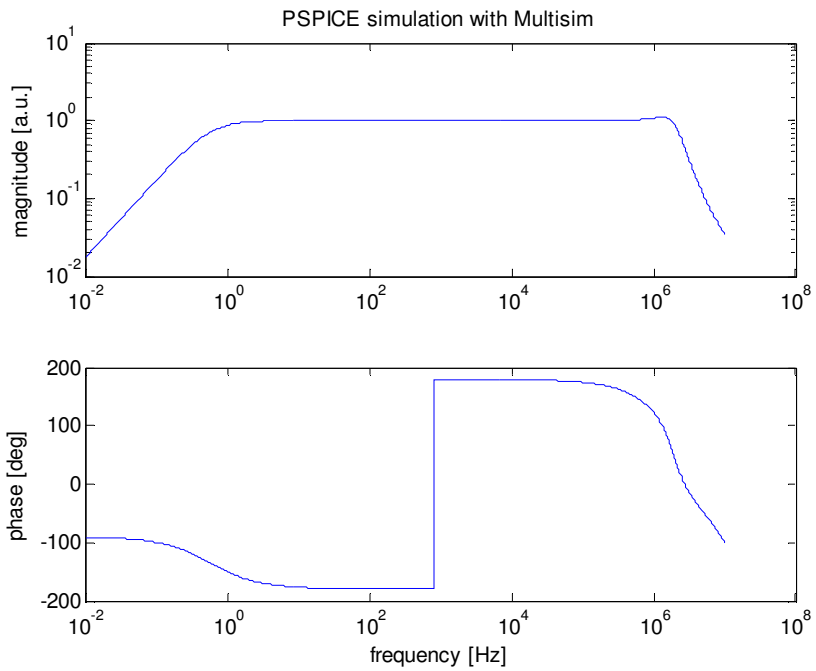

Figure 47. Simulated AC response of the laser noise canceller circuit.

Note that the comparison photocurrent, *I2*, in the original canceller circuit is purely DC. However, *I2*, in the circuit built for membrane probes is the photocurrent generated by 0^{th} order diffraction beam. So *I2* has both DC and AC components when the membrane operates. Since *I1* and *I2* are 90˚ out-of-phase, this should not affect the operation of the circuit as long as $I2_{DC} > I1_{DC}$ which is almost always the case. Yet, transient response of the circuit is simulated in PSPICE by assigning 100 μV_{peak} AC current on *I1* and 200 μV_{peak} AC current on *I2* to check the circuit operation. The output of the circuit generates linear voltage as shown in figure 48, verifying the circuit operation.

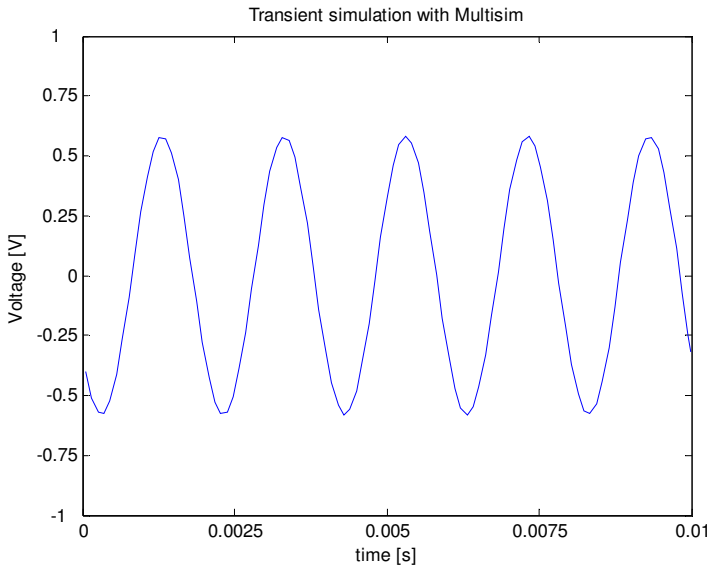

Figure 48. Simulated transient response of laser noise canceller circuit for a 100 μA_{peak} AC input on I_1.

Finally the noise characteristic of the circuit with a stiff silicon nitride/oxide membrane is shown in figure 49. For this experiment, a 200 μm diameter membrane was biased to its maximum sensitivity point and the noise was read from the PD outputs using a dynamic signal analyzer (Stanford Research Systems model # SR785). The differential readout scheme helped suppressing the RIN. It is clearly shown that shot noise limited operation starting from a few Hz is possible with this circuit. At low frequencies, two orders of magnitude improvement in detecting the membrane displacement is achieved with the differential signal when compared to the detection with first order signal. Overall, more than 20 dB noise suppression is achieved with differential detection.

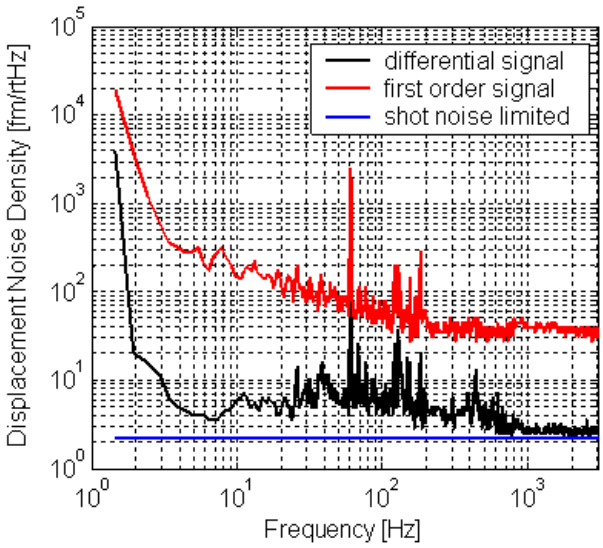

Figure 49. Measured displacement noise density with laser noise canceller circuit.

CHAPTER 5

EXPERIMENTAL CHARACTERIZATION

To use these active probes in single molecule mechanics experiments, both the electrostatic actuation and optical interferometric detection capabilities should be well characterized. The electrostatic actuator should provide suitable actuation range with a reasonable speed for biological experiments.

Detection of single-biomolecular interactions requires sensitive force sensors with low noise floor. Being dependent on the specific biomolecular system, the interaction forces can be as low as few pN- and even sub-pN-levels. These levels impose the operation of probes at the level of unity SNR when used as force sensors. Accordingly, noise behavior of membrane probes should be well characterized for biological experiments.

In this chapter, experimental characterization of the fabricated probes is presented. Details of actuation and detection capabilities of different types of probes are given for both in air and in fluid operation. For the device characterization, the setup shown in figure 38 is used.

Characterization of Probe Actuator

DC Actuation

Silicon nitride/oxide and parylene membranes on quartz substrate use parallel-plate type electrostatic actuators. For these devices, metallic diffraction gratings under the membrane serve as bottom electrodes. Diffraction gratings are patterned in square shapes and one side of the square equals to 60% of the diameter of the membrane. Membranes are actuated by applying bias voltage to the diffraction gratings while the top electrodes are connected to the electrical ground.

The deflection of a 200 μm diameter parylene membrane with increasing bias voltage was measured using a white light interferometer (Veeco Instruments, Wyko, Woodbury, NY). The gap height of the membrane without any bias was measured to be 2.23 μm. Figure 50(a) shows the gap height with increasing bias voltage. Profiles of the unbiased membrane and the membrane with 25V bias are shown in figure 50(b). This membrane was relatively soft (k=23 N/m) for actuation purposes and it is possible to displace the membrane by 400 nm at 25V bias.

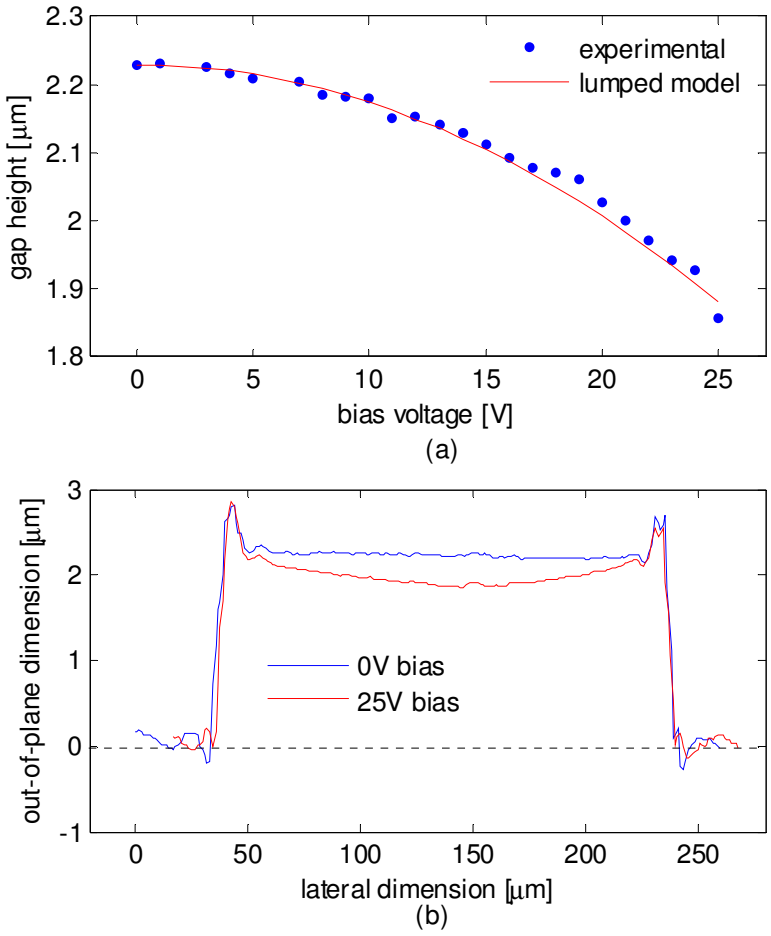

Figure 50 (a) Center deflection of a 200 µm diameter parylene membrane as a function of bias voltage measured with a white light interferometer. (b) The profile of the same membrane at two different bias voltages.

The other type of the electrostatic actuator for the probe membranes is the one with side electrode actuation. The parallel-plate actuator with side electrodes provides extended range as compared to a simple parallel plate type electrostatic actuator with uniform electrodes as shown in chapter 3 through FEM simulations. This eliminates the need for increasing the gap height significantly to increase the actuation range.

Non-uniform parylene membranes on Silicon use side electrode actuation method. For experimental characterization, the range provided by the actuator of a 150 μm diameter membrane was measured. Deflection of the membrane was measured by engaging an AFM cantilever at the center of the membrane. AFM cantilever monitored the displacement of the membrane as the voltage bias between the electrodes was increased. The spring constant of the membrane was 200 N/m and that of the cantilever was 0.01 N/m. The center portion of this membrane was not thinned down and it was used only as a rigid actuator. Since the membrane was much stiffer than the cantilever, the loading of the cantilever on the membrane due to the engaged cantilever was insignificant. Figure 51 shows that the membrane can be displaced more than 1.8 μm before it collapses to the substrate. The whole range requires less than 200 V-bias, which is comparable to the requirements of bulk piezo actuators commonly used in commercial AFM systems. The initial gap was 2.5 μm, and a simple parallel plate electrostatic actuator with this gap would provide a range of 0.83 μm before collapse. The electrostatic actuation with side electrodes increased the range of a simple parallel-plate electrostatic actuator by more than 100%.

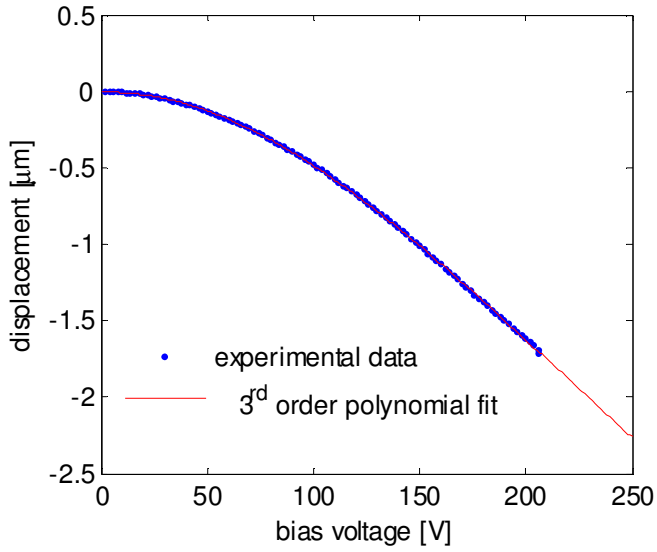

Figure 51. Displacement of a 150 µm diameter membrane with side electrode actuation as a function of bias voltage.

Dynamic Actuation

The electrostatic actuator should provide the demonstrated displacement range with enough bandwidth for fast pulling experiments. For dynamic characterization, the transducer was excited with a small amplitude AC voltage on top of the DC voltage for biasing the probe membrane deflection to the maximum sensitivity point. Membrane deflection was measured using the integrated interferometer to the membrane. Here, sensitivity is defined as the change in photodiode signal level divided by the change in membrane displacement.

First, a 200 µm diameter silicon nitride/oxide membrane with sealed etch holes was used for dynamic characterization. The resonant frequency of the membrane in air was ~1 MHz, which dropped to ~400 kHz when the membrane was operated in buffer

solution as shown in figure 52 (the small peak around 30 kHz was due to spurious coupling to the electronics). This is a rather stiff membrane (k~1000 N/m) designed for fast actuation purposes. It uses a simple parallel-plate type actuator and it is possible to displace the membrane by 200 nm with 50 V-bias. The flat response of the membrane in liquid up to resonant frequency exceeds the bandwidth requirements of molecular force spectroscopy.

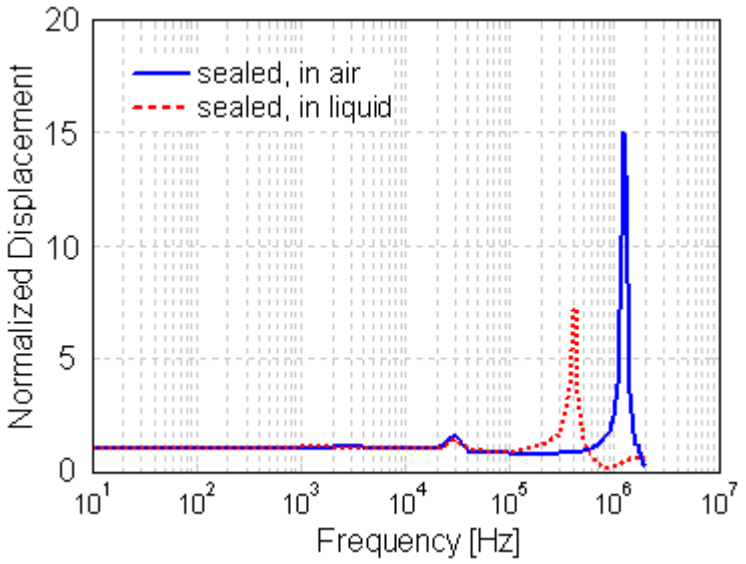

Figure 52. Measured dynamic response of the 200 μm diameter silicon nitride/oxide membrane on quartz. Stiffness of the membrane is ~1000 N/m.

Stiff membranes make fast actuators and their dynamics are not affected from squeeze-film damping effect. Flat response of the membrane shown in figure 52 verifies this fact. However for force sensing, the stiffness of the membrane should be kept small which can make the mechanical stiffness become comparable with the stiffness of air trapped under the membrane. That can be detrimental for the dynamics of the probe as described in chapter 3.

Figure 53 shows the dynamics of a 200 μm diameter parylene membrane on quartz substrate in air. The spring constant of the membrane was measured ~70 N/m. This moderate level of spring constant is suitable both for actuation and detection purposes. However, the measured dynamic response of the membrane shows that the membrane is under strong influence of squeeze-film damping. At only 400 Hz, displacement response of the membrane is reduced by 50% as compared to DC actuation levels. Although the pulling rate that can be provided with this membrane compares well with that of bulk piezo actuators, the advantage of fast membrane actuation is lost because of squeeze-film damping. Note that the resonant frequency of this membrane is about 1 MHz, comparable with that of the stiff silicon nitride/oxide membrane. This is due to the fact that the spring constant of air trapped under the membrane increases the effective stiffness of the system.

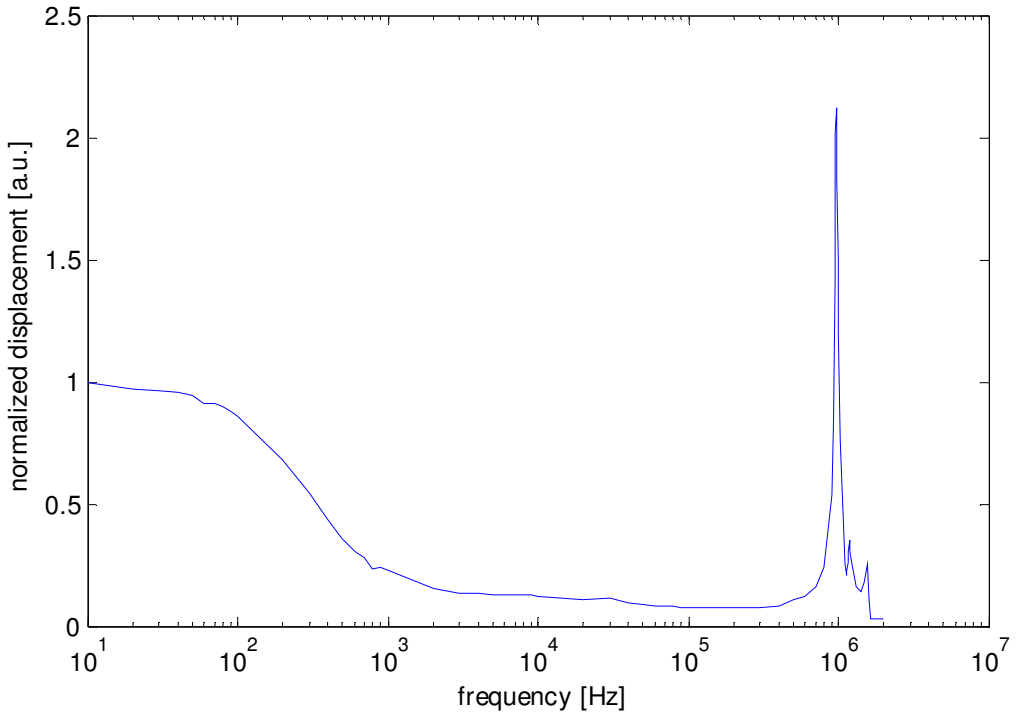

Figure 53. Dynamic response of the 200 µm diameter parylene membrane on quartz. Stiffness of the membrane is ~70 N/m. The membrane was in air with open etch hole.

The measurement shown in figure 53 was taken in air and the etch hole of the probe was open. When the membrane is under the strong influence of squeeze-film damping effect, the flow of air through the etch hole becomes important. Dynamics of a 150 µm diameter parylene membrane were experimentally obtained for three different cases as shown in figure 54 to illustrate this fact.

When the etch hole was left open, air under the membrane could freely escape through the etch hole at lower speeds, corresponding to lower actuation frequencies. However, at higher frequencies air had no time to escape and was trapped under the membrane. It behaved as an elastic spring, increasing the equivalent stiffness of the system. Thus the actuation amplitude dropped significantly.

When the etch hole was sealed, air was trapped under the membrane for the entire spectrum, thus increasing the equivalent stiffness. This flattened the frequency response of the membrane which is good for actuation purposes. However, increased stiffness reduces displacement sensitivity of the membrane when used as a force sensor. In liquid operation, the resonant frequency of the membrane shifted to lower frequencies due to the mass loading of the fluid. The quality factor also dropped, as expected, due to increased hydrodynamic damping.

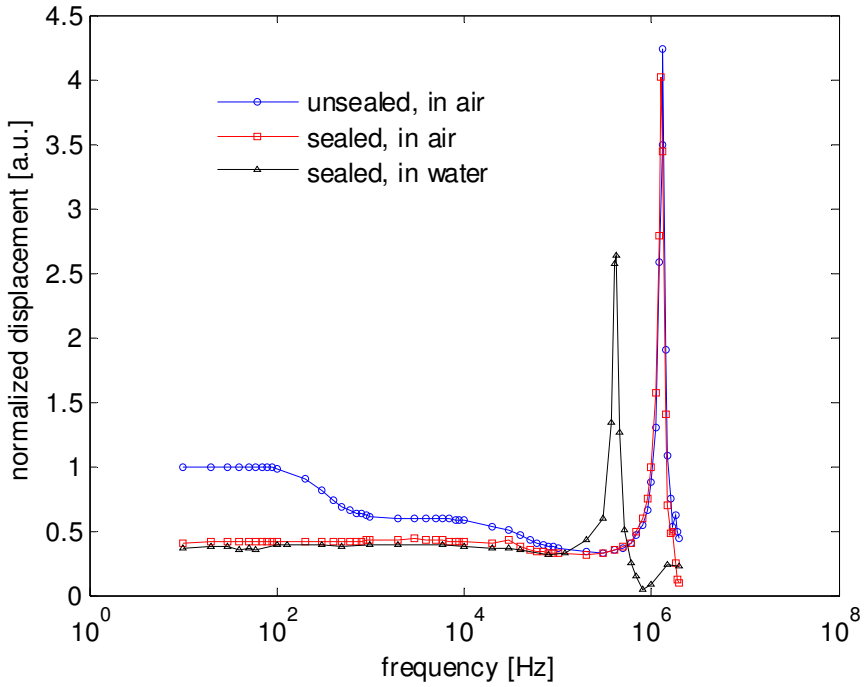

Figure 54. Dynamic response of the 150 µm diameter parylene membrane on quartz. Stiffness of the membrane is ~100 N/m. Dynamics of the membrane was obtained both when the etch hole was left open and sealed.

The focus of the design effort for the non-uniform parylene membranes on silicon is to optimize both the actuator and the force sensor simultaneously. For this, the probe

dynamics should not be affected adversely by squeeze-film damping effect even for softer membranes. This problem is effectively solved by opening vent holes under the membranes. Vent holes provide free air flow for improved device dynamics.

Figure 55 shows the experimentally obtained frequency response of a 200 μm diameter non-uniform membrane. The detector membrane at the center is not thinned down and the spring constant of the membrane was measured ~150 N/m. The resonant frequency of the membrane in air was measured to be 365 kHz, which was predicted well with the lumped model of the membrane. The resonant frequency of the same membrane was measured to be 36 kHz in fluid. The drop in resonant frequency can be explained by fluid loading due to radiation pressure of vibrating membrane in fluid. A lumped model including this effect is in good agreement with the experimental data. Additional damping was introduced to the model to match the quality factor measured experimentally. The membrane dynamics is free from squeeze-film damping effect and flat response up to the resonant frequency ensures the use of the actuator effectively for fast pulling experiments.

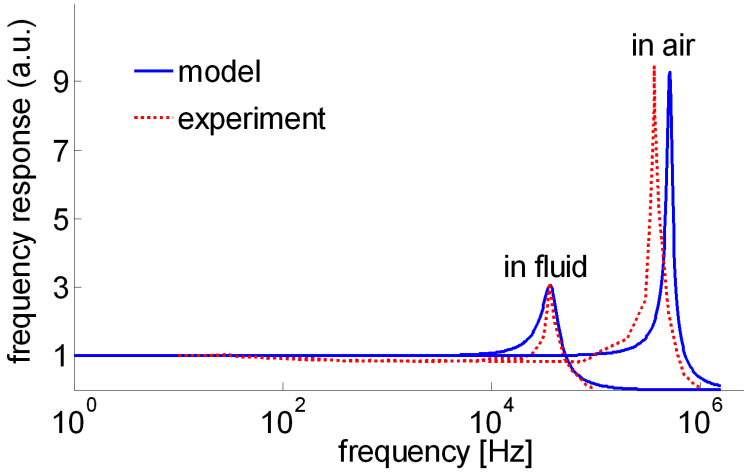

Figure 55. Dynamic response of the 200 µm diameter non-linear parylene membrane on silicon. Stiffness of the membrane is ~150 N/m.

RMS operation, explained in chapter 3, also relies on dynamic actuation of the membrane probes. RMS operation helps preventing electrolysis problem in fluid as explained earlier. In this mode of operation, the input signal to the membrane is modulated with a high frequency square wave. A 240 µm diameter non-uniform parylene membrane on silicon was tested accordingly. The resonant frequency of this membrane in fluid was measured around 30 kHz. A sine wave at 100 Hz was modulated with a 600 kHz square wave as shown in figure 56(a) and fed into the electrostatic actuator of the membrane in fluid. The measured deflection of the membrane in time domain is shown in figure 56(b). The membrane, due to its frequency response, behaved as a low pass filter and followed the sine wave at 100 Hz nicely but it effectively filtered out the square wave at 600 kHz. The mean of the input signal was zero, and no electrolysis was observed when the membrane was operated for about an hour. The polarity of input voltage changed fast enough (at 600 kHz) to prevent electrolysis when the mean of the signal was adjusted to zero.

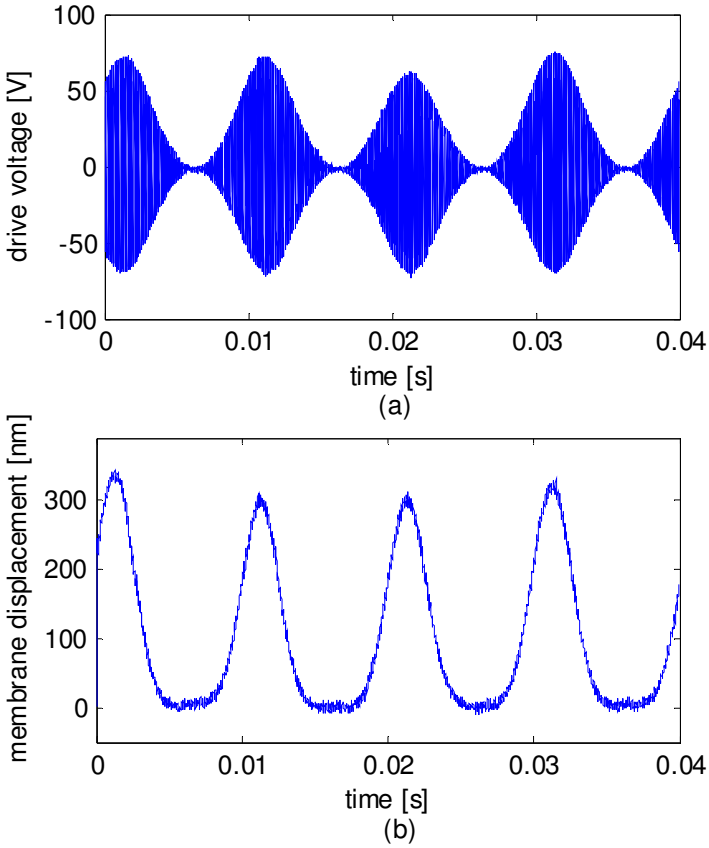

Figure 56. (a) Drive signal fed into the electrostatic actuator of a 240 μm diameter non-linear parylene membrane on silicon. 100 Hz signal was modulated with a 600 kHz square wave. (b) Membrane displacement measured at the center.

Parallel Operation

The experimental results presented show that micromachined probe membranes can be individually actuated for single molecule force spectroscopy measurements. Furthermore, arrays of these membranes have already been fabricated as shown in figure 31(g). A natural extension of this approach shows a path to parallel force measurements where individually actuated membranes are used to conform to stationary cantilever

arrays as shown schematically in Fig. 11. With this method, the force exerted by the cantilever tips on the molecules under investigation can be precisely controlled. Note that, in this configuration the molecular interaction forces are still measured using the AFM cantilevers, but since the pulling motion is provided by the individual active probe membranes, the cantilevers don't have to be individually actuated, thus eliminating a significant bottleneck for single molecular assays. Since the membranes in the array configuration are individually actuated, it is possible to electrostatically bias the membranes to compensate possible fabrication non-uniformities across the membrane actuator array. An acceptable level of non-uniformities in an array configuration has already been demonstrated and characterized using CMUT array structures [78].

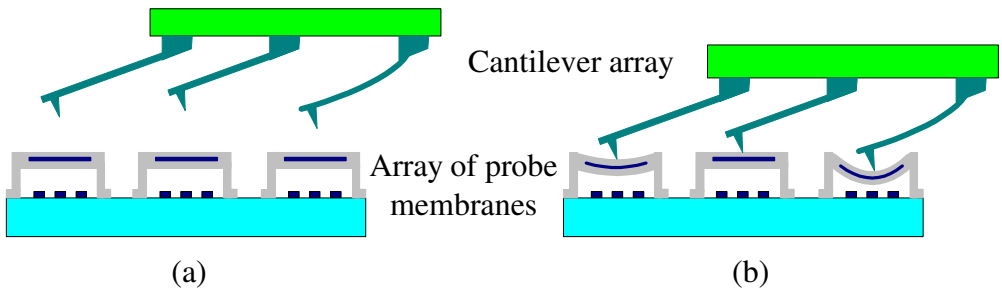

Figure 57. (a) Schematic of array of individually actuated membrane transducers used as a locally actuated sample surface under a stationary AFM cantilever array. (b) It is possible for individually actuated transducer membranes to conform to the AFM cantilevers after engagement to compensate possible non-uniformities.

A proof of principle experiment shows the feasibility of the method of actuating parallel cantilevers and reading them simultaneously. The experimental setup built for this experiment is shown in figure 58. A 8-cantilever array developed by IBM was used in this experiment [79]. The cantilevers on this chip do not have sharp tips by default but tips were grown on cantilever-1 and cantilever-8. This allows engaging the cantilevers

controllably on a membrane chip mounted on a piezo transducer. The optical setup allows the detection of cantilever-1 and cantilever-8 simultaneously using optical lever method with a single laser source.

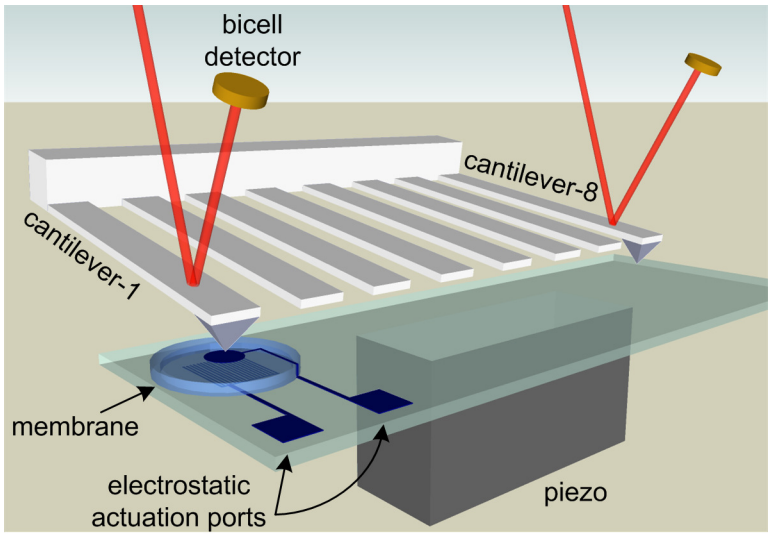

Figure 58. Schematic of the parallel operation setup.

The experiment was performed by engaging cantilever-1 on top of a 100 µm diameter silicon nitride/oxide membrane while cantilever-8 was in contact with the quartz substrate. Figure 59 shows the recorded force traces when the piezo actuator was turned off and the membrane was actuated as shown. This data shows the feasibility of reading out parallel cantilevers simultaneously and the capability of individual cantilever actuation.

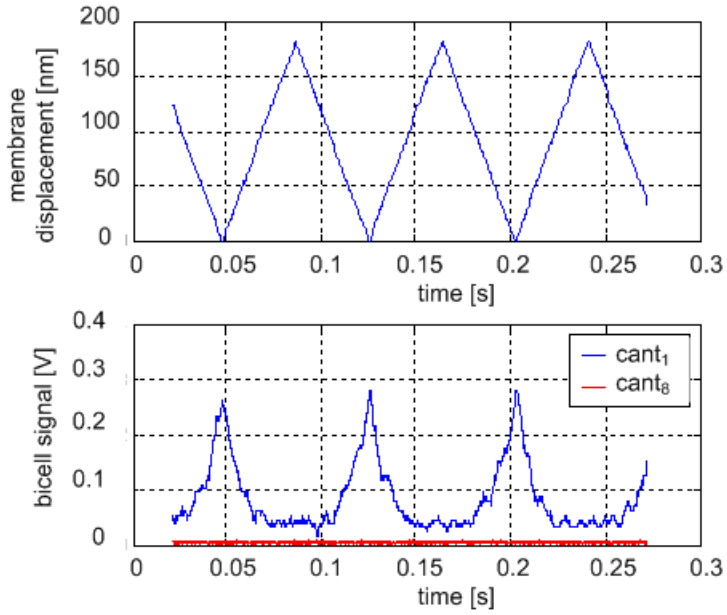

Figure 59. Membrane actuator was ON and piezo was OFF. The readout signals captured from the cantilevers show that only one cantilever can be actuated.

In another attempt, both cantilevers were actuated to make sure that they were engaged on the substrate. Figure 60 shows the cantilever readings when cantilever-1 was actuated by combined displacement of the piezo and the membrane while cantilever-8 was following the piezo displacement.

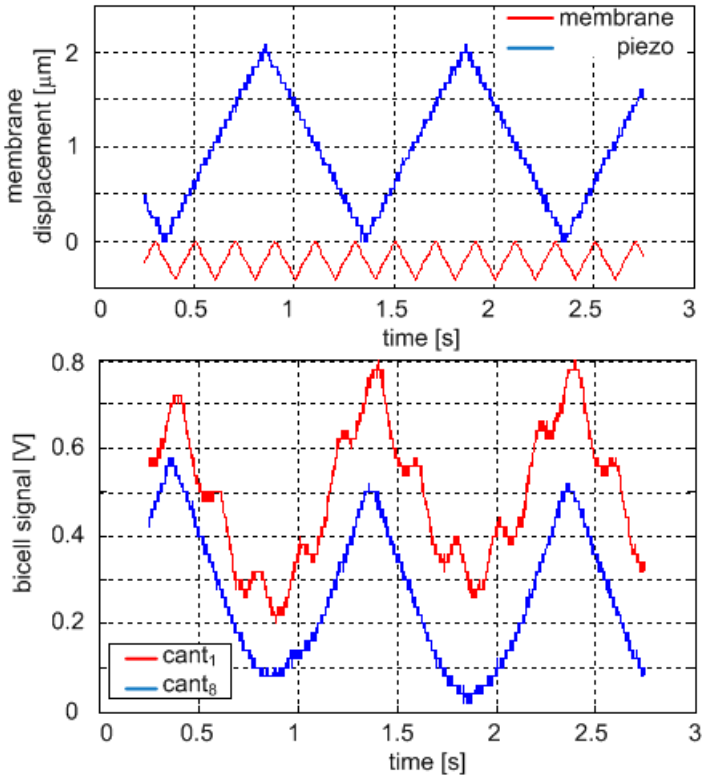

Figure 60. Both actuators were ON. The readout signals captured from the cantilevers show that cantilever-8 follows the piezo whereas cantilever-1 follows the combined actuators.

Characterization of Probe Sensor

Silicon nitride/oxide membranes have better displacement resolution when compared to parylene membranes with similar size. Assuming the damping is comparable between membranes with similar size, the force noise is comparable. Thus, silicon nitride/oxide membranes with large stiffness have lower displacement noise. This is advantageous when they are used as actuators. High displacement resolution makes it possible to control the actuator precisely with a feedback loop. On the other hand, large stiffness reduces force sensitivity, i.e. the change in photodiode signal level divided by

the change in force applied on the membrane. Thus parylene membranes provide higher SNR than silicon nitride/oxide membranes given their lower stiffness.

Both types of probe sensors should be well characterized before using them for biological experiments.

Optical Curves

For experimental characterization of the detection performance with silicon nitride/oxide membranes, a 500 μm diameter transducer membrane with a diffraction grating period of 3.3 μm was used. The membrane was actuated by applying voltage difference between the electrodes (top electrode and diffraction grating) while monitoring the intensity of light in the diffraction orders using the PD array. Figure 61 shows the measured intensity variations (in terms of voltage) in the diffraction orders as a function of applied DC bias voltage to the actuator. The intensity of the 0^{th} and 1^{st} orders changed periodically as the gap height changes due to the applied voltage, as expected. The modulation efficiency, i.e. percentage change in photodiode signal, was 77% for the 0^{th} order and 95% for the 1^{st} order. Since light reflects off of the substrate also goes to 0^{th} order, it is expected to have lower modulation in 0^{th} order.

The same experiment was repeated under a white light interferometer to measure the membrane displacement independently as a function of applied bias voltage. Membrane displacement is proportional to the square of voltage as explained before and the experiment shows that for a bias voltage of 50 V, this particular membrane was displaced by ~ 200 nm. Combining these data sets, the optical interference curve is

mapped to the membrane displacement as shown in figure 61(b). The interference curve shows a nearly sinusoidal dependence to membrane displacement with a period of 210 nm. The deviation of the curve from the ideal case can be due to several reasons including the membrane curvature, the angular spectrum of the incident light beam and possible vectorial effects not considered in the scalar formulation used to derive equation 1.

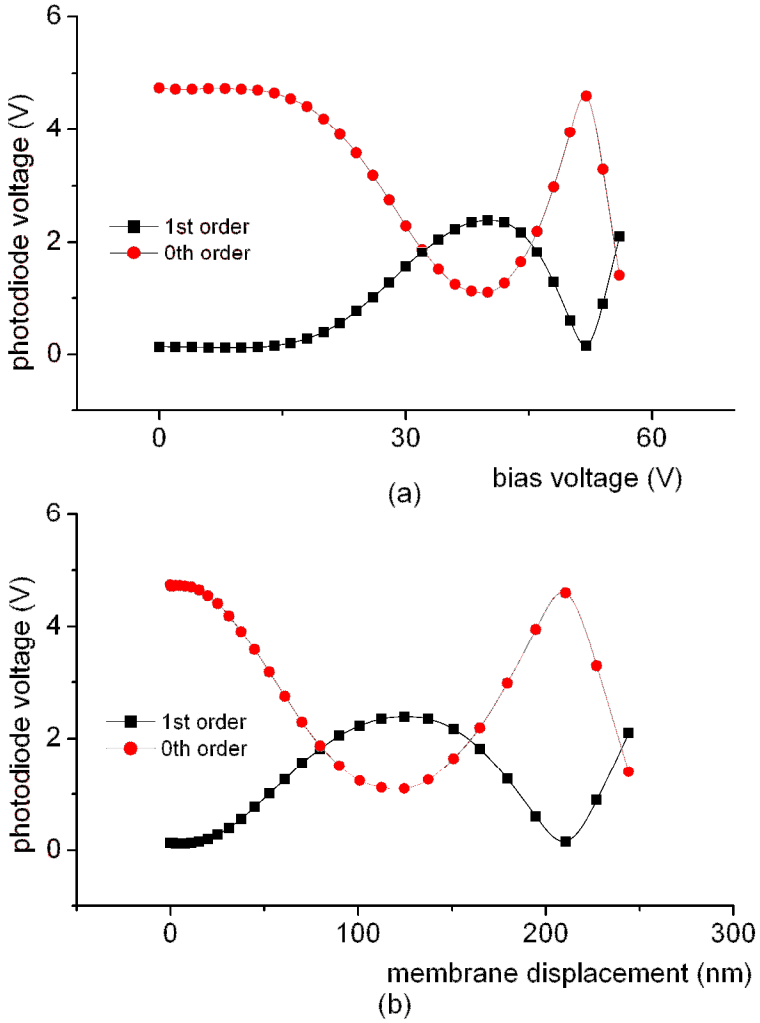

Figure 61. (a) The variation of photodiode output with the applied DC bias voltage (b) The variation of photodiode output with the membrane displacement. A 500 μm diameter silicon nitride/oxide membrane was used for the characterization. The membrane was unsealed and was in air.

Grating interferometer for non-uniform membranes on silicon comprises the reflector pad on the membrane and the diffraction grating glued to the backside of the silicon substrate. The gap height between the grating and the membrane includes the thickness of the silicon wafer, which is 350 μm. Comparing this extended gap height to the gap height of the membranes on quartz, which is less than 5 μm, it can be said that the non-uniform membranes are more sensitive to misalignment or incidence angle of the laser. Nevertheless, good modulation efficiency can be obtained with care. Figure 62 shows the optical curves obtained with a 240 μm diameter non-uniform membrane. The inset, showing the normalized values for the photodiode signals, can be used to calculate the modulation efficiencies. The efficiency of the 0^{th} order signal was measured 45.7% and that of the 1^{st} order signal was measured 90.2%. Note that the membrane was actuated such that the optical curves spanned more than 3 periods and the modulation of the orders reduced as the membrane was biased further towards its substrate. Increasing membrane curvature with increasing bias voltage can explain this observation. Yet for sensing applications, membrane can be biased on the first period of the optical curve for better dynamic range.

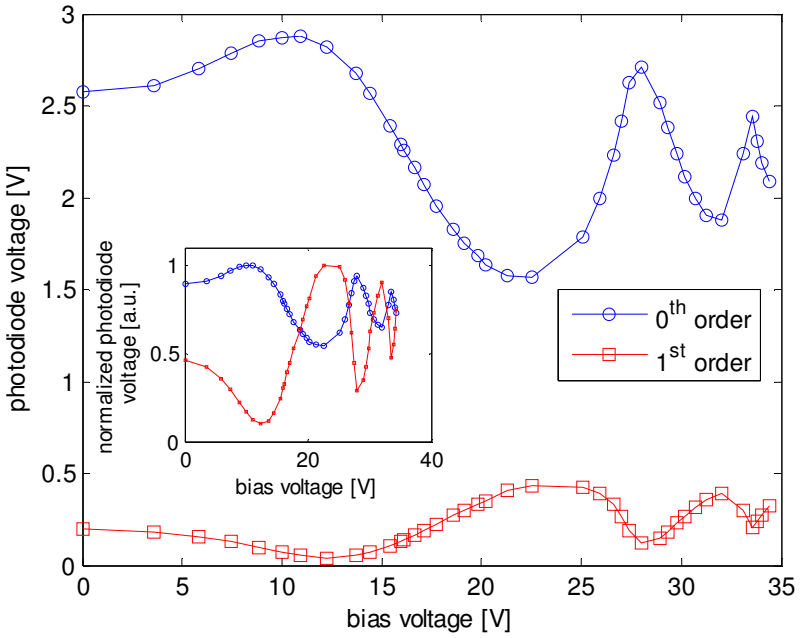

Figure 62. The variation of photodiode output with the applied DC bias voltage for a 240 μm diameter non-uniform parylene membrane on silicon. The inset curve shows the normalized photodiode signals to compare modulation efficiencies.

Noise Characterization

Basic sources of noise in the system can be classified as shot noise in the photodetectors, thermo-mechanical noise of the mechanical structure, electronics noise and laser noise. Among these, electronics noise and laser noise can be controlled well as explained in chapter 4 and kept below the limit of shot noise and thermo-mechanical noise as. So, shot noise and thermo-mechanical noise determine the noise performance of the probes.

Thermo-mechanical noise arises in any system at thermal equilibrium when the ambient temperature is finite. Considering an oscillator of any kind, fluctuations in the

equilibrium temperature imposes random motion on the oscillator. This process is the basis for the thermo-mechanical noise. Thermo-mechanical noise is also named as mechanical-thermal noise or simply thermal noise. J. B. Johnson was the first to discover and quantitatively analyze the thermal noise in an electrical circuit [80]. Same year, in 1928, H. Nyquist developed the theoretical basis for the thermal noise observations [81]. In his work, Nyquist stated the relationship between random fluctuations of voltage (E) across a resistor (R) to equilibrium temperature (T) as follows:

$$E^2 dv = 4Rk_B T dv \tag{32}$$

Where dv is the measurement interval and k_B is the Boltzmann's constant. Nyquist also showed that the simple theorem is valid not only for total fluctuation but also for fluctuations within any frequency. H. B. Callen and T. A. Welton generalized this theorem from quantum mechanical perspective and showed that equation 32 can be reformulated for any system to quantify the relationship between any dissipation process in a system and associated fluctuations [82]. Accordingly, the following relationship holds for a linear dissipative system:

$$\left\langle V^2 \right\rangle = \left(2/\pi\right) \; k_B T \int R(\omega) d\omega \tag{33}$$

Where $\left\langle V^2 \right\rangle$ is the mean square value of the spontaneously fluctuating force, R is the generalized resistance and ω is the angular frequency. An immediate application of this generalized relationship is to calculate thermo-mechanical noise in a simple harmonic

oscillator (SHO). A Langevin equation governing the dynamics of a SHO with mass m, spring constant k, and mechanical resistance R is given as:

$$m\frac{d^2z}{dt^2} + R\frac{dz}{dt} + kz = F_n(t) \tag{34}$$

Where z represents the motion of the oscillator and $F_n(t)$ represents random force with zero mean and a constant power spectral density. Solving the equation for the spectral density of displacement ($Z_n(f)$) gives [83]:

$$\left|Z_n(f)\right| = \frac{\sqrt{4k_BTR}}{k}\frac{1}{\sqrt{\left[1-(f/f_0)^2\right]^2 + (f/f_0)^2/Q^2}} \tag{35}$$

Note that equation 35 is analogous to equation 20 given in chapter 2. This simple, yet powerful, model has been used to explain thermal noise associated with several types of micromachined devices [83, 84]. Here, the dominant dissipation source is viscous damping (R). Besides this model, the spring itself can be a source of dissipation. The noise arises in this case is called viscoelastic noise for which an associated model assumes a complex spring constant, $k(1+j\phi)$ [85, 86]. Then, the spectral density of displacement can be expressed as in equation 36.

$$\left|Z_n(f)\right| = \frac{4k_BT}{k\omega_o}\frac{1/Q + \phi/u}{\left(1-u^2\right)^2 + \left(u/Q + \phi\right)^2} \tag{36}$$

where ωo is the angular resonant frequency, Q is the quality-factor and u=ω/ωo. Viscoelastic noise is usually seen with laminated structures such as bimaterial cantilevers [86].

For the parylene membranes on silicon, the mechanical structure is a single layer of parylene with a small metallic circle at the center. Then, the noise characteristics of these membranes can be modeled using equation 35. The model of equation 35 for a 200 μm diameter parylene membrane with uniform thickness predicts the thermal noise and the shot noise levels for the membrane in fluid is on the same order. Power spectral densities of thermal noise and the shot noise below 1 kHz are 0.29 and 0.34 pN/√Hz, respectively; bringing the total noise floor with 1 kHz bandwidth to 14 pN. Figure 63 shows the measured force noise spectrum along with the model for this membrane. A SHO model was fitted to the experimental spectrum and associated lumped parameters were extracted.

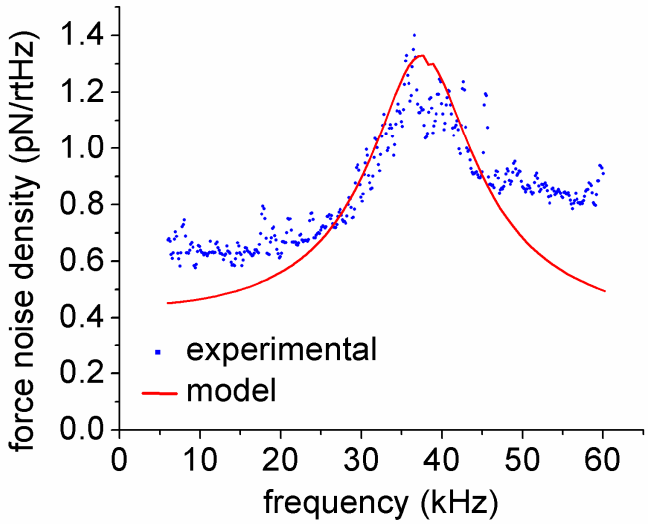

Figure 63. Force noise spectrum of a 200 µm diameter non-uniform force probe in fluid. The membrane is made of parylene and the center detection membrane is not thinned down. The spring constant of the membrane is 150 N/m.

The total noise floor of the probes is lowered by simply thinning down the detection membrane. Thinning down the detection membrane reduces its spring constant which in turn reduces the shot noise component of force noise. Lower spring constants also increase the signal levels, thus improve SNR. By adjusting the thicknesses of detection membrane and the actuator section carefully, the actuator section can be designed much stiffer. Thus, thermal noise associated with the force detection part is limited to that of the detection membrane. Minimizing the moving area reduces the viscous damping of the structure and this helps reducing thermal noise component of force noise.

Force noise power spectral density obtained with a 500 µm diameter probe with 300 µm diameter detection membrane in fluid is shown in figure 64. The spring constant of the detection membrane was measured 8 N/m. Based on the measured spring constant

and the photocurrent in the photodiodes; the shot noise below 1 kHz was calculated to be 0.13 pN/√Hz. A SHO model with viscous damping was used to fit the resonance behavior of the membrane in fluid. This model predicts thermal noise below 1 kHz to be 0.22 pN/√Hz. Total noise (shot and thermal) spectrum is also shown in figure 64 and is in good agreement with the measurements. Moreover, the viscous damping of the membrane can be calculated independently with the approach described in chapter 2. Discussion on hydrodynamics of the membrane in fluid can be followed to calculate the viscous damping spectrum of the membrane. Calculated total force noise with the consideration of the hydrodynamic model is also shown in figure 64.

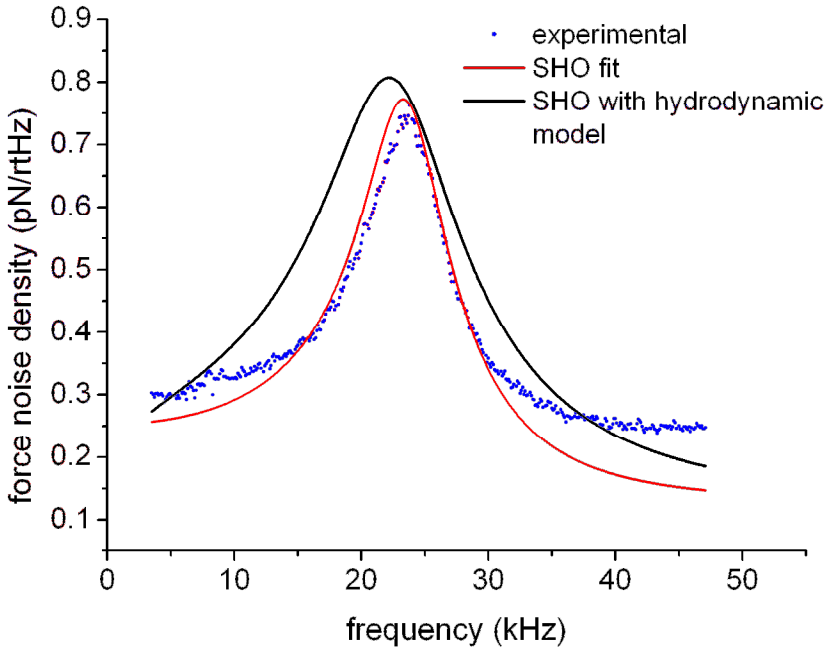

Figure 64. Force noise spectrum of a 500 μm diameter force probe with 300 μm diameter detection membrane in fluid.

The total noise floor of this sensor with 1 kHz bandwidth in fluid is 8.1 pN. The force resolution of current probes is comparable to that of commercially available

cantilevers. For example, the thermal noise floor of a 200 μm long rectangular cantilever (from Veeco Instruments Inc.) with a nominal spring constant of 0.02 N/m is 8.4 pN with 2 kHz bandwidth in fluid [87].

For a comparison of force curves simultaneously captured with a membrane probe and an AFM cantilever, we coupled this 500 μm diameter force probe with a rectangular silicon cantilever (FESP, Veeco Instruments Inc.) in fluid. The selection was based on the similar spring constants of the sensors. Nominal spring constant of this cantilever is 2.8 N/m and the spring constant of the probe was measured 8 N/m. Moreover, the resonant frequency of an FESP tip was previously reported to be 30 kHz in fluid with a quality factor of 3.8 [88]. Considering the similar values of resonant frequency and quality factor measured with the membrane, it is reasonable to select this cantilever for the comparison.

The cantilever was actuated in and out of contact with the probe membrane and the force curves were simultaneously captured using the optical lever readout of the cantilever and the diffraction grating interferometer of the probe. Figure 65 shows the captured force curves when the peak force on the cantilever was set such that the signal-to-noise ratio (SNR) on the cantilever is unity. This membrane compared to the specific cantilever used here was able to resolve lower forces although its spring constant is larger than that of the cantilever.

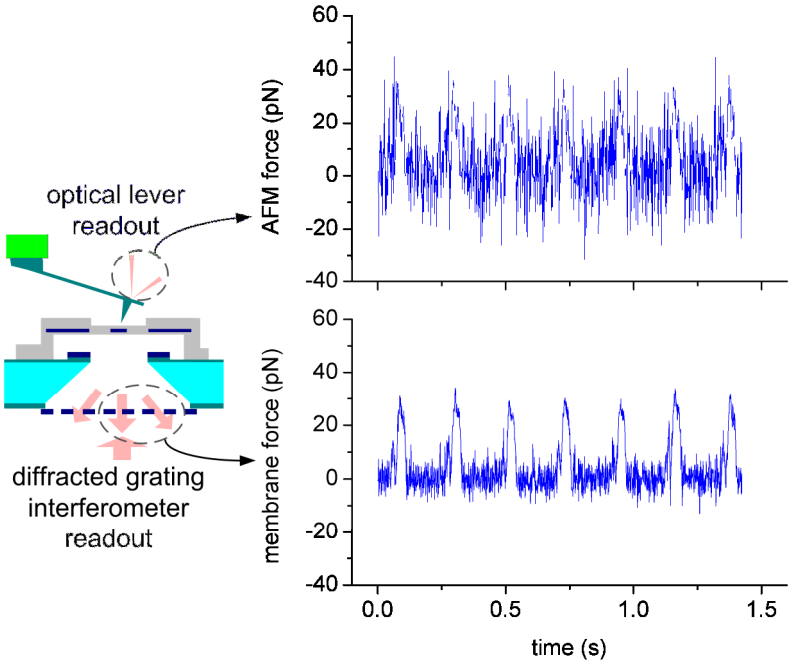

Figure 65. Comparison of force curves obtained by the AFM cantilever and the membrane probe when a 2.8 N/m cantilever was actuated against a 8 N/m membrane in fluid. The peak force on the cantilever was set such that SNR=1.

CHAPTER 6

BIOLOGICAL EXPERIMENTS

Functionalization of parylene membrane surfaces

Parylene C, a hydrophobic crystalline polymer, has been used as the mechanical structure as explained in this thesis. It also forms the outer layer of the membrane that is in contact with AFM cantilevers in biological experiments. Deposition of parylene layers requires a CVD process and polymerization following this. It is chemically inert, non-toxic and ideal for biomedical applications [89, 90].

Parylene coatings are hydrophobic in nature and strongly discourage adhesion of proteins and cells on to their surfaces. However, it is absolutely mandatory that the membrane surface would anchor the biomolecules without compromising on the molecular functionality. It has been reported that treating parylene surfaces by oxygen plasma reduces hydrophobicity [70, 91, 92]. The process recipe for O_2 plasma in a RIE chamber is given in Table 1.

Table 4. RIE process recipe for O2 plasma

O_2 gas flow	40 sccm
Pressure	500 mTorr
Power	200 W
DC-Bias	440 V

The compatibility of treated parylene surfaces with biomolecular force spectroscopy experiments was systematically evaluated by employing a qualitative adhesion probability measurement method. For this, the experimental setup shown in figure 66(a) was used.

The parylene membrane surfaces were coated by 100 ppm polyethylenimine (PEI) solution (Fisher Scientific, PA) to accommodate the occasionally inversely oriented selectins. Then lipid vesicle solution was coated on the surface (3-5 µL and incubated for 15-20 min). Membranes were finally covered by Dulbeccos Phosphate Buffered Saline (DPBS) solution (Fisher Scientific, PA) containing Ca^{2+}, Mg^{2+} and 1% Bovine Serum Albumin (BSA). The membranes were then tested against AFM cantilevers with tips coated either with BSA or DREG56 (an anti-L-selectin antibody). Interaction between L-selectin and DREG56 was expected which would mean high adhesion probability.

PEI cushion helps accommodating the inversely-oriented selectins during lipid bilayer formation. Absence of the PEI cushion would create a bumpy and non-uniform bilayer, which would thus lead to a high degree of sticking between the AFM tip and the membrane. On the other hand, absence of RIE treatment would mean that the membrane surface stays hydrophobic. This would thus lead to a non-uniform bilayer formation on the surface and thereby lead to a high % of non-specific adhesion.

When either the membranes were treated with RIE treatment the non-specific adhesion frequency dropped dramatically as shown in figure 66(b). This clearly suggested that RIE treatment of the parylene surfaces made them hydrophilic, viable for conducting biological experiments. In the second part of the surface characterization,

AFM tips with DREG56 were tested against the same bilayers. Accordingly, the adhesion frequency increased sharply, indicating specific adhesions between L-selectin and DREG56 figure 66(b). This clearly demonstrated that RIE treatment of parylene surfaces made them hydrophilic, conducive for carrying out single molecular biological studies.

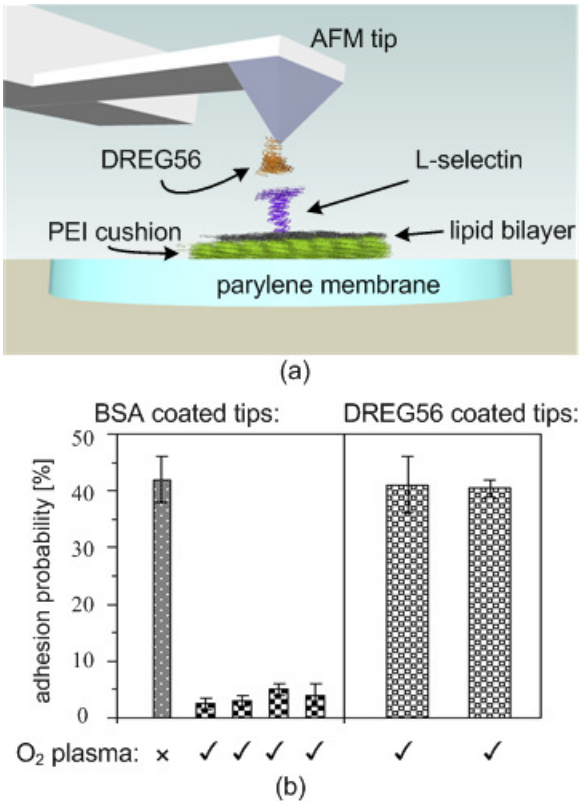

Figure 66. (a) Functionalization of AFM tip and parylene membrane to evaluate parylene surface treatment. (b) Adhesion probability data gathered using both BSA coated and DREG56 (an anti-L-selectin antibody) coated AFM tips tested against L-selectin bilayers.

Pulling experiment with probe actuator

The same biological system used to characterize parylene surface modification was selected as a biological test system for the force spectroscopy experiments with silicon nitride probe actuators. L-selectin is an adhesion molecule on the surface of white blood cells. During inflammatory response, white blood cells use L-selectin to tether to and roll on tissue vasculature [93]. Unbinding force strength and adhesion probability between L-selectin and DREG56 were studied in this experiment.

An AFM tip and a 200 μm diameter silicon nitride probe membrane were functionalized using the same protocol explained before and shown in figure 67(a). Initial experiments were performed by repeatedly moving the AFM tip with the piezo-actuator of the commercial AFM system while the probe membrane was kept stationary as shown in figure 67(b). The interaction forces were detected from the optical lever detection mechanism of the AFM system. Figure 67(c-d) shows typical force curves with rupture forces comparable to previously published data [94]. Upon testing, the adhesion frequency (i.e. the fraction of binding events) was ~ 40%, consistent for several different membrane-tip pairs, thus demonstrating repeatability and reproducibility of the biological protocol used. In order to clearly demonstrate the specificity of the observed interactions, control experiment was performed wherein the L-selectin in the bilayer was blocked using excess DREG-56. Upon blocking, the adhesion frequency dropped dramatically to 6%, at par with nonspecific adhesion levels. This suggests that an intact bilayer with reconstituted L-selectin was formed on the surface of the membrane probe, which not only supported specific L-selectin interaction with DREG-56 but also presented a small

fraction of nonspecific interactions. The majority of the binding events exhibited only single breaks, with progressively small numbers of binding events that showed double as well as triple breaks, which is consistent with Poisson distribution and suggests that each break represents unbinding of a single L-selectin-DREG-56 bond.

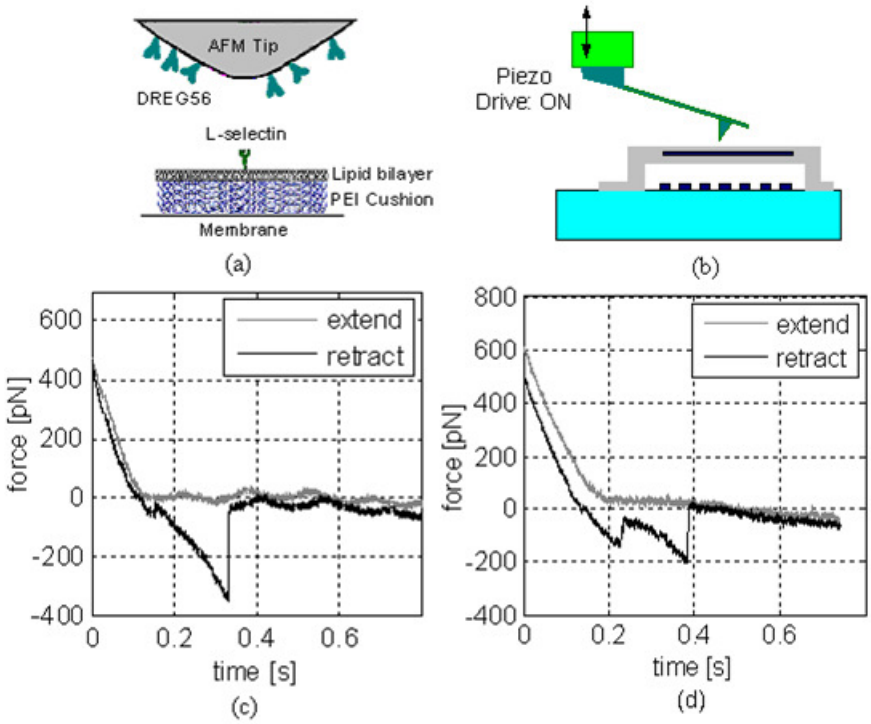

Figure 67. (a) Functionalization of the membrane-based probe and the AFM cantilever with biomolecules; (b) Schematic of biological experiment with a stationary membrane and a piezo-actuated AFM cantilever; (c) Representative single-break force curve and (b) double-break force curve (black trace) obtained during the experiment.

In subsequent experiments, the piezo actuation was disabled and the probe membrane was actuated using the built-in actuator as sketched in figure 68(a). To test the actuator under liquid, the AFM cantilever was pressed on the membrane, which was driven with a 5 V-peak triangular wave at 5 Hz. Since the piezo was turned off, the

cantilever bending should be caused by the membrane deflection, which is proportional to the square of the actuation signal, shown in figure 68(b). In support of this contention, the measured force time course ramped up for about 0.05 s and then ramped down as shown in figure 68(c), concurrent with the time course of the voltage applied to drive the membrane. Then the AFM cantilever was lifted slightly so that the membrane movement would bring it in and out of contact with the cantilever. The experiment was repeated to detect the possible rupture events. Figure 68(d) shows a typical force curve so obtained. Initially the cantilever and the membrane were out of contact so the cantilever force remained zero as the membrane moved up. When the membrane made contact with the cantilever, the compressive force increased accordingly, i.e. when the slope of the curve is positive. Then the membrane moved down together with the cantilever with a negative slope on the force curve. Before the membrane moved out of contact from the cantilever, a clear adhesion event was detected. The cyclic operation went on in this manner and a total of two rupture events were detected out of four for the force time curve shown in figure 68(d). The observed unbinding forces are in agreement with the previous experiment in which the piezo-drive was active and the membrane was stationary, shown in figure 68(c-d).

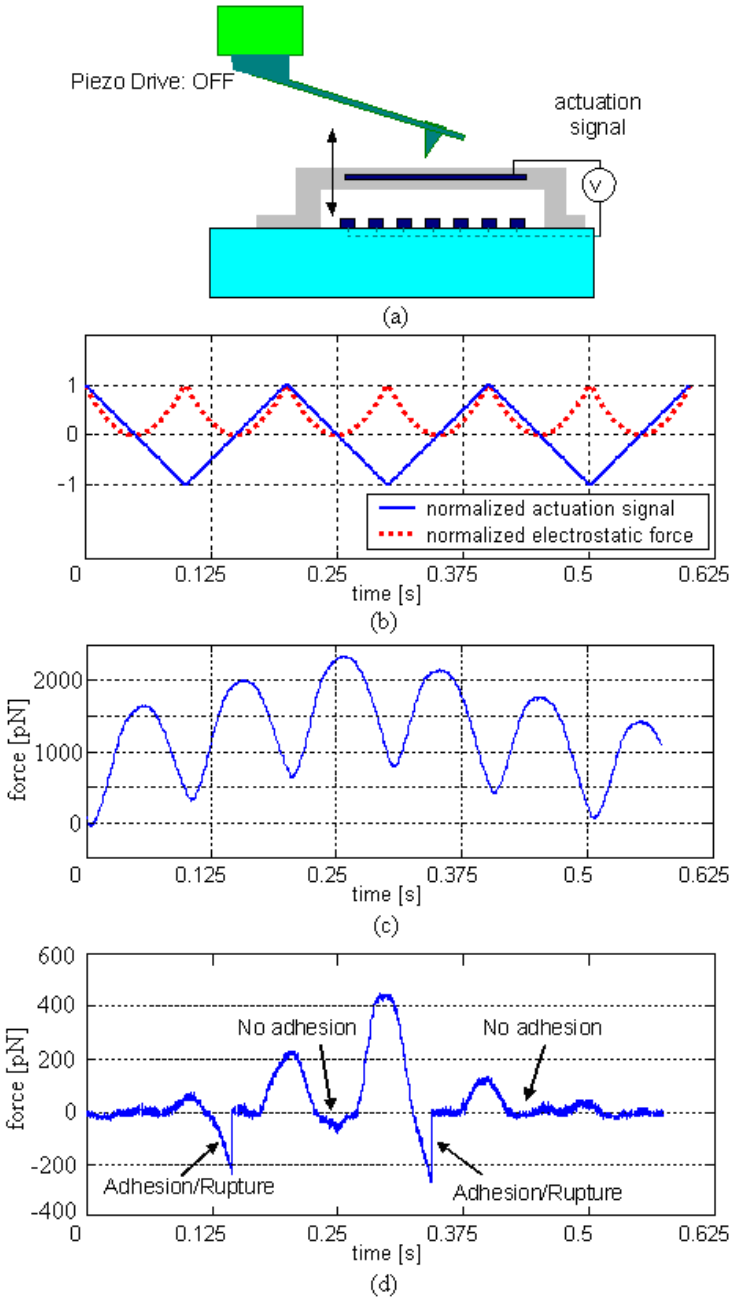

Figure 68. (a) Schematic of biological experiment with electrostatically actuated active probe membrane and disabled piezo-drive for the cantilever; (b) The actuation signal applied to the probe membrane and the generated electrostatic force, which is proportional to the square of the actuation signal; (c) The cantilever and the probe membrane were in full contact and moved together; (d) The detected rupture events as the probe membrane was actuated into and out of contact with the AFM cantilever.

Fast pulling experiment with probe actuator

One motivation to use probe actuator is the capability of fast pulling. Actuation bandwidth of probe membranes in fluid (tens of kHz for parylene, hundreds of kHz for silicon nitride membranes as shown in chapter 6) is several orders of magnitudes larger than that of commercial bulk piezo actuators. Moreover, surface-actuated cantilevers by probe membranes feel an order of magnitude smaller drag forces as compared to piezo actuation [95]. Fast pulling capability with probe actuator was experimentally tested using a 300 μm diameter parylene membrane on silicon. The center part of the membrane was not thinned down and a spring constant of ~150 N/m was measured at the center of the membrane.

Interactions between human IgG and a counter antibody (anti-human IgG) were tested in this experiment. Biomolecules were purchased from Sigma-Aldrich (St. Louis, MO). Membrane was incubated with 10-20 μl of anti-human IgG (10 μg/ml) for 15-20 min at room temperature and excess antibody was washed off with DPBS (Sigma-Aldrich) containing 1% BSA. AFM cantilevers were incubated with 10 μl of human IgG (10 μg/ml) for 15-20 min at room temperature.

Binding specificity was first tested as shown in figure 69(a). The membrane was coated with anti-human IgG and was tested against three different cases. When bare AFM tips were used adhesion probability was measured <10%. The adhesion probability increased drastically when AFM tips coated with human IgG were used marking inter-molecular interactions. Finally when the human IgG coated AFM tips were incubated

with excess anti-human IgG, an adhesion probability of <10% was measured, indicating that the functionalization protocol worked.

Force spectroscopy experiment with accordingly functionalized membrane and AFM cantilevers (MLCT-C and MLCT-D, Veeco Instruments) was performed by actuating the membrane by applying voltages < 50 V, at speeds between 10 and 100 μm/s. A stationary cantilever was used only for force sensing. Figure 69(b) shows a force curve recorded using the AFM cantilever when the membrane was actuated at a speed of ~ 100 μm/s. The minimal hydrodynamic drag on the AFM cantilever is strongly demonstrated by the cantilever snapping back to its mean resting position (horizontal black line) immediately after bond rupture, though the membrane was moving at ~ 100 μm/s.

Additionally, several other pulling experiments were performed by using piezo actuator of the cantilever for comparison purposes over a range of retraction speeds till hydrodynamic effects become comparable with the interaction forces. To reach a loading rate of 10^5 pN/s the cantilevers were actuated at speeds > 10 μm/s, encountering few tens of pN drag force in the process.

Unbinding force histograms obtained with both cantilever pulling and membrane actuation are shown in figure 69(c). Number of approaches is written on the histograms for each pulling rate. The distributions have the characteristic bell-shape. Membrane actuator was used to gather data with pulling rates $>10^4$ pN/s. Piezo actuator of cantilevers cannot be used effectively in this range due to hydrodynamic drag forces. Data shows that the results obtained with both methods compare well and they are combined together to generate force spectrum as shown in figure 69(d). Force spectrum is

generated with peak values of the unbinding forces and the fitted line with single slope suggests that there is a single energy barrier under the set conditions [13, 96, 97].

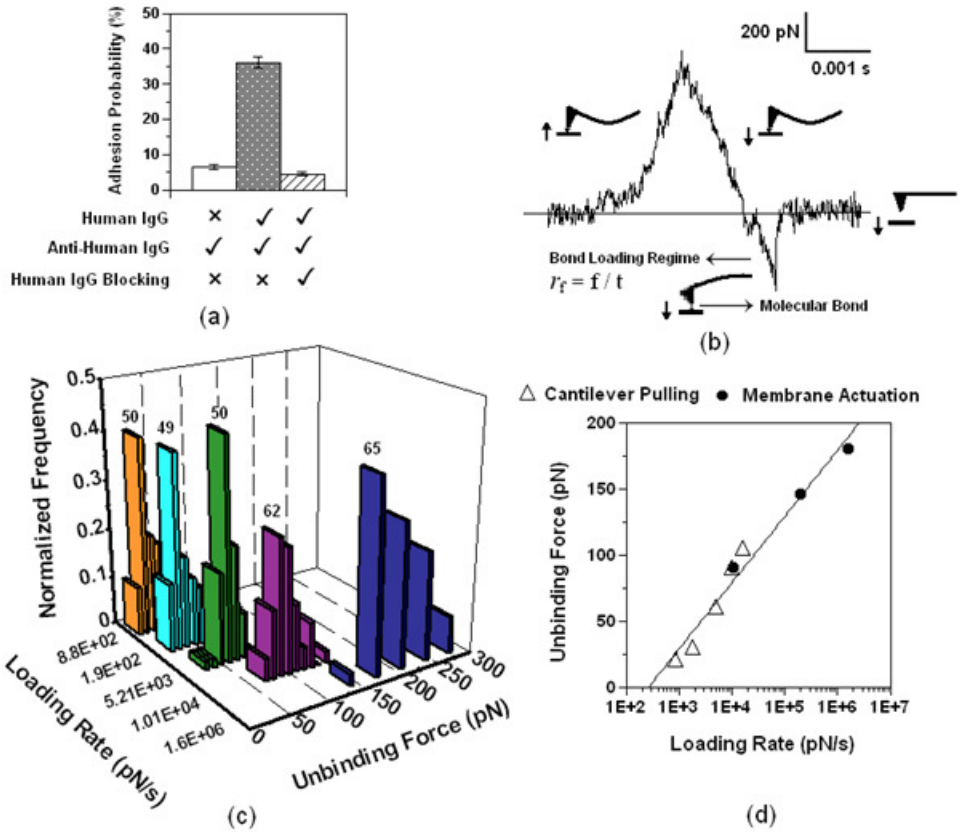

Figure 69. (a) Binding specificity in antibody experiments. (b) A typical force curve obtained with membrane actuation. Relative motion of membrane was shown with small arrows. (c) Unbinding force histograms obtained with both cantilever pulling and membrane actuation. Data correspond to a loading rate of ~10^6 pN/s was obtained with probe actuation. (d) Unbinding force spectrum obtained.

Force-clamp experiment with probe actuator

Open-loop operation of probe actuator makes pulling experiments possible. Fast-pulling experiments with this operation mode are especially important as they can address some biological problems for which conventional cantilever actuation cannot be used. When controlled in a feedback loop, force-clamp force spectroscopy experiments are possible with probe actuators. The force-clamp setup built for biological experiments is shown in figure 70. Here, AFM cantilever is still used as the force sensor. During the operation, readout of the cantilever (hence the force on it) is compared to a set value. The generated error signal is processed and corresponding actuation signal is fed to the membrane probe to keep the force on the cantilever constant.

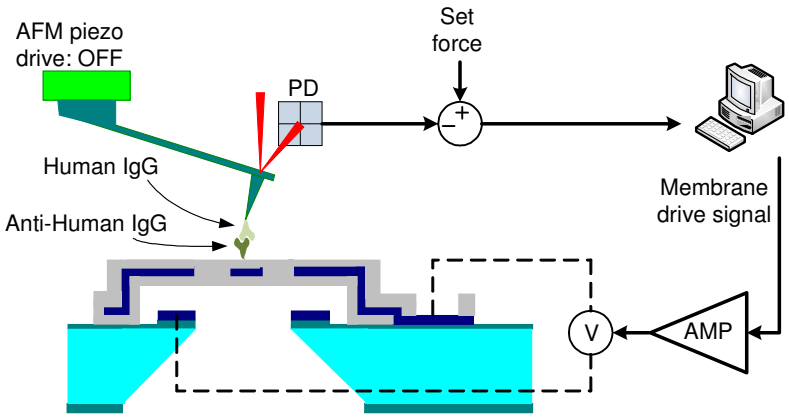

Figure 70. Force-clamp setup with probe actuator.

Force-clamp setup was used to probe interaction forces between human IgG and anti-human IgG. The membrane used for this experiment was a 200 µm diameter parylene membrane on silicon and a spring constant of 150 N/m was measured at its center. The membrane was coupled to an AFM cantilever with 10 pN/nm spring constant

(MLCT-C, Veeco Instruments Inc.). Both structures were incubated as explained before. Figure 71 shows an exemplary force trace and corresponding membrane displacement. The experiment was performed with AFM cantilever brought in contact with the membrane and then membrane was displaced at t=0 such that the force measured by the cantilever met the set value of 80 pN. The membrane actuator compensated for the disturbances to keep the force level constant until the biomolecular bond ruptured at t=0.38s.

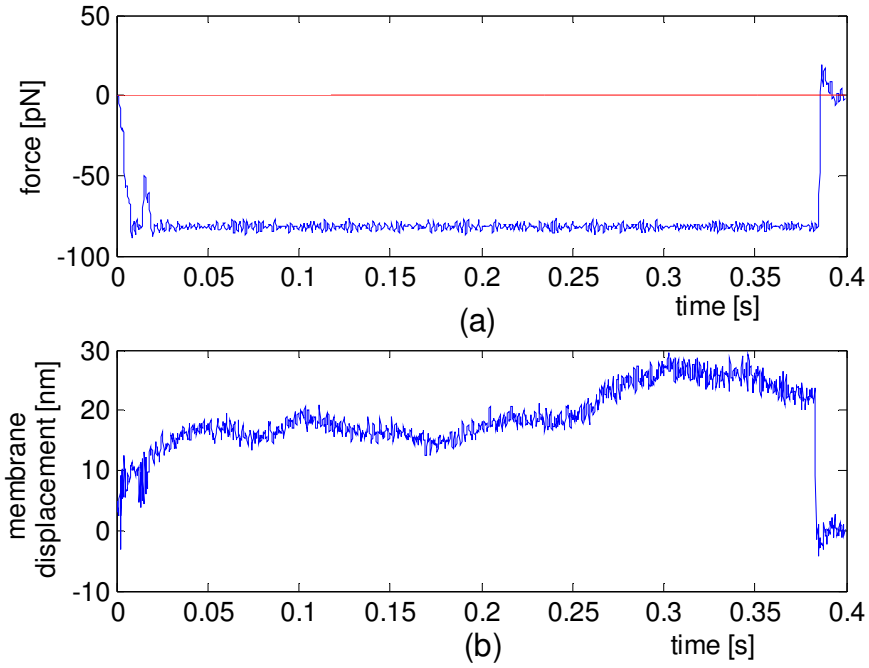

Figure 71. (a) Force trace measured with AFM cantilever with clamping force set at 80 pN. (b) Membrane displacement (based on the signal fed to its actuator) from clamping the force at set-point to the rupture of biomolecular bond.

Figure 72 shows some of the several force traces recorded using the same membrane for a clamping force of 50 pN. Force-clamp method allows the direct measurement of life-time for the biomolecular bond under investigation for different

loading forces. The lifetime spectrum obtained using force-clamp setup was compared with simple Monte-Carlo (MC) simulations for the molecular pair. The MC simulations were based on the results of a pulling experiment done to extract so called Bell parameters: k_{off}^{0} and x_{β}, the off-rate at the absence of force and the barrier width, respectively.

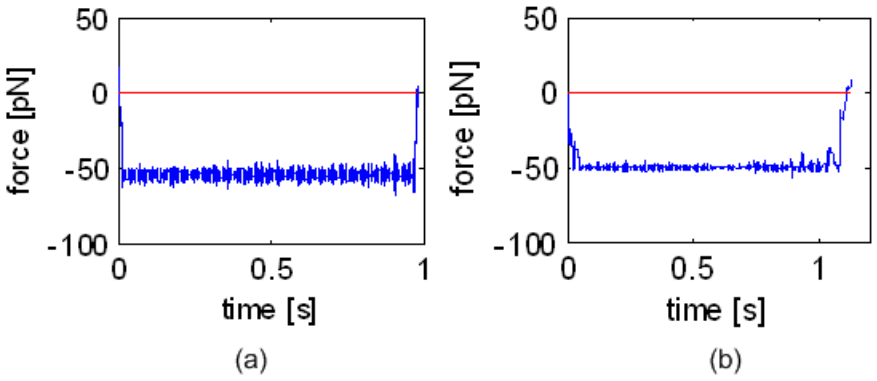

Figure 72. Force traces measured with AFM cantilever with clamping force set at 50 pN.

The experimental setup for the AFM pulling experiment is shown in figure 73(a). An incubated AFM cantilever was tested against a functionalized surface to extract Bell parameters for the interaction between human IgG and anti-human IgG. An extraction method introduced lately was followed. This method is based on the fact that the data acquisition is done by sampling at constant rate [98].

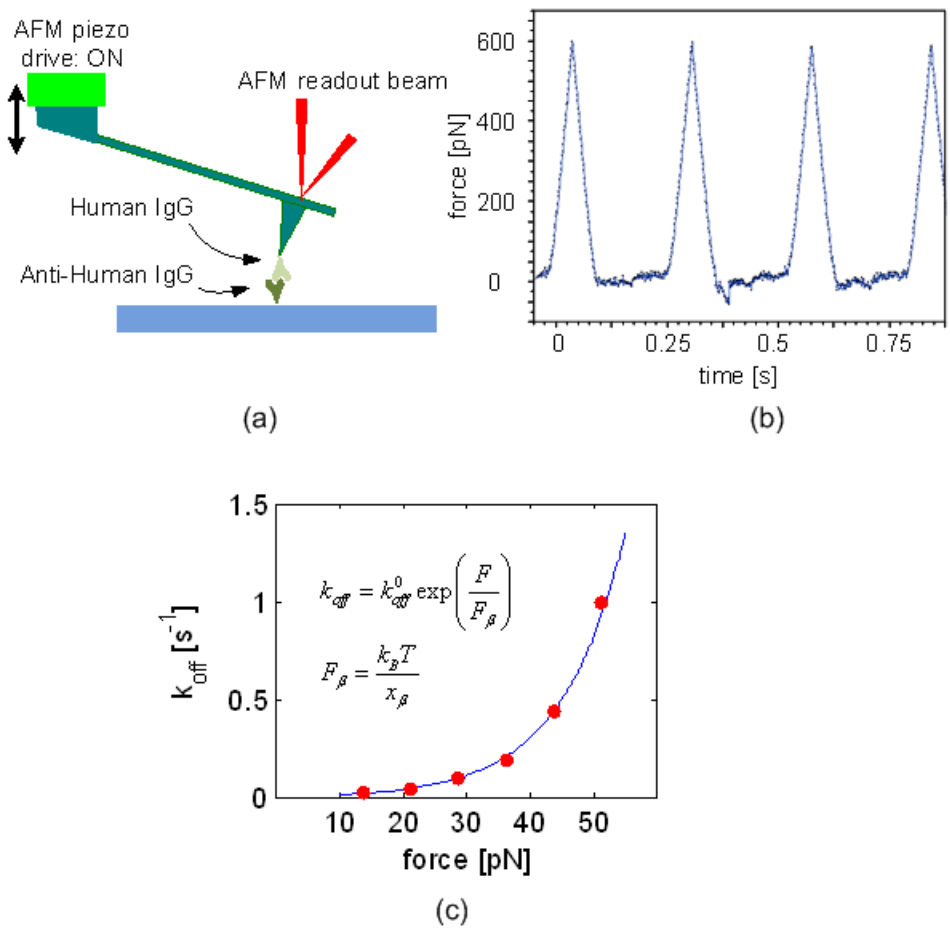

Figure 73. (a) Experimental setup for the AFM pulling experiment to extract Bell parameters. (b) Representative force curves showing one adhesion/rupture event together with two null events. A total of ~1200 force curves were recorded during the entire experiment. (c) Extraction of Bell parameters by fitting an exponential curve to the variation of off-rate as a function of force bin widths. This method is explained in detail elsewhere [98].

After a total of ~1200 force curves were recorded, the results were combined together as shown in figure 73(c). From the best exponential fit; k_{off}^0 and x_β values were determined as 0.0055 s^{-1} and 0.41 nm, respectively. Simple MC simulations to predict lifetime spectrum for a specified clamping force require these value. For a fixed force applied (F) on the bond, the thermal force (F_β) and the off-rate (k_{off}) is fixed and given as:

$$F_\beta = \frac{k_B T}{x_\beta}$$
$$k_{off} = k_{off}^0 \exp\left(\frac{F}{F_\beta}\right) \tag{36}$$

MC simulations comprise of a recursive comparison of instantaneous unbinding probability for time step ΔT with a random number between 0 and 1. Instantaneous unbinding probability is given in equation 37 and if it is larger than the random number, bond is assumed broken [99]. If not, time is stepped up until the bond gets broken. The time when the bond is broken is considered as the lifetime.

$$P_{rupture} = 1 - \exp(-k_{off} \Delta T) \tag{37}$$

Figure 74 shows the distribution of life-times when MC simulation was run for a clamping force of 50 pN. Life-time distribution is in a shape of exponential distribution as expected. The mean value for the fitted probability density function is 1.24s. This value validates the findings the results of force-clamp experiments independently.

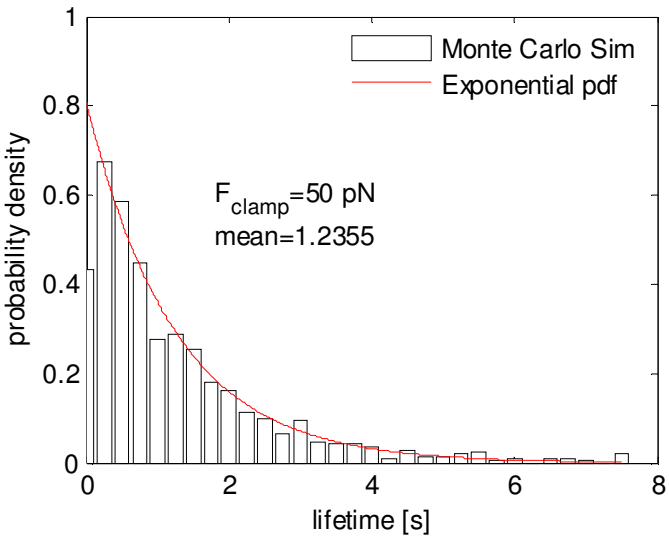

Figure 74. Distribution of life-time obtained by simple MC simulations for a clamping force of 50 pN. The mean value for the fitted exponential pdf is determined to be 1.24s.

Pulling experiments with probe sensor

Parylene membranes on silicon have been used both as an actuator and force sensor for biomolecular force spectroscopy experiments. Unbinding forces between biotin and streptavidin were measured by using these membranes to demonstrate their use in biological experiments. For these experiments, pre-functionalized cantilevers with biotin (CT. BIO, Novascan Technologies, Inc., AMES, IA) were purchased. The spring constant of the cantilevers were 14 N/m.

One of the cantilevers was coupled with a 500 μm diameter membrane. The spring constant of the membrane was measured 60 N/m at its center. The center part of the membrane was not thinned down, the thickness was uniform. After removing the cantilever from the sealed pack, it was incubated with ~20 μl of streptavidin (concentration: 10 μg/ml) that has an extremely strong affinity for biotin and the probe

membrane was functionalized with biotinylated BSA (Bovine Serum Albumin). The membrane was then covered with Dulbecco's Phosphate Buffered Saline (DPBS) solution (Sigma-Aldrich Inc., St. Louis, MO). Streptavidin has 4 binding sites for biotin. It is expected that two of those sites would be used to strap them onto the biotin on the AFM cantilever, leaving the other 2 sites free for binding with the BSA on the membranes. Incubating the membranes with BSA helped block the rest of the surface, helping to minimize nonspecific adhesion. Figure 75(a) shows the schematic of functionalized membrane and cantilever couple.

Experiments were performed by repeatedly moving the AFM cantilever with the piezo-actuator of the commercial AFM system at 2 Hz while the probe membrane was kept stationary. Figure 75 shows the captured force curves showing adhesion/rupture events. The strength of the specific event is ~ 220 pN. The adhesion frequency (i.e. the fraction of binding events in 100 repeated test cycles) was between 30-40%. At such a binding frequency, bulk of the interactions would involve single molecular pairs, according to small number statistics. The findings are in good agreement with data presented previously using similar parylene membranes [100].

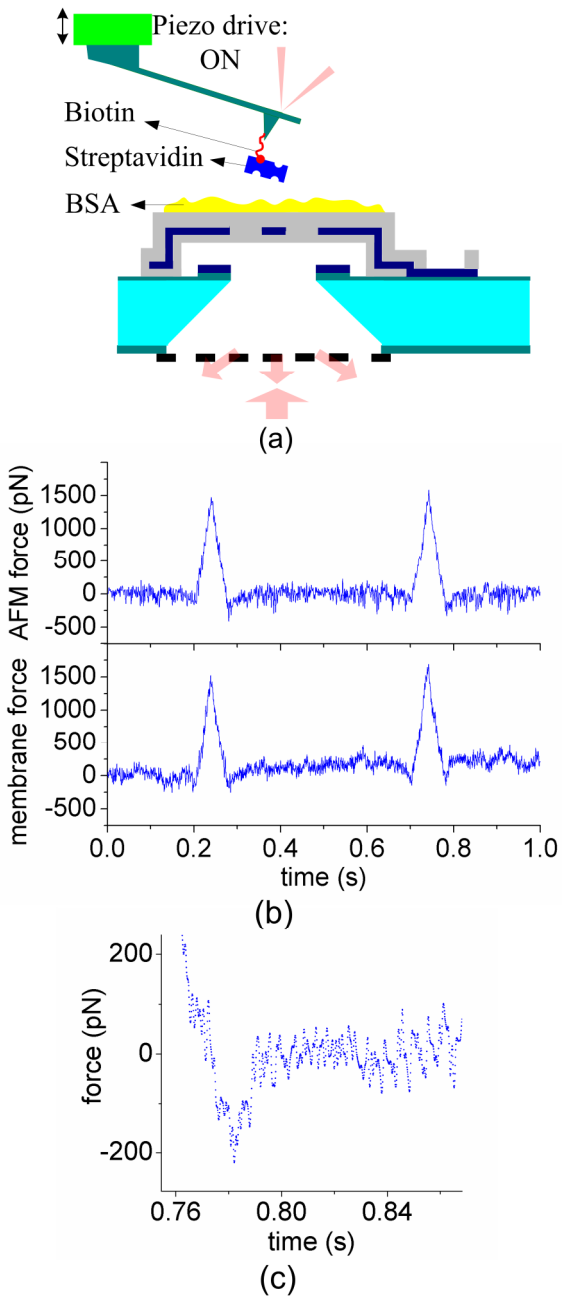

Figure 75. (a) A biotin and streptavidin coated afm cantilever tested against a functionalized membrane probe with biotinylayted BSA. (b) Simultaneously captured force curves from afm system and the membrane probe showing adhesion/rupture events. (c) Closer view of rupture event detected with the membrane probe.

CHAPTER 7

SPRING CONSTANT TUNING OF ACTIVE PROBES

In a conventional AFM system, a passive, microscale cantilever is used as the force sensing element to measure the interaction force between the sharp cantilever tip and the sample surface. The spring constant of the cantilever depends on geometry and material properties, and it is permanently set once the cantilever is fabricated. Although this is advantageous for stability purposes, it also limits the range of physical properties that can be effectively realized with a cantilever. For example, if one reduces the lateral dimensions of the cantilever to achieve low thermal noise in fluids, the thickness needs to be decreased to simultaneously keep the spring constant at its original value. In addition, one needs to fabricate multiple cantilevers with different spring constants to probe samples of different surface stiffness effectively, and without damage.

The spring constants of membrane probes, on the other hand, can be tuned electrically using spring softening phenomenon. This method is used to soften the membrane type active probes developed for force spectroscopy experiments to improve force sensitivity. In addition to force spectroscopy applications, this capability can be effectively used to optimize a single probe for quantitative characterization of different surfaces with different viscoelastic properties

Spring Softening Phenomenon

Further reduction of spring constants of already fabricated membranes is possible by using the electrostatic actuation capability. Due to inherent nonlinear nature of the electrostatic forces, this type of actuator enables one to adjust or tune the stiffness of the coupled mechanical structure for small displacements around an equilibrium point determined by the bias voltage and the initial stiffness [42]. This so-called spring softening effect has been used as a frequency tuning method for micromachined resonator devices [101],[102]. Researchers have also studied spring softening effect to model parallel-plate type microstructures accurately such as cantilever beams and membranes [103],[104].

Force resolution for force spectroscopy measurements improves by reducing the mechanical sensor's coefficient of viscous damping. It was shown that smaller cantilevers can measure smaller forces since they have smaller viscous damping [24]. On the other hand, given the microfabrication constraints, the spring constant of the cantilever scales inversely with shrinking the cantilevers. The value of spring constant is fixed for passive cantilevers once they are fabricated, which is not necessarily the case for the active probe membranes. The use of spring softening capability essentially adds another knob to adjust the probe properties on demand which is not available in passive AFM cantilevers. With this capability, one can adjust the sensitivity of force measurements and decouple the optimization of spring constant and the viscous damping coefficient of the probes for thermo-mechanical noise limited force spectroscopy measurements. The idea of using spring softening effect with membrane probes is summarized in figure 76. An ideal probe

has low viscous damping which is the case for smaller structures and at the same time it has lower spring constant which is the case for larger structures. Smaller probes fabricated for low viscous damping can be softened electrostatically for force spectroscopy experiments as shown in figure 76(b).

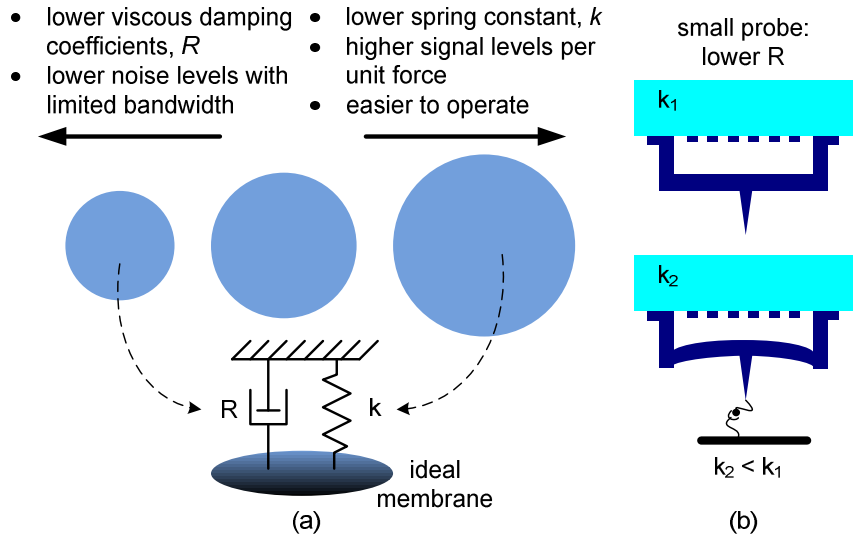

Figure 76. (a) Summarizing the effect of physical size of membranes (b) Application of spring softening with membrane probes to achive low viscous drag and small spring constant at the same time.

The spring constant of the membrane vibrating in electrostatic field is reduced by increasing the electromechanical coupling coefficient (k_T) suggested by spring softening effect:

$$k' = k(1 - k_T^{\,2}) \tag{38}$$

where *k'*, *k* are the softened and unbiased membrane's spring constants, respectively. The reduction in spring constant increases as the DC bias voltage is increased and the membrane gap is reduced since the coupling coefficient increases with increasing membrane displacement:

$$k_T^{\,2} = \frac{2x}{d_0 - x} \tag{39}$$

where x and d_0 are the membrane displacement and initial gap height, respectively. Based on equation 38 and 39, it is possible to bring the spring constant of the membrane virtually to zero at the collapse voltage. Figure 77 shows the stable and unstable regions of a parallel plate type electrostatic actuator together with associated spring constant values. This figure also suggests a drawback of the outlined method. Spring softening requires biasing the membrane towards its collapse point thus limiting the allowed displacement range. Moreover, the damping due to the air trapped within the membrane cavity is increased as the gap closes with increasing bias voltage. Both effects can be minimized by increasing the initial gap of the device at the expense of increasing voltage requirement.

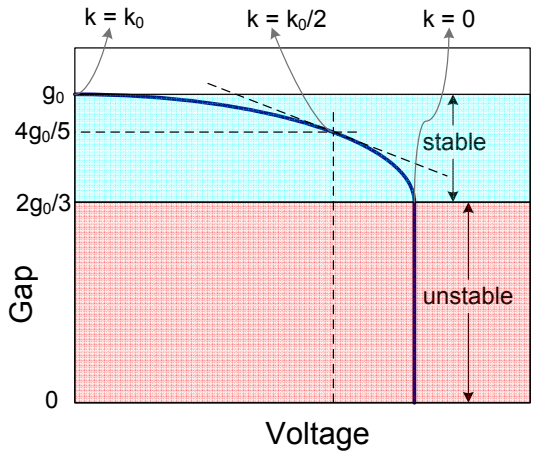

Figure 77. Operating regions of a parallel plate type electrostatic actuator with associated spring constant values.

The Matlab/Simulink implementation of the first-order lumped model given in figure 11 can be modified to include the effect of spring softening easily. The modified model is shown in figure 78. This model can be used to simulate the dynamics of the membrane together with the spring softening effect for any bias voltage on the electrostatic actuator.

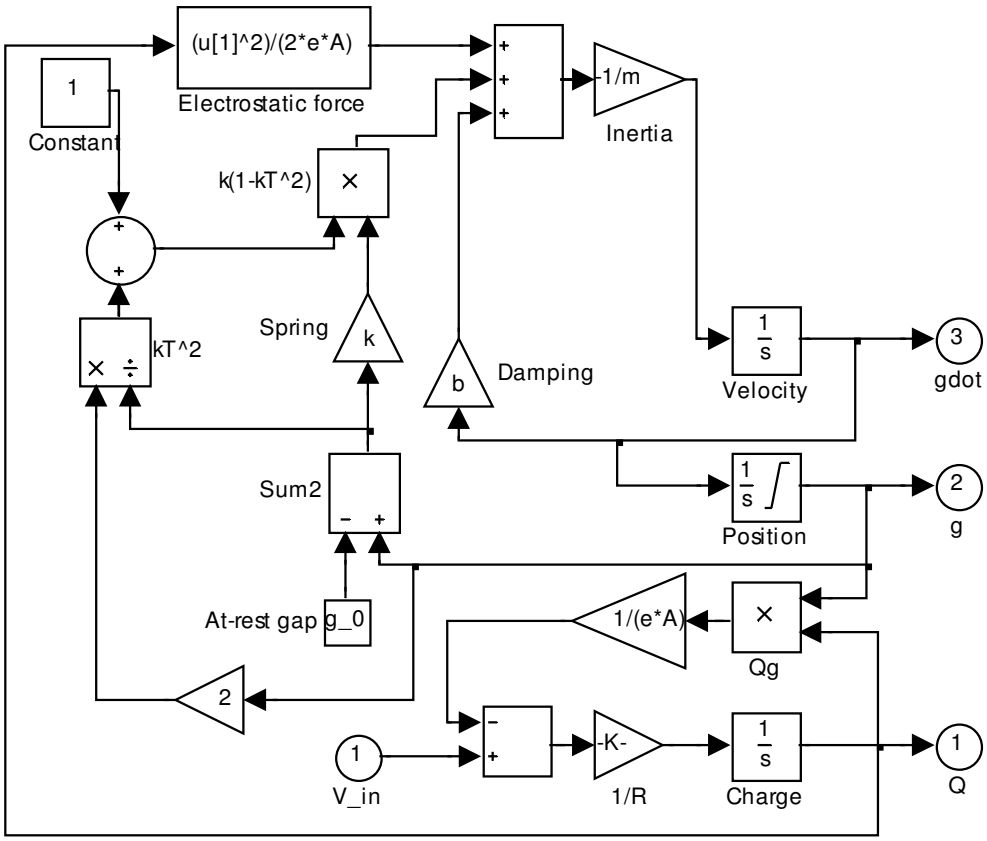

Figure 78. First-order lumped model of the electrostatic actuator, including the effect of spring softening, implemented with Simulink/Matlab.

Experimental Verification

For the experimental verification, a 250 μm diameter uniform parylene membrane on quartz was used. A spring constant of 24.4 N/m was measured at the center of the unbiased membrane by using a calibrated FESP cantilever from Veeco Metrology. The measurement was repeated after the membrane was biased and the variation of spring constant with respect to bias voltage is shown in figure 79. The measurement is in good agreement with the lumped model for the membrane of equation 9. The model also

predicts well the membrane displacement, which was measured using the white light interferometer as the inset to figure 79 shows. The measurements show the softening of the specific membrane under consideration approximately by 3-folds before it collapses when it moves one-third-of the initial gap. Fluctuations in voltage bias can cause membrane collapse as the gap height approaches one-third of its initial value. Thus, further reduction in spring constant is possible with a more precise control on the bias voltage.

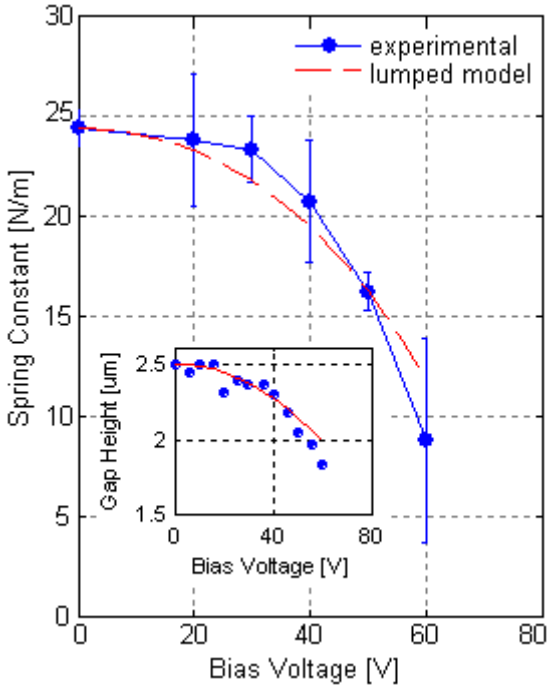

Figure 79. The softening of the membrane with increasing bias voltage. The inset curve shows the membrane displacement as a function of bias voltage.

The probe sensor was also characterized by actuating the membrane by the integrated electrostatic actuator, and recording the intensity of light going to first diffraction order. Figure 80(a) shows this variation with respect to the voltage applied

between the electrodes. For dynamic characterization, the probe was excited with a small amplitude AC signal at a maximum sensitivity point. Measured dynamic response of the membrane for two different DC bias values is shown in Figure 80(b). The results showed a shift of resonance peak and a change in quality factor which was expected due to spring softening effect.

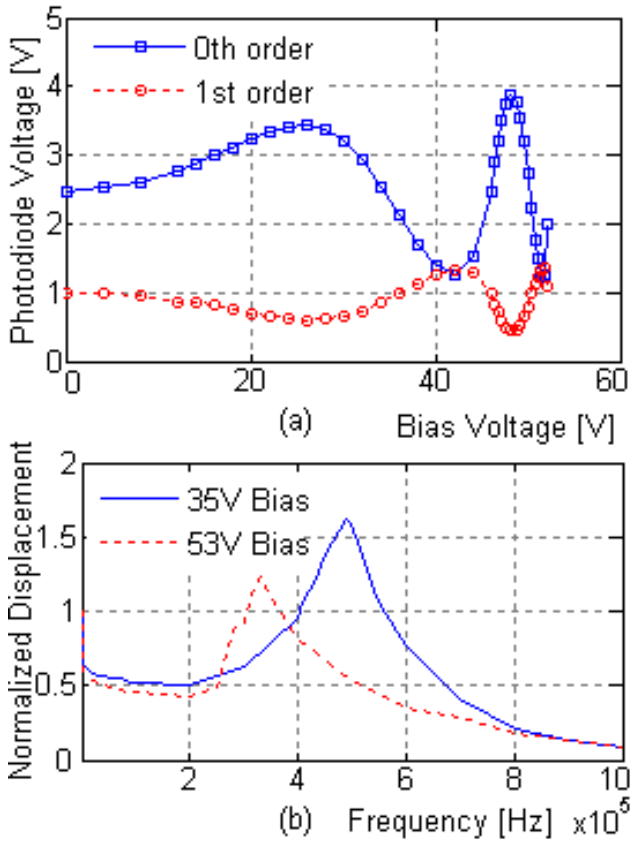

Figure 80. Experimental characterization of the membrane probe. (a) Variation of measured photodetector signals with respect to applied DC bias, (b) Frequency response when two different DC bias voltages are applied the electrostatic actuator terminals.

A proof of principle experiment showing sensitivity improvement was carried out with the same probe. First, a force curve measurement was performed after the membrane

was biased at 35 V. At this bias level, the spring constant of the membrane was 22 N/m. Then the AFM cantilever (TESP tip from Veeco Metrology, k=40 N/m) was driven in and out of contact of the membrane. The force curves obtained from the AFM system and the membrane probe are shown in Figure 81(a). The maximum force applied by the cantilever was 400 nN, for which the probe output was 0.66 V. The same experiment was repeated after the bias voltage was increased to 53 V thus reducing the spring constant of the membrane to 11 N/m. The maximum force applied was kept constant while the probe generated 1.36 V as shown in Figure 81(b). Comparing the results, the reduction in spring constant of the membrane matches to 2.06-folds increase in the output signal of the active probe. Given that the current AFM cantilever spring constants are typically in the range of 0.1 N/m to 40 N/m, further improvements are needed to achieve the full theoretical tuning range of the active probes so that one can cover a similar range with a single or several active probes.

Note that the force curve measurements in Figure 81 were performed at discrete bias voltages, since the membrane needs to be biased at certain levels for optimum detection sensitivity. An improved probe structure with quadrature phase-shifted dual gratings that provides good detection sensitivity for small displacement for the whole range of membrane displacement has also been developed [39]. Using that structure, precise and continuous control of spring constant at any bias voltage with good detection sensitivity should be possible.

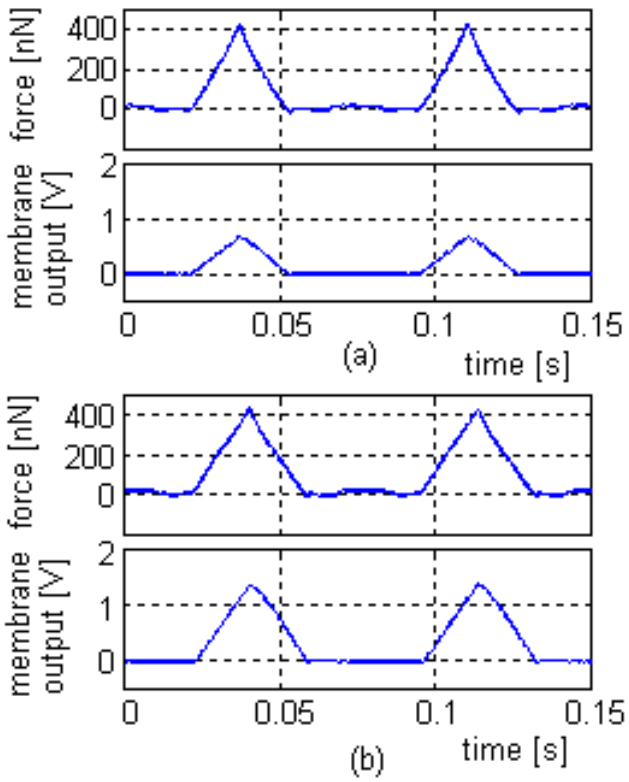

Figure 81. (a) Force curves obtained with the probe membrane biased at 35V. The top curve recorded from the AFM cantilever shows a peak force of 400nN. The bottom curve is recorded from the membrane with a spring constant of 22N/m. (b) The peak force applied by the cantilever is kept constant at 400nN as shown in top trace. The bottom trace is from the same membrane with an electrically reduced spring constant of 11N/m.

Another impact of this method can be expected in fast imaging systems. A fast imaging probe is usually stiffer for higher resonant frequency. However, the force sensitivity of the probe is inversely proportional with its stiffness. Another implication of the increased probe stiffness will be the increased shot noise contribution to the force noise. These adverse effects can be minimized on demand by electronically softening an already fabricated membrane.

Figure 5 shows SEM images of sharp tip integrated probes that are suitable for fast imaging. The use of clamped circular membranes made of aluminum, shown in

figure 5(b), for fast imaging was demonstrated before by actuating the membrane at 600 kHz [36]. The spring constant of a similar device with a diameter of 200 µm was measured 49 N/m at its center. Its spring constant was reduced to 18 N/m for a bias voltage of 31 V as shown in figure 82. This shows the validity of spring softening effect with different types of devices. Note that reducing spring constant of the probe will reduce its resonant frequency as well. Yet, it is valuable to have the capability of tuning spring constant of already fabricated devices for fast imaging. Also, it is worth mentioning that the resonant frequency scales with the square root of the spring constant while SNR improves by $(1/k)^{3/2}$ for a shot noise limited detection.

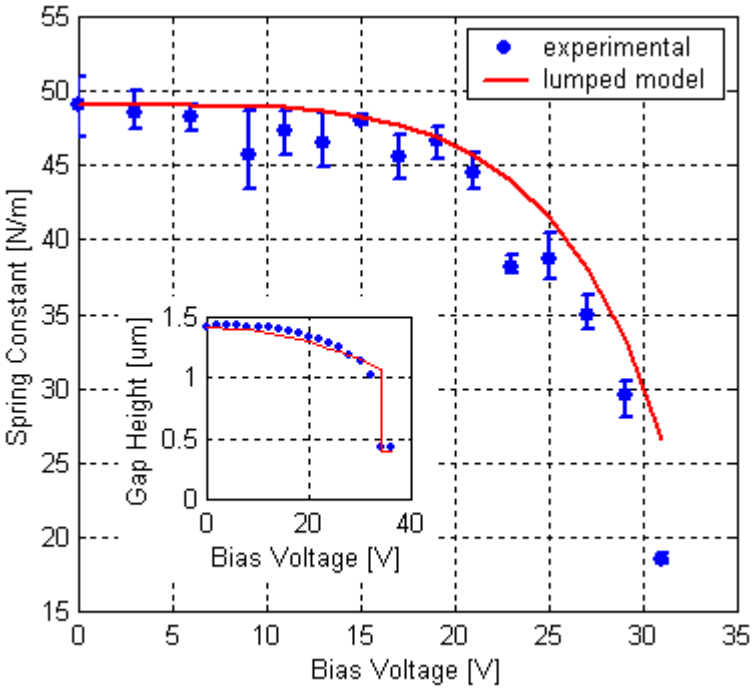

Figure 82. The softening of a 200 µm diameter aluminum membrane with increasing bias voltage. The inset curve shows the membrane displacement as a function of bias voltage.

In summary, the use of spring softening effect for electrical tuning of the spring constant of active AFM probes is introduced. This method is used to soften the membrane type active probes developed for force spectroscopy experiments to improve force sensitivity. It is effective to reduce spring constant of smaller probes with low viscous damping as shown in figure 76. Moreover, if the spring constant is dominated by the stress built up on the membrane as explained in chapter 3, electronic spring softening method can be employed. This also gives the freedom of increasing the thickness of dielectric layer for better insulation in fluid. In that case, increased stiffness due to thicker dielectric layer can be altered electronically.

The use of spring constant tuning method is also important for fast imaging applications. Experimental results with different types of probes show the general validity of this method. In addition to force spectroscopy and fast imaging applications, the effective use of this capability can be utilized to optimize a single probe for quantitative characterization of different surfaces with different viscoelastic properties [105].

CHAPTER 8

ATHERMALIZATION IN AFM USING MEMBRANE PROBES

One further application for the membrane probe architecture presented in this dissertation is athermalization in AFM based force spectroscopy applications. Athermalization consists of a system design such that ambient temperature fluctuations have no effect on the measurements made by the AFM cantilevers. The method developed is presented in this chapter.

Thermal Drift Problem in AFM

AFM has been used extensively to probe the nanoscale interactions that take place in wide range of time scales, from microseconds [106, 107] to minutes [108]. Long time scale experiments require stability and control of drift to minimize the effects of changes in ambient conditions. Thermal drift of the cantilever due to ambient temperature changes is a significant source of drift in AFM systems along with mechanical vibrations [109], material creep, and surface stress changes [110].

The AFM cantilever is usually a bimorph structure and is sensitive to temperature changes. It can even be used as a thermal detector [111]. In contrast, the deflection of the cantilever due to changes in ambient temperature is detrimental for AFM especially for long time-scale experiments where the rate of drift is comparable with the rate of

measured interactions. Thermal drift can be corrected using correlation methods [112] and Kalman filtering [113] for imaging purposes, but a different approach is needed to address this problem for force spectroscopy experiments involving biomolecules or cells. The effect of thermal drift in these experiments is two-folds: a) The cantilever bends which causes false force reading, b) The zero-force level shifts. These cannot be tolerated in biomolecular experiments where the samples are delicate and the precise control of both force and tip-to-sample distance is critical. Thus, effective methods for reducing thermal drift in AFM are needed to probe slow biomolecular interactions.

Wenzler *et al.* reported significant reduction of thermal drift by simply removing the metal layer over the base of the cantilever [114]. The end of the cantilever, where the deflection is read, still has the metal layer so these cantilevers are still exposed to thermally induced deflection. Instead of modifying the existing cantilevers, Beyder *et al.* developed a new type of force sensing structure to effectively reduce the probe dependent thermal drift [115]. In addition to the efforts for reducing the thermal drift with modified and new probes, researchers have also developed new techniques for existing cantilevers. Spagnoli *et al.* developed a software routine where the cantilever is time-shared between the sample and the substrate for referencing [108]. When the cantilever should be engaged on the sample for the entire experiment, the referencing can be done by reading the deflection of a reference sensor. The reference sensor, which provides distance information from the cantilever substrate-to-sample can simply be another cantilever next to the measurement one [116, 117], an interferometer [118], or an electrostatic sensor [109]. Effective suppression of drift has been demonstrated with these methods which require a feedback controller to keep the force constant. The reference sensor provides

information for compensation of drift in distance from cantilever plane to sample substrate. However, this approach does not prevent cantilever bending against a stationary surface while the cantilever is connected to the surface through a biomolecule or a cell. A typical experiment of this type is a force clamp experiment on a biomolecule [119].

Athermalization of AFM Cantilevers Using Membrane Probes

The method introduced for athermalization of AFM cantilevers consists of coupling them with thermo-mechanically matched microstructures. A specific case for biomolecular experiments is schematically shown in Figure 83.

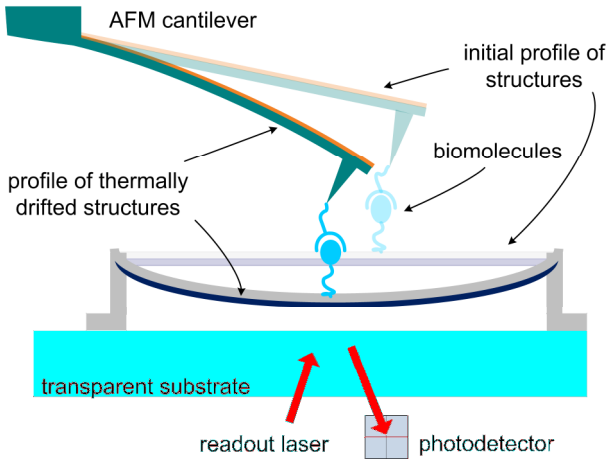

Figure 83. Schematic of a micromachined membrane with integrated diffraction grating interferometer coupled with AFM cantilever for athermalization of the cantilever in a biomolecular experiment. Profiles of the structures before and after thermal deflection are schematically shown.

Here, a passive bimaterial membrane is used as the matching microstructure designed such that it thermally deflects identically with the measurement cantilever. This provides constant tip-to-membrane distance even under thermal fluctuations when the piezo actuator keeps the cantilever-to-substrate distance the same. Thus when the piezo is ramped up and down for molecular force spectroscopy experiments, the peak force exerted on the biomolecules stays the same. Maintaining the peak force at the set value is important to avoid pushing the biomolecules with the probe tip too hard so that they would not be damaged and would become the secondary source of adhesive interaction [120]. Maintaining the set peak force without the need for an external driver or feedback is a unique capability with the introduced approach when compared to the previously demonstrated methods [109, 116-118]. Note that the cantilever still bends, and there is a shift in zero-force level set for the cantilever. This can be corrected by reading the displacement of the membrane. To make sure that the membrane displacement is only due to thermal fluctuations but not the biomolecular interaction forces, the membrane should be much stiffer as compared to the cantilever.

For experimental verification, a 320 μm long, triangular-shaped cantilever made of silicon nitride, chromium and gold (MLCT-C, Veeco Probes) was chosen. Thermal deflection of the cantilever tip was measured to be 315 nm/ºK. This figure matches the calculations using an analytical thermal deflection model for multi-layer structures and verifies the model [121]. To test the concept of athermalization of AFM cantilevers by a matching microstructure, the AFM cantilever in air was coupled with an identical one using the setup schematically shown in Figure 84(a). The reference cantilever was coupled on a diffraction grating using a 300 μm-thick spacer, and its displacement was

read using the diffraction grating interferometer. To control the temperature of the cantilevers, the substrate of the reference cantilever was placed on a thermoelectric cooler (TEC). The temperature was monitored using a semiconductor temperature sensor (LM135, National Semiconductor). Figure 84(b) shows the displacement traces of the cantilevers recorded simultaneously together with the temperature data. The system was thermally excited shortly by running current through TEC from point *a* to *b*, labeled with small arrows. The temperature change was 0.4 ºK and both cantilevers deflected by 128 nm, which was expected from analytical calculations. The forced thermal responses of the cantilevers (from point *a* to *b*) were nearly identical and the differential displacement signal showed significant reduction in thermal deflection. However, the natural responses of the cantilevers (from point *b* to the end) were different because the thermal time constants of the cantilevers were different due to the mounting differences. This reduced the thermal deflection cancellation capability to some extent, but the differential signal still exhibited at least 3-times smaller change when compared with the change on AFM signal.

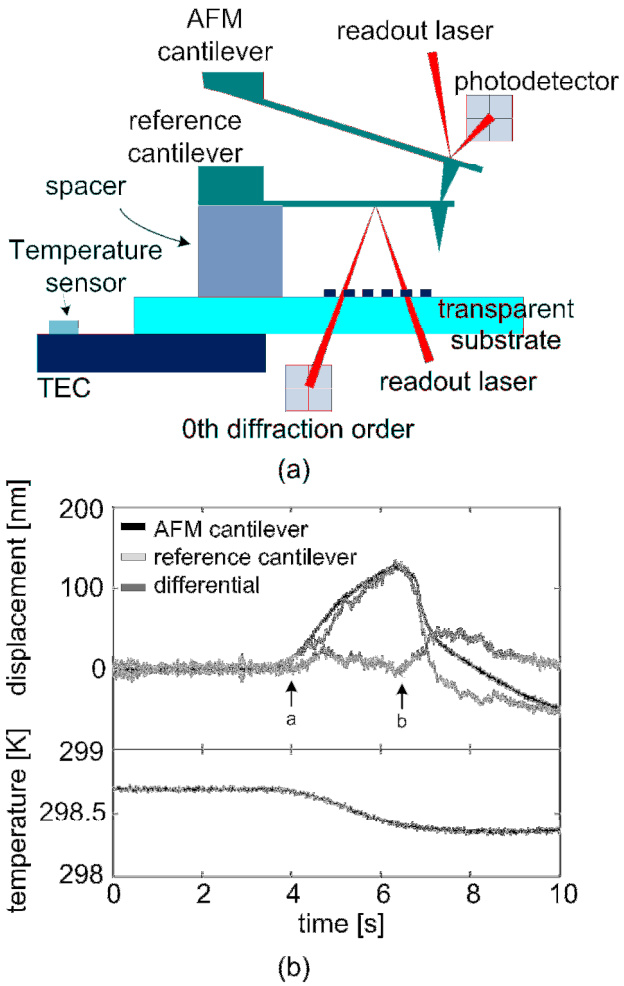

Figure 84. (a) Schematic of the setup with temperature control for the athermalization of an AFM cantilever using an identical one. (b) Displacements of the cantilevers recorded simultaneously together with the temperature data. Small arrows indicate when the thermal excitation was turned on and off.

For biomolecular experiments in fluid, coupling two cantilevers is not feasible without optimizing the interferometer for the reference cantilever such that it works well in fluid. Instead, the cantilever was coupled with a bimaterial circular membrane as schematically shown in Figure 85(a). The membrane chosen for this experiment was made of 1.5 µm-thick silicon nitride and 0.2 µm-thick gold. The fabrication process for this membrane is detailed in Chapter 3.

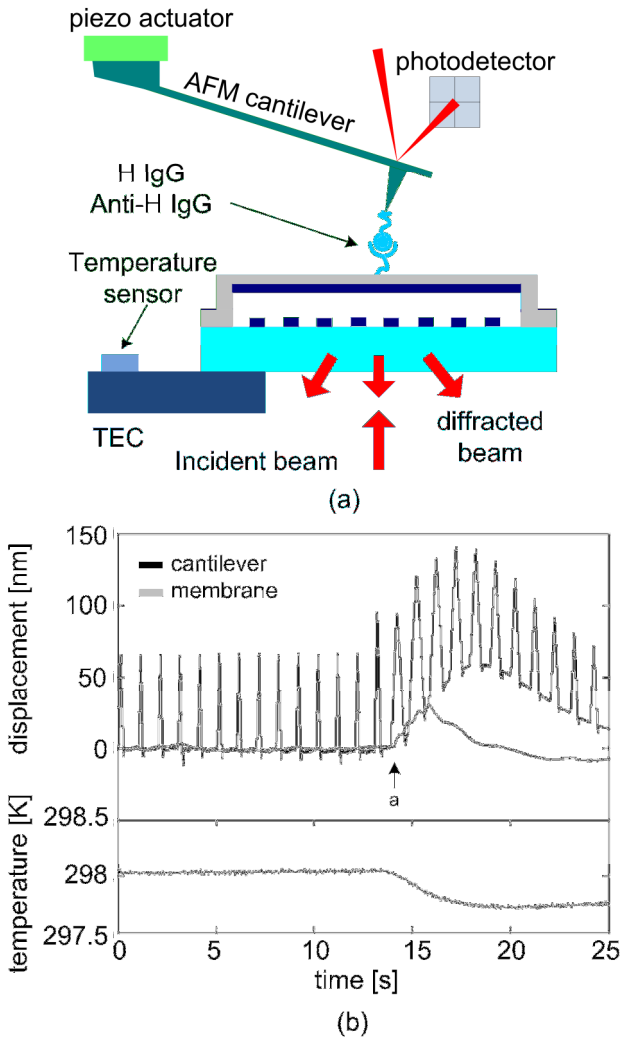

Figure 85. (a) Schematic of the setup with temperature control for biomolecular force spectroscopy. The AFM cantilever is engaged on a membrane that thermally displaces with the cantilever and reduces the effect of thermal fluctuations. (b) Displacements of the cantilever and the membrane recorded simultaneously together with the temperature data. Small arrow indicates when the thermal excitation was turned on.

The expected thermal deflection at the center of the 500 µm diameter membrane was calculated to be 119 nm/°K using an analytical model where the radius of curvature ($1/R$) for a temperature change of ΔT is expressed as [122]:

$$1/R = \frac{6}{h_1 + h_2} \cdot \frac{(\alpha_2 - \alpha_1)\Delta T(1 + h_1/h_2)^2}{3(1 + h_1/h_2)^2 + [1 + (h_1/h_2)(D_1/D_2)](h_1/h_2)^2 + \frac{1}{(h_1/h_2)(D_1/D_2)}} \quad (40)$$

where h, α, D are the thickness, coefficient of thermal expansion, and plate rigidity of the layers and the subscripts differentiate the layers.

The force spectroscopy experiment was carried out with the membrane incubated with 10-20 µl of anti-human IgG, and the AFM cantilever incubated with 10 µl of human IgG (10 µg/ml) for 15-20 min at room temperature. Using the piezo actuator, the cantilever was brought in and out of contact with the membrane and the displacement of the structures was recorded simultaneously as shown in Figure 85(b). Short thermal excitation by 0.3ºK was introduced at point *a* labeled with a small arrow. The peak deflection of the cantilever was 60 nm. This was measured when the structures were out of contact, which corresponds to the shift in zero-force level of the cantilever. The membrane, on the other hand, deflected 30 nm. The measured deflection at the center of the membrane was in good agreement with the analytical deflection model of Eq. (1).

The shift in zero-force level was reduced with a differential signal using the recorded membrane displacement as a reference, but the complete cancellation of thermal drift requires a membrane that exhibits the same deflection with the cantilever. The delay seen in deflection curves of the structures can be explained with the differences between thermal time constants of the structures. Note that the introduced thermal disturbance was abrupt. Consequently, the responses of the structures were dominated by their time

constants. However, the change in temperature in a typical force spectroscopy experiment is very slow, and a well designed membrane could match both the thermal deflection and the time constant of the cantilever as will be discussed below.

The second effect of thermal disturbance was the change in the peak force. This was reduced when the cantilever was coupled with the bimaterial membrane since both structures deflected in the same direction. Again, complete cancellation requires perfectly matching membrane. Note that the membrane used was 3000 times stiffer than the cantilever. This ensured the membrane displacement due to the biomolecular interactions was insignificant.

Based on the experimental data obtained using the available membrane, an ideal membrane for this particular cantilever is designed for this particular cantilever. The layer thicknesses are determined to match the thermal time constants of the structures. For immersed structures, thermal paths from the structure areas to the fluid will have higher conductivity. Based on this assumption, thermal time constant of the selected cantilever is equal to 1.71β s., where β is the ratio of the effective thermal path length to the thermal conductivity of the fluid. A membrane with 270 nm-thick gold and 400 nm-thick silicon nitride is designed to match this figure using water as working fluid. If the radius of this membrane is set to 150 μm (the design space for thermal deflection is given in Figure 86(a)), the analytical model of Eq. 1 predicts that the membrane center deflects by 320 nm/ºK. Thus it matches the thermal deflection of the selected cantilever. This figure was verified with the finite element simulation (FEM) using ANSYS software as shown in Figure 86(b). Moreover, Figure 86(b) shows the possibility of using this membrane with different cantilevers by coupling them at different locations on the

constant displacement contours on the membrane to match their thermal displacements. Note that this membrane is 300 times stiffer than the selected cantilever, and hence the membrane deflection due to biomolecular interactions will still be insignificant.

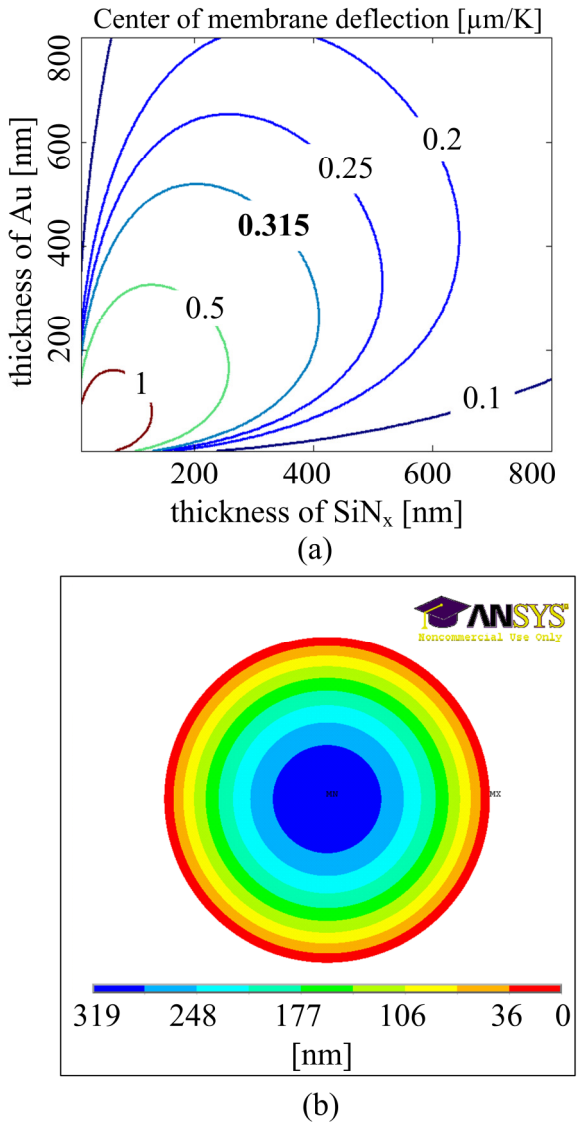

Figure 86. (a) Design space showing the center deflection of a 150 µm radius membrane made of silicon nitride and gold per Kelvin temperature difference. (b) FEM simulation showing the displacement profile of the membrane made of 150 nm thick silicon nitride and 200 nm thick gold.

Further envision is the use of different microstructures for athermalization in AFM with imaging applications. For imaging, it is important to thermo-mechanically match an area rather than a single point. Thick micro-plates anchored with bimorph legs can provide this capability.

Design of Athermal Membrane Probes

In addition to using membrane probes as thermo-mechanically matching structures for AFM cantilevers, it is also possible to design athermal membranes that can be used for force sensing. It is important to design an athermal membrane such that the center part of it, where the detection takes place, does not deflect due to temperature fluctuations. The non-uniform membrane structure introduced earlier is suitable for the realization of athermal membranes because of the discontinuous fashion of the top electrode. Unlike simple bimaterial membranes, this type of metal/dielectric combination can be designed such that the center of the membrane deflects upwards or downwards depending on the layer thicknesses. Moreover, it is possible to alter the thermo-mechanical behavior of the membrane by just varying the thickness of the top parylene layer. Note that the top parylene layer serves as a protection layer in fluid operation for the top electrode. Thus, changing the thickness of this layer does not alter the detection capabilities.

Figure 87(a) shows the cross section of a circular probe made of parylene and aluminum based on the previously introduced structure. The lateral dimensions are fixed based on the results obtained with this probe structure. The thickness of the bottom

parylene layer is limited to 0.5 μm to keep the stiffness of the detection membrane small. The thickness of the aluminum top electrode is fixed to 0.2 μm that can be deposited conformably without increasing the stiffness excessively. The thickness of top parylene layer, denoted by t_1 is set as a variable. Figure 87(b) shows the results of FEM simulations that predict the displacement of membrane center as a function of t_1 when the structure is exposed to +1 ˚C temperature difference.

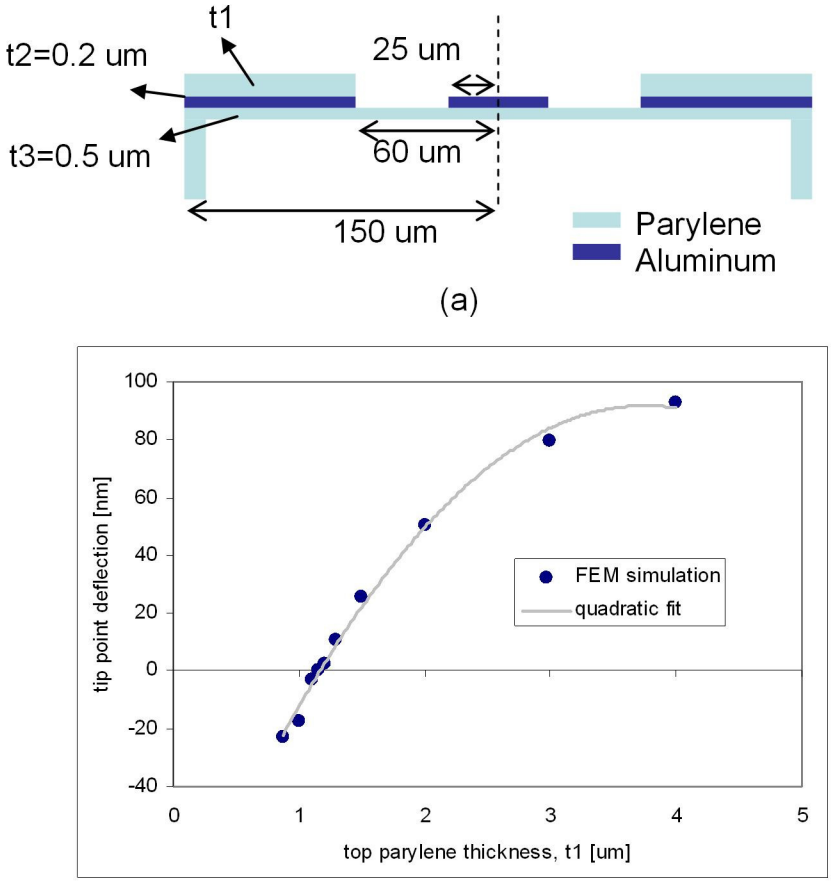

Figure 87. (a) Schematic of cross section of circular probe structure made of Parylene and Aluminum. (b) Deflection of the center of the structure with varying Aluminum thickness when the temperature of the structure is increased by 1 ˚C by FEM simulations with Ansys.

The center of membrane deflects upwards when the membrane is heated up for t_1>1.15 μm, and downwards for t_1<1.15 μm. At t_1=1.15 μm, the membrane center does not deflect thermally, pointing to an athermal design. Figure 88 shows the profile of this athermal membrane. During fabrication processes, it is possible to control the lateral dimensions within 10% [123]. However control on vertical dimension is not as good as this figure. Thus, the parylene layer thickness can vary even if it is nominally set to 1.15 μm. The effect of thickness variation on the tip point deflection of the membrane can be observed using the simulation results. The quadratic fit given in figure 87(b) agrees well with the FEM simulations and the slope of the fit can be used to observe the sensitivity of tip point deflection to thickness variations. The slope of the curve at t_1=1.15 μm is rather large, but note that the tip deflection varies within ±20 nm/ºK for 20% variation in parylene layer thickness. This figure is superior comparing with that of the cantilever presented here (315 nm/ºK).

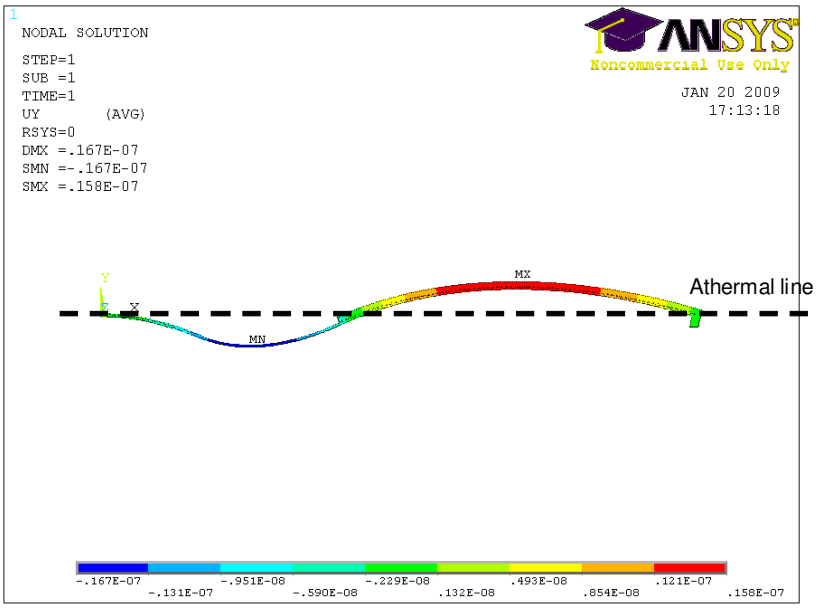

Figure 88. Half profile of the athermal probe structure (thickness of top Aluminum layer is 1.15 μm).

Growing a tip on top of the membrane eliminates the need for a cantilever. Athermal membrane probes presented here with integrated sharp tips can be used for long time-scale biophysical experiments. The details can be found in chapter 9.

CHAPTER 9

CONCLUSIONS AND FUTURE DIRECTIONS

This dissertation presents the research efforts for the development of membrane-based active probe structures with electrostatic actuation and integrated diffraction-based optical interferometric force detection for single-molecular force measurements. The aim of this project is to develop novel probes for improved AFM based single-molecular force assays. Biomolecular experiments demand for higher force resolution, better dynamic range and high-throughput. The probes presented in this dissertation are developed to address these demands by eliminating significant bottlenecks that are present in conventional cantilever-based instruments.

Membrane-based probes with different variations for different applications are designed in this project. These probes are fabricated at Microelectronics Research Center (MiRC) at Georgia Tech using surface micromachining technology.

A setup including optics and electronics for experimental characterization and biological experiments with the probes membranes is built. This setup allows integration of membrane probes with a commercial AFM head. The AFM cantilever and the membrane in the setup can be controlled independently and it is possible to readout their displacement simultaneously. The experiments are performed by engaging the cantilever on the membrane. The cantilever is used as a force sensor with stiff membranes that are used as surface-actuators. Softer membranes are also used as force sensors while the cantilever is used to localize biomolecules.

Stiff membranes are demonstrated to provide an actuation bandwidth of >100 kHz in fluid. That is far beyond the bandwidth of bulk piezo actuators. Moreover, surface-actuated cantilevers feel at least an order of magnitude lower hydrodynamic drag force as compared to piezo-actuated ones as experimentally shown.

In addition to fast pulling experiments, it is also desirable to perform long-time scale experiments. These experiments are more prone to drift of various sources, especially mechanical drift and thermal drift. Thermal drift in AFM based force spectroscopy experiments can be reduced by using a membrane probe as a sample holder as demonstrated as a part of this research. A membrane design for complete athermalization is provided. The realization of such probes is recommended for ultra-stable cantilever-based AFM. Athermalization capability together with fast pulling capability increases dynamic range and significant progress has been showed using membrane probes in this direction.

Besides actuation capabilities, the detection capabilities of the membrane probes are investigated thoroughly. Diffraction gratings integrated to the membranes allows displacement detection with a sensitivity of a Michelson interferometer. The displacement noise spectral density for the probe was measured to be below 10 fm/√Hz for frequencies as low as 3 Hz with differential readout scheme. This noise floor makes sensitive force measurements in fluid possible with carefully designed membranes. Design of such membranes is backed by FEM and analytical models and a force resolution of a few pN in fluid with a bandwidth of 1 kHz is experimentally demonstrated. The models developed shows that further progress is possible with smaller

membranes. Smaller membranes require better control on fabrication process for reliable operation in fluid.

An important and unique feature for detection is the adjustable spring constant. An immediate implication is that a small, relatively stiff membrane with smaller coefficient of viscous damping can be used for low force noise experiments. The large spring constant of such a membrane can be reduced electrically to obtain a larger signal for unit force, i.e. higher detection sensitivity, while still being limited by thermal mechanical noise dominated by the interaction of the probe structure with the surrounding liquid. The feasibility of this method is experimentally demonstrated as a part of this research.

The actuation and detection requirements do not always overlap. A non-uniform membrane structure is introduced in this research to optimize both the actuator and the sensor independently. Non-cantilever based parallel force spectroscopy is possible using these probes both as actuators and force sensors. The feasibility of this is shown and the realization of the method is recommended. The experiments can be performed by integrating sharp tips to the probe membranes. Moving these functionalized sharp tips against a stationary substrate may eliminate the need for cantilevers.

The membrane probes are used in a variety of biological experiments. A protocol for the biological functionalization of the membranes is successfully developed and unbinding force measurements are performed using these functionalized probes. The probes are used both as actuators and force sensors in biomolecular force spectroscopy experiments. In addition, a force-clamp setup is developed for life-time measurement

experiments. In this setup, membrane probes are controlled in a feedback loop to keep the force on biomolecules constant.

Future Directions

Actuation and force sensing capabilities of membrane probes are studied in this research. The probes are coupled with AFM cantilevers for biological experiments. It is necessary to attach biomolecules to the sharp tip of an AFM cantilever to guarantee single-molecule interactions. Sharp tip of an AFM cantilever is also used for localization purposes. Moreover, it is advantageous to have two force sensors for some applications such as athermalization as presented in chapter 8.

This architecture may obscure the advantages of membrane probes. Membrane probes designed for fast pulling experiments and fast imaging applications have high bandwidth. But when coupled with AFM cantilevers, the bandwidth of the system is limited by the slower component. Integrating sharp tips to the probe structures eliminate the need for AFM cantilevers. In this case, the probe can be used both as a force sensor and an actuator for biomolecular mechanics experiments.

Figure 89 schematically shows probes with integrated tips. These membranes can be actuated electrostatically as explained before or electromagnetically as shown in figure 89(b). Electromagnetic actuation requires passing current in a micro-coil embedded in the membrane and exposing the membrane to a magnetic field (B-field). Comparing with the electrostatic actuation, electromagnetic actuation method offers several advantages. Unlike electrostatic actuation, electromagnetic actuation provides linear, bi-directional membrane movement. It requires significantly lower voltage values for operation.

Moreover, pull-in phenomena observed with electrostatic actuators does not affect electromagnetic actuators. On the other hand, passing current through membrane induces joule heating that introduces thermal fluctuations in operation. This major drawback, however, can be tolerated with athermal membrane design as presented in chapter 8. Even if such a membrane heats up due to joule heating, the center of the membrane does not move significantly, making this method feasible.

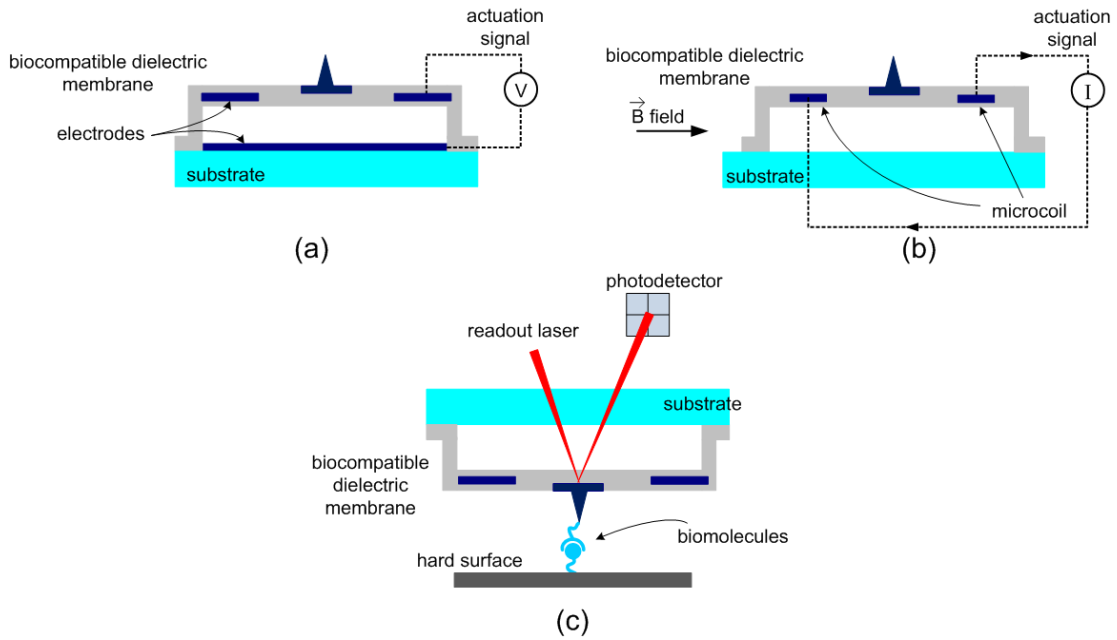

Figure 89. Schematic of athermal AFM probes with integrated (a) electrostatic (b) electromagnetic actuator. (c) Schematic of an athermal AFM probe in a typical single molecule experiment.

Membrane probes with integrated current-carrying loops can be used together with magnetic beads for fast screening and detection purposes. Figure 90 schematically shows a membrane probe coupled with a functionalized magnetic bead. It is possible to integrate these probes in fluidic microchannels and rupture experiments can be performed

by replacing AFM cantilevers with magnetic beads. Magnetic beads can be actuated against the membrane by varying current through the integrated coil and membrane detection can be detected interferometrically. These compact and low cost systems are ideal for fast screening applications.

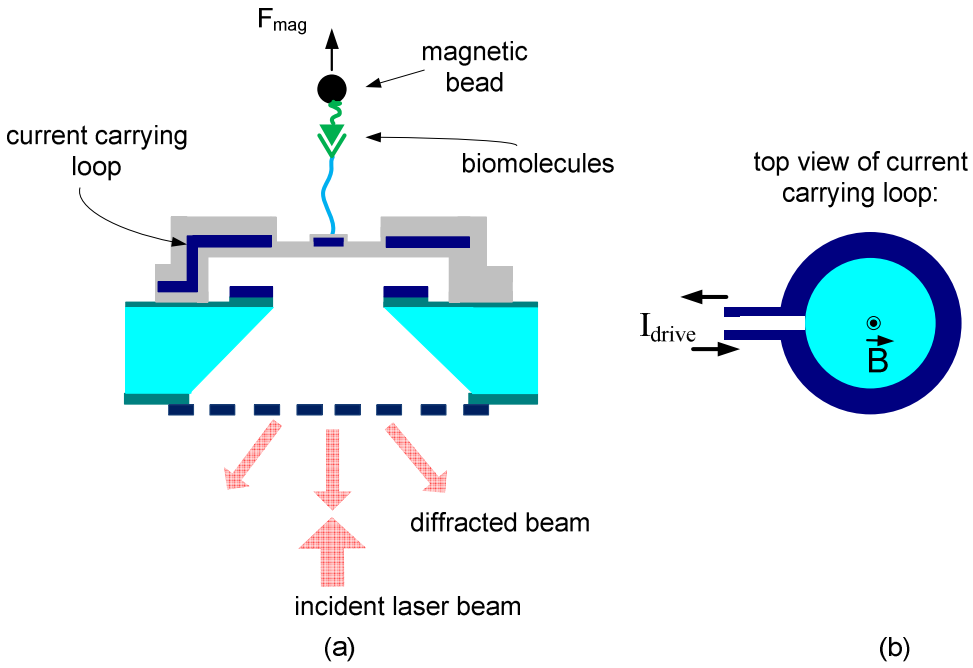

Figure 90. (a) Schematic of membrane probe with electromagnetic actuation capability coupled with a functionalized magnetic bead. (b) Current carrying loop embedded to the dielectric membrane used to generate B-field.

So far, the membrane probes are used for biomolecular interaction measurements. Novel transducers are also needed for cellular mechanics measurements. High force/displacement resolution of membrane probes can be good assays for these experiments. Figure 91 schematically shows an array of small membranes for cellular

mechanics measurements. By patterning smaller membranes it is possible to get local information from a single cell and segmented photodetectors (or a CCD) can be used for reading the displacement of membranes.

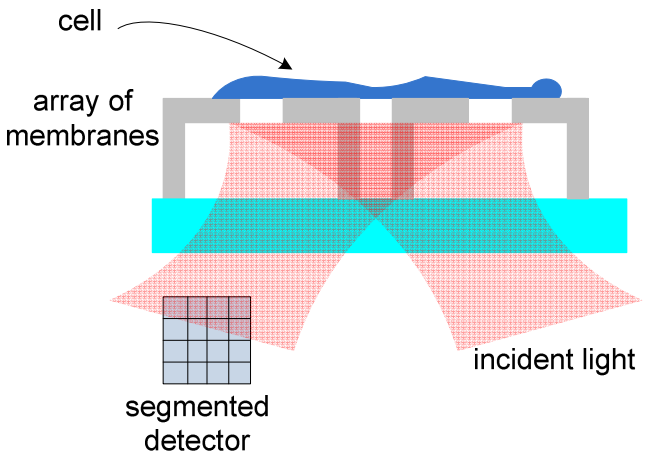

Figure 91. Schematic of an array of small membranes for cellular mechanics measurements.

REFERENCES

[1] G. Binnig, C. F. Quate, and C. Gerber, "Atomic Force Microscope," *Physical Review Letters,* vol. 56, p. 930, 1986.

[2] M. Radmacher, R. W. Tillamnn, M. Fritz, and H. E. Gaub, "From molecules to cells: imaging soft samples with the atomic force microscope," *Science,* vol. 257, pp. 1900-1905, 1992.

[3] K. Yamanaka, A. Noguchi, T. Tsuji, T. Koike, and T. Goto, "Quantitative material characterization by ultrasonic AFM," *Surface and Interface Analysis,* vol. 27, pp. 600-606, 1999.

[4] J. Zlatanova, S. M. Lindsay, and S. H. Leuba, "Single molecule force spectroscopy in biology using the atomic force microscope," *Progress In Biophysics & Molecular Biology,* vol. 74, pp. 37-61, 2000.

[5] O. Marti, B. Drake, and P. K. Hansma, "Atomic force microscopy of liquid-covered surfaces: Atomic resolution images," *Applied Physics Letters,* vol. 51, pp. 484-486, 1987.

[6] O. Marti, V. Ellings, M. Haugan, C. E. Bracker, J. Schneir, B. Drake, S. A. Gould, J. Gurley, L. Hellemans, and K. Shaw, "Scanning probe microscopy of biological samples and other surfaces," *Journal of Microscopy,* vol. 152, p. 6, 1988.

[7] D. Fotiadis, S. Scheuring, S. A. Muller, A. Engel, and D. J. Muller, "Imaging and manipulation of biological structures with the AFM," *Micron,* vol. 33, pp. 385-397, 2002.

[8] Z. F. Shao, J. Mou, D. M. Czajkowsky, J. Yang, and J. Y. Yuan, "Biological atomic force microscopy: What is achieved and what is needed," *Advances In Physics,* vol. 45, pp. 1-86, Jan-Feb 1996.

[9] J. Yang and Z. F. Shao, "Recent Advances In Biological Atomic-Force Microscopy," *Micron,* vol. 26, pp. 35-49, 1995.

[10] M. Rief and H. Grubmuller, "Force spectroscopy of single biomolecules," *Chemphyschem,* vol. 3, pp. 255-261, Mar 12 2002.

[11] T. Hugel and M. Seitz, "The Study of Molecular Interactions by AFM Force Spectroscopy," *Macromolecular Rapid Communications,* vol. 22, pp. 989-1016, 2001.

[12] E.-L. Florin, V. T. Moy, and H. E. Gaub, "Adhesion Forces Between Individual Ligand-Receptor Pairs," *Science,* vol. 264, pp. 415-417, 1994.

[13] E. Evans and K. Ritchie, "Dynamic strength of molecular adhesion bonds," vol. 72, pp. 1541-1555, 1997.

[14] E. Evans and D. Calderwood, "Forces and Bond Dynamics in Cell Adhesion," *Science,* vol. 316, p. 1148, 2007.

[15] B. T. Marshall, M. Long, J. W. Piper, T. Yago, R. P. McEver, and C. Zhu, "Direct observation of catch bonds involving cell-adhesion molecules," *Nature,* vol. 423, pp. 190-193, May 8 2003.

[16] C. Zhu, J. Lou, and R. P. McEver, "Catch bonds: Physical models, structural bases, biological function and rheological relevance," *Biorheology,* vol. 42, pp. 443-462, 2005.

[17] H. Clausen-Schaumann, M. Seitz, R. Krautbauer, and H. E. Gaub, "Force spectroscopy with single bio-molecules." vol. 4: Elsevier, 2000, pp. 524-530.

[18] P. Hinterdorfer and Y. F. Dufrene, "Detection and localization of single molecular recognition events using atomic force microscopy," *Nat Meth,* vol. 3, pp. 347-355, 2006.

[19] O. H. Willemsen, M. M. E. Snel, A. Cambi, J. Greve, B. G. De Grooth, and C. G. Figdor, "Biomolecular Interactions Measured by Atomic Force Microscopy," vol. 79, pp. 3267-3281, 2000.

[20] M. V. Bayas, A. Leung, E. Evans, and D. Leckband, "Lifetime Measurements Reveal Kinetic Differences between Homophilic Cadherin Bonds," vol. 90, pp. 1385-1395, 2006.

[21] M. S. Z. Kellermayer, S. B. Smith, H. L. Granzier, and C. Bustamante, "Folding-Unfolding Transitions in Single Titin Molecules Characterized with Laser Tweezers," *Science,* vol. 276, pp. 1112-1116, 1997.

[22] M. Kruithof, F. Chien, M. de Jager, and J. van Noort, "Subpiconewton Dynamic Force Spectroscopy Using Magnetic Tweezers," vol. 94, pp. 2343-2348, 2008.

[23] D. A. Walters, J. P. Cleveland, N. H. Thomson, P. K. Hansma, M. A. Wendman, G. Gurley, and V. Elings, "Short cantilevers for atomic force microscopy," *Review of Scientific Instruments,* vol. 67, p. 3583, 1996.

[24] M. B. Viani, T. E. Schaffer, A. Chand, M. Rief, H. E. Gaub, and P. K. Hansma, "Small cantilevers for force spectroscopy of single molecules," *Journal of Applied Physics,* vol. 86, pp. 2258-2262, 1999.

[25] T. Fukuma and S. P. Jarvis, "Development of liquid-environment frequency modulation atomic force microscope with low noise deflection sensor for cantilevers of various dimensions," *Review of Scientific Instruments,* vol. 77, pp. 043701-8, 2006.

[26] R. Merkel, P. Nassoy, A. Leung, K. Ritchie, and E. Evans, "Energy landscapes of receptor-ligand bonds explored with dynamic force spectroscopy." vol. 397, 1999, pp. 50-53.

[27] H. Janovjak, J. Struckmeier, and D. J. Müller, "Hydrodynamic effects in fast AFM single-molecule force measurements." vol. 34: Springer, 2005, pp. 91-96.

[28] T. Sulchek, R. J. Grow, G. G. Yaralioglu, S. C. Minne, C. F. Quate, S. R. Manalis, A. Kiraz, A. Aydine, and A. Atalar, "Parallel atomic force microscopy with optical interferometric detection," *Applied Physics Letters,* vol. 78, pp. 1787-1789, Mar 19 2001.

[29] J. Mertens, M. Alvarez, and J. Tamayo, "Real-time profile of microcantilevers for sensing applications," *Applied Physics Letters,* vol. 87, pp. 234102-3, 2005.

[30] M. Álvarez and J. Tamayo, "Optical sequential readout of microcantilever arrays for biological detection," *Sensors and Actuators B: Chemical,* vol. 106, pp. 687-690, 2005.

[31] P. Vettiger, G. Cross, M. Despont, U. Drechsler, U. Durig, B. Gotsmann, W. Haberle, M. A. Lantz, H. E. Rothuizen, R. Stutz, and G. K. Binnig, "The "millipede" - Nanotechnology entering data storage," *Ieee Transactions On Nanotechnology,* vol. 1, pp. 39-55, Mar 2002.

[32] S. C. Minne, S. R. Manalis, and C. F. Quate, "Parallel atomic force microscopy using cantilevers with integrated piezoresistive sensors and integrated piezoelectric actuators," *Applied Physics Letters,* vol. 67, pp. 3918-3920, 1995.

[33] B. Rogers, T. Sulchek, K. Murray, D. York, M. Jones, L. Manning, S. Malekos, B. Beneschott, J. D. Adams, H. Cavazos, and S. C. Minne, "High speed tapping mode atomic force microscopy in liquid using an insulated piezoelectric cantilever," *Review of Scientific Instruments,* vol. 74, pp. 4683-4686, 2003.

[34] Y.-S. Kim, H.-J. Nam, S.-M. Cho, J.-W. Hong, D.-C. Kim, and J. U. Bu, "PZT cantilever array integrated with piezoresistor sensor for high speed parallel operation of AFM," *Sensors and Actuators A: Physical,* vol. 103, pp. 122-129, 2003.

[35] H. P. Herzig, O. Manzardo, A. Meister, J. Polesel-Maris, R. Pugin, U. Staufer, and P. Vettiger, "Concept and Demonstration of Individual Probe Actuation in Two-Dimensional Parallel Atomic Force Microscope System," *Japanese Journal of Applied Physics,* vol. 46, pp. 6458-6462, 2007.

[36] A. G. Onaran, M. Balantekin, W. Lee, W. L. Hughes, B. A. Buchine, R. O. Guldiken, Z. Parlak, C. F. Quate, and F. L. Degertekin, "A new atomic force microscope probe with force sensing integrated readout and active tip," *Review Of Scientific Instruments,* vol. 77, Feb 2006.

[37] M. Balantekin, A. G. Onaran, and F. L. Degertekin, "Quantitative mechanical characterization of materials at the nanoscale through direct measurement of time-resolved tip–sample interaction forces," *Nanotechnology,* vol. 19, p. 085704, 2008.

[38] N. A. Hall, W. Lee, and L. Degertekin, "Capacitive micromachined ultrasonic trransducers with diffraction-based integrated optical displacement detection,"

Ieee Transactions On Ultrasonics Ferroelectrics And Frequency Control, vol. 50, pp. 1570-1580, Nov 2003.

[39] B. Van Gorp, A. G. Onaran, and F. L. Degertekin, "Integrated dual grating method for extended range interferometric displacement detection in probe microscopy," *Appl. Phys. Lett.,* vol. 91, p. 083101, 2007.

[40] O. Ferhanoglu, M. F. Toy, and H. Urey, "Two-Wavelength Grating Interferometry for MEMS Sensors " *Photonics Technology Letters, IEEE,* vol. 19, pp. 1895-1897, 2007.

[41] K. J. V. Vliet, G. Bao, and S. Suresh, "The biomechanics toolbox: experimental approaches for living cells and biomolecules," vol. 51, pp. 5881-5905, 2003.

[42] S. D. Senturia, *Microsystem Design*. Boston: Kluwer Academic Pub., 2001.

[43] E. S. Hung and S. D. Senturia, "Extending the travel range of analog-tuned electrostatic actuators," *Microelectromechanical Systems, Journal of,* vol. 8, pp. 497-505, 1999.

[44] J. A. Pelesko and D. H. Bernstein, *Modeling Mems and Nems*: CRC press, 2003.

[45] H. D. Gesser, *Applied chemistry: a textbook for engineers and technologists*: Kluwer Academic/Plenum Publishers, 2001.

[46] D. Sameoto, T. Hubbard, and M. Kujath, "Operation of electrothermal and electrostatic MUMPs microactuators underwater," *Journal of Micromechanics and Microengineering,* vol. 14, pp. 1359-1366, 2004.

[47] T. L. Sounart, T. A. Michalske, and K. R. Zavadil, "Frequency-dependent electrostatic actuation in microfluidic MEMS," *Microelectromechanical Systems, Journal of,* vol. 14, pp. 125-133, 2005.

[48] M. Bao and H. Yang, "Squeeze film air damping in MEMS," *Sensors and Actuators A: Physical,* vol. 136, pp. 3-27, 2007.

[49] P. Li, R. Hu, and Y. Fang, "A new model for squeeze-film damping of electrically actuated microbeams under the effect of a static deflection," *Journal of Micromechanics and Microengineering,* vol. 17, pp. 1242-1251, 2007.

[50] A. H. Nayfeh and M. I. Younis, "A new approach to the modeling and simulation of flexible microstructures under the effect of squeeze-film damping," *Journal of Micromechanics and Microengineering,* vol. 14, pp. 170-181, 2004.

[51] T. Veijola, H. Kuisma, J. Lahdenperä, and T. Ryhänen, "Equivalent-circuit model of the squeezed gas film in a silicon accelerometer," *Sensors and Actuators A: Physical,* vol. 48, p. 9, 1995.

[52] Y. Yao-Joe, M. Kamon, V. L. Rabinovich, C. Ghaddar, M. Deshpande, K. Greiner, and J. R. Gilbert, "Modeling gas damping and spring phenomena in MEMS with frequency dependent macro-models," in *Micro Electro Mechanical Systems, 2001. MEMS 2001. The 14th IEEE International Conference on*, 2001, pp. 365-368.

[53] D. Ostergaard and J. Mehner, "Using Heat Transfer Analogy to Solve for Squeeze Film Damping and Stiffness Coefficients in MEMS Structures," *technical paper from ANSYS Corporate,* 2003.

[54] W. Lee, N. A. Hall, Z. P. Zhou, and F. L. Degertekin, "Fabrication and characterization of a micromachined acoustic sensor with integrated optical readout," *IEEE Journal Of Selected Topics In Quantum Electronics,* vol. 10, pp. 643-651, May-Jun 2004.

[55] L. E. Kinsler, A. R. Frey, A. B. Coppens, and J. V. Sanders, *Fundamentals of Acoustics. 2000*: John Wiley, New York.

[56] Z. Dagan, R. Pfeffer, and S. Weinbaum, "Axisymmetric stagnation flow of a spherical particle near a finite planar surface at zero Reynolds number," *Journal of Fluid Mechanics,* vol. 122, pp. 273-294, 1982.

[57] A. W. Leissa, *Vibration of plates*: Storming Media, 1969.

[58] S. Basak, A. Raman, and S. V. Garimella, "Hydrodynamic loading of microcantilevers vibrating in viscous fluids," *Journal of Applied Physics,* vol. 99, pp. 114906-10, 2006.

[59] A. Maali, C. Hurth, R. Boisgard, C. Jai, T. Cohen-Bouhacina, and J.-P. Aime, "Hydrodynamics of oscillating atomic force microscopy cantilevers in viscous fluids," *Journal of Applied Physics,* vol. 97, pp. 074907-6, 2005.

[60] J. E. Sader, "Frequency response of cantilever beams immersed in viscous fluids with applications to the atomic force microscope," *Journal of Applied Physics,* vol. 84, pp. 64-76, 1998.

[61] R. J. Clarke, S. M. Cox, P. M. Williams, and O. E. Jensen, "The drag on a microcantilever oscillating near a wall," *Journal of Fluid Mechanics,* vol. 545, pp. 397-426, 2005.

[62] A. B. Comsol, "Comsol Multiphysics Modelling Guide." vol. 3, 2007.

[63] J. Happel and H. Brenner, *Low Reynolds number hydrodynamics: with special applications to particulate media*: Kluwer Academic Print on Demand, 1983.

[64] Z. Djuric, "Mechanisms of noise sources in microelectromechanical systems," *Microelectronics Reliability,* vol. 40, pp. 919-932, 2000.

[65] R. Kubo, "The fluctuation-dissipation theorem," *Reports on Progress in Physics,* vol. 29, pp. 255-284, 1966.

[66] A. Toshio, U. Takayuki, K. Noriyuki, Y. Daisuke, T. Masaaki, M. Atsushi, and Y. Hayato, "High-speed atomic force microscopy for observing dynamic biomolecular processes," *Journal of Molecular Recognition,* vol. 20, pp. 448-458, 2007.

[67] M. Di Giovanni, *Flat and corrugated diaphragm design handbook*: CRC Press, 1982.

[68] http://www.scscoatings.com/ (date accessed: Dec. 2009).

[69] T. A. Harder, Y. Tze-Jung, H. Qing, S. Chi-Yuan, and T. Yu-Chong, "Residual stress in thin-film parylene-c," in *Micro Electro Mechanical Systems, 2002. The Fifteenth IEEE International Conference on*, 2002, pp. 435-438.

[70] S. Alvarez-Blanco, S. Manolache, and F. Denes, "A novel plasma-enhanced way for surface-functionalization of polymeric substrates." vol. 47: Springer, 2001, pp. 329-336.

[71] N. A. Hall and F. L. Degertekin, "Integrated optical interferometric detection method for micromachined capacitive acoustic transducers," *Applied Physics Letters,* vol. 80, pp. 3859-3861, May 20 2002.

[72] M. Pachchigar, "Design Considerations for a Transimpedance Amplifier," *National Semiconductor Application Note,* vol. 1803, 2008.

[73] Burr-Brown, "Noise Analysis of FET Transimpedance Amplifiers," *Application Bulletin,* vol. SBOA060, 1994.

[74] T. C. Ralph, E. H. Huntington, C. C. Harb, B. C. Buchler, P. K. Lam, D. E. McClelland, and H. A. Bachor, "Understanding and controlling laser intensity noise," *Optical and Quantum Electronics,* vol. 31, pp. 583-598, 1999.

[75] R. Helkey, "Relative-intensity-noise cancellation in bandpass external-modulation links," *Microwave Theory and Techniques, IEEE Transactions on,* vol. 46, pp. 2083-2091, 1998.

[76] P. C. D. Hobbs, "Ultrasensitive laser measurements without tears," *Appl. Opt.,* vol. 36, pp. 903-920, 1997.

[77] M. Tinto and J. W. Armstrong, "Cancellation of laser noise in an unequal-arm interferometer detector of gravitational radiation," *Physical Review D,* vol. 59, p. 102003, 1999.

[78] J. Knight, J. McLean, and F. L. Degertekin, "Low temperature fabrication of immersion capacitive micromachined ultrasonic transducers on silicon and dielectric substrates," *Ieee Transactions On Ultrasonics Ferroelectrics And Frequency Control,* vol. 51, pp. 1324-1333, Oct 2004.

[79] H. P. Lang, M. Hegner, and C. Gerber, "Cantilever array sensors," *Materials Today,* vol. 8, pp. 30-36, 2005.

[80] J. B. Johnson, "Thermal Agitation of Electricity in Conductors," *Physical Review,* vol. 32, p. 97, 1928.

[81] H. Nyquist, "Thermal Agitation of Electric Charge in Conductors," *Physical Review,* vol. 32, p. 110, 1928.

[82] H. B. Callen and T. A. Welton, "Irreversibility and Generalized Noise," *Physical Review,* vol. 83, p. 34, 1951.

[83] T. B. Gabrielson, "Mechanical-thermal noise in micromachined acoustic and vibration sensors," *Electron Devices, IEEE Transactions on,* vol. 40, p. 903, 1993.

[84] F. Gittes and C. F. Schmidt, "Thermal noise limitations on micromechanical experiments," *European Biophysics Journal,* vol. 27, pp. 75-81, 1998.

[85] E. Majorana and Y. Ogawa, "Mechanical thermal noise in coupled oscillators," *Physics Letters A,* vol. 233, pp. 162-168, 1997.

[86] P. Paolino and L. Bellon, "Frequency dependence of viscous and viscoelastic dissipation in coated micro-cantilevers from noise measurement," *submitted to Nanotechnology,* 2009.

[87] B. Ohler, "Force Resolution in Force Spectroscopy Experiments: Thermal Noise and Bandwidth," *Veeco Instruments Inc.,* 2007.

[88] L. Chen, C. L. Cheung, P. D. Ashby, and C. M. Lieber, "Single-Walled Carbon Nanotube AFM Probes: Optimal Imaging Resolution of Nanoclusters and Biomolecules in Ambient and Fluid Environments," *Nano Letters,* vol. 4, pp. 1725-1731, 2004.

[89] P. J. Chen, D. C. Rodger, R. Agrawal, S. Saati, E. Meng, R. Varma, M. S. Humayun, and Y. C. Tai, "Implantable micromechanical parylene-based pressure sensors for unpowered intraocular pressure sensing," *Journal of Micromechanics and Microengineering,* vol. 17, pp. 1931-1938, Oct 2007.

[90] H. Jui-Mei, L. Rieth, R. A. Normann, P. Tathireddy, and F. Solzbacher, "Encapsulation of an Integrated Neural Interface Device With Parylene C," *Biomedical Engineering, IEEE Transactions on,* vol. 56, pp. 23-29, 2009.

[91] F. Poncin-Epaillard and G. Legeay, "Surface engineering of biomaterials with plasma techniques," *Journal of Biomaterials Science, Polymer Edition,* vol. 14, pp. 1005-1028, 2003.

[92] M. Suzuki, A. Kishida, H. Iwata, and Y. Ikada, "Graft copolymerization of acrylamide onto a polyethylene surface pretreated with glow discharge," *Macromolecules,* vol. 19, pp. 1804-1808, 2002.

[93] R. P. McEver, "Selectins - Novel Receptors That Mediate Leukocyte Adhesion During Inflammation," *Thrombosis And Haemostasis,* vol. 65, pp. 223-228, Mar 4 1991.

[94] K. K. Sarangapani, T. Yago, A. G. Klopocki, M. B. Lawrence, C. B. Fieger, S. D. Rosen, R. P. McEver, and C. Zhu, "Low force decelerates L-selectin dissociation from P-selectin glycoprotein ligand-1 and endoglycan," *Journal Of Biological Chemistry,* vol. 279, pp. 2291-2298, Jan 16 2004.

[95] K. K. Sarangapani, H. Torun, O. Finkler, C. Zhu, and F. L. Degertekin, "Membrane-based Actuation for High Speed Single Molecule Force Spectroscopy Studies Using AFM," *European Biophysics Journal,* vol. submitted for publication, 2009.

[96] E. Evans, A. Leung, D. Hammer, and S. Simon, "Chemically distinct transition states govern rapid dissociation of single L-selectin bonds under force," *Proceedings Of The National Academy Of Sciences Of The United States Of America,* vol. 98, pp. 3784-3789, 2001.

[97] X. Zhang, S. E. Craig, H. Kirby, M. J. Humphries, and V. T. Moy, "Molecular Basis for the Dynamic Strength of the Integrin ±4²1/VCAM-1 Interaction," vol. 87, pp. 3470-3478, 2004.

[98] M. J. Serpe, F. R. Kersey, J. R. Whitehead, S. M. Wilson, R. L. Clark, and S. L. Craig, "A Simple and Practical Spreadsheet-Based Method to Extract Single-Molecule Dissociation Kinetics from Variable Loading-Rate Force Spectroscopy Data," *The Journal of Physical Chemistry C,* vol. 112, pp. 19163-19167, 2008.

[99] D. F. J. Tees, J. T. Woodward, and D. A. Hammer, "Reliability theory for receptor--ligand bond dissociation," *The Journal of Chemical Physics,* vol. 114, pp. 7483-7496, 2001.

[100] H. Torun, K. K. Sarangapani, F. L. Degertekin, and C. Zhu, "Parallel active polymer probes with integrated interferometer for single molecule force spectroscopy," in *International Meeting on AFM in Life Sciences and Medicine*, Monterey, CA., 2008.

[101] S. Ghatnekar-Nilsson, E. Fors, G. Abadal, J. Verd, F. Campabadal, P. F, M. rez, J. Esteve, N. Barniol, A. Boisen, and L. Montelius, "Resonators with integrated CMOS circuitry for mass sensing applications, fabricated by electron beam lithography," *Nanotechnology,* p. 98, 2005.

[102] J. H. Zhao, G. E. Bridges, and D. J. Thomson, "Direct evidence of ``spring softening" nonlinearity in micromachined mechanical resonator using optical beam deflection technique," *J. Vac. Sci. Technol. A,* vol. 24, pp. 732-736, 2006.

[103] S. Chowdhury, M. Ahmadi, and W. C. Miller, "A closed-form model for the pull-in voltage of electrostatically actuated cantilever beams," *Journal of Micromechanics and Microengineering,* p. 756, 2005.

[104] G. G. Yaralioglu, A. S. Ergun, B. Bayram, E. Haeggstrom, and B. T. Khuri-Yakub, "Calculation and measurement of electromechanical coupling coefficient of capacitive micromachined ultrasonic transducers," *Ultrasonics, Ferroelectrics and Frequency Control, IEEE Transactions on,* vol. 50, p. 449, 2003.

[105] A. T. Joseph and S. W. Joshua, "Sensitivity of flexural and torsional vibration modes of atomic force microscope cantilevers to surface stiffness variations," *Nanotechnology,* vol. 12, p. 322, 2001.

[106] T. Ando, T. Uchihashi, N. Kodera, D. Yamamoto, A. Miyagi, M. Taniguchi, and H. Yamashita, "High-speed AFM and nano-visualization of biomolecular processes," *Pflügers Archiv European Journal of Physiology,* vol. 456, pp. 211-225, 2008.

[107] M. Anwar and I. Rousso, "Atomic force microscopy with time resolution of microseconds," *Applied Physics Letters,* vol. 86, pp. 014101-3, 2005.

[108] C. Spagnoli, A. Beyder, S. R. Besch, and F. Sachs, "Drift-free atomic force microscopy measurements of cell height and mechanical properties," *Review of Scientific Instruments,* vol. 78, pp. 036111-3, 2007.

[109] G. Schitter and A. Stemmer, "Eliminating mechanical perturbations in scanning probe microscopy," *Nanotechnology,* vol. 13, pp. 663-665, 2002.

[110] A. M. Moulin, S. J. O'Shea, and M. E. Welland, "Microcantilever-based biosensors," *Ultramicroscopy,* vol. 82, pp. 23-31, 2000.

[111] P. G. Datskos, N. V. Lavrik, and S. Rajic, "Performance of uncooled microcantilever thermal detectors," *Review of Scientific Instruments,* vol. 75, pp. 1134-1148, 2004.

[112] J. H. Kindt, J. B. Thompson, M. B. Viani, and P. K. Hansma, "Atomic force microscope detector drift compensation by correlation of similar traces acquired at different setpoints," *Review of Scientific Instruments,* vol. 73, pp. 2305-2307, 2002.

[113] B. Mokaberi and A. A. G. Requicha, "Drift compensation for automatic nanomanipulation with scanning probe microscopes," *Automation Science and Engineering, IEEE Transactions on,* vol. 3, pp. 199-207, 2006.

[114] L. A. Wenzler, G. L. Moyes, and J. T. P. Beebe, "Improvements to atomic force microscopy cantilevers for increased stability," *Review of Scientific Instruments,* vol. 67, pp. 4191-4197, 1996.

[115] A. Beyder, C. Spagnoli, and F. Sachs, "Reducing probe dependent drift in atomic force microscope with symmetrically supported torsion levers," *Review of Scientific Instruments,* vol. 77, pp. 056105-3, 2006.

[116] S. M. Altmann, P.-F. Lenne, and J. K. H. Horber, "Multiple sensor stabilization system for local probe microscopes," *Review of Scientific Instruments,* vol. 72, pp. 142-149, 2001.

[117] J. L. Choy, S. H. Parekh, O. Chaudhuri, A. P. Liu, C. Bustamante, M. J. Footer, J. A. Theriot, and D. A. Fletcher, "Differential force microscope for long time-scale biophysical measurements," *Review of Scientific Instruments,* vol. 78, pp. 043711-6, 2007.

[118] A. W. Sparks and S. R. Manalis, "Atomic force microscopy with inherent disturbance suppression for nanostructure imaging," *Nanotechnology,* vol. 17, pp. 1574-1579, 2006.

[119] J. M. Fernandez and H. Li, "Force-Clamp Spectroscopy Monitors the Folding Trajectory of a Single Protein," vol. 303, pp. 1674-1678, March 12, 2004 2004.

[120] A. Ikai, *World of Nano-Biomechanics: Mechanical Imaging and Measurement by Atomic Force Microscopy*: Elsevier Science, 2007.

[121] H. Torun and H. Urey, "Thermal deflections in multilayer microstructures and athermalization," *Journal Of Applied Physics,* vol. 100, Jul 15 2006.

[122] P. A. Engel, *Structural analysis of printed circuit board systems*: Springer, 1993.

[123] S. Franssila, *Introduction to microfabrication*: Wiley, 2004.